Industrial Alloys Studied by Surface Sensitive Techniques

Rullik, Lisa

2018

Document Version:
Publisher's PDF, also known as Version of record

Link to publication

Citation for published version (APA):
Rullik, L. (2018). *Industrial Alloys Studied by Surface Sensitive Techniques*. [Doctoral Thesis (compilation), Synchrotron Radiation Research, Department of Physics]. Fysiska institutionen, Lunds universitet.

Total number of authors:
1

General rights
Unless other specific re-use rights are stated the following general rights apply:
Copyright and moral rights for the publications made accessible in the public portal are retained by the authors and/or other copyright owners and it is a condition of accessing publications that users recognise and abide by the legal requirements associated with these rights.

- Users may download and print one copy of any publication from the public portal for the purpose of private study or research.
- You may not further distribute the material or use it for any profit-making activity or commercial gain
- You may freely distribute the URL identifying the publication in the public portal

Read more about Creative commons licenses: https://creativecommons.org/licenses/

Take down policy
If you believe that this document breaches copyright please contact us providing details, and we will remove access to the work immediately and investigate your claim.

LUND UNIVERSITY

PO Box 117
221 00 Lund
+46 46-222 00 00

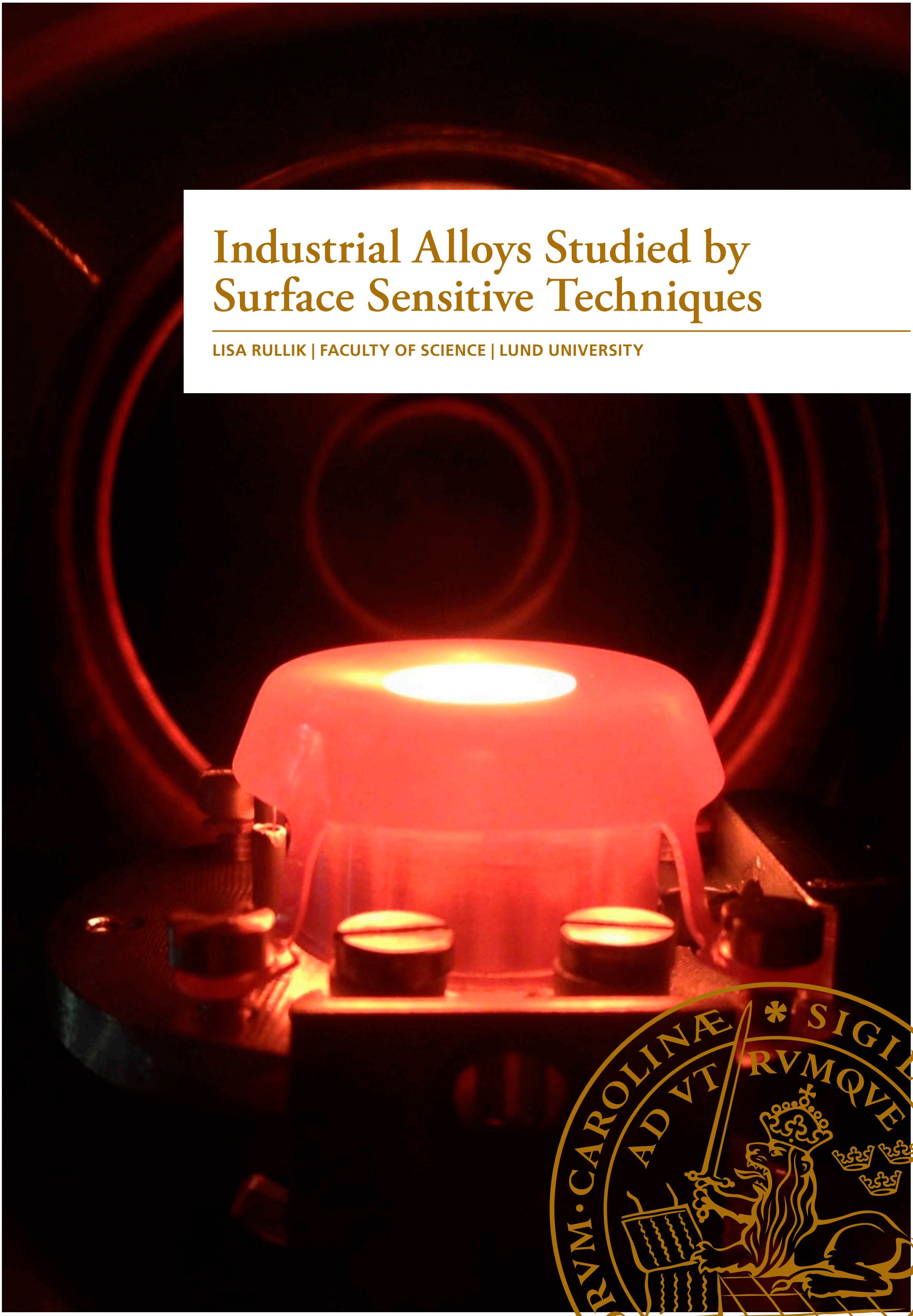

Industrial Alloys Studied by Surface Sensitive Techniques

LISA RULLIK | FACULTY OF SCIENCE | LUND UNIVERSITY

Industrial Alloys Studied by Surface Sensitive Techniques

by Lisa Rullik

LUND
UNIVERSITY

Thesis for the degree of Doctor of Philosophy

Thesis advisors: Prof. Edvin Lundgren, Prof. Anders Mikkelsen

Faculty opponent: Dr. Robert Lindsay, The University of Manchester

To be presented, with the permission of the Faculty of Science, Lund University,
for public criticism in the Rydberg Lecture Hall at the Department of Physics
on Friday, the 14th of December 2018 at 13:15.

DOKUMENTDATABLAD enl SIS 61 41 21

Organization
LUND UNIVERSITY

Department of Physics
Box 118
SE–221 00 LUND
Sweden

Document name
DOCTORAL DISSERTATION

Date of disputation
2018-12-14

Sponsoring organization
Swedish Foundation for Strategic Research (SSF project RMA11-0090, Aluminum oxides for processing and products, ALUX)

Author(s)
Lisa Rullik

Title and subtitle
Industrial Alloys Studied by Surface Sensitive Techniques

Abstract

This thesis reports on surface studies of industrial alloys, in particluar aluminum alloys and duplex stainless steels. The importance of these materials for society manifests in the vast range of applications which rely on their performance. The challange in investigating these materials lies within their composition as they typically consist of a multitude of alloying elements in order to obtain the improved physical and mechanical properties.

For both alloy groups, the properties of their protective surface oxides are of major importance as they determine the material's performance with respect to corrosion, erosion, wear, joining, and coating. Therefore, a surface science approach was employed to study the chemical composition, thickness and distribution of phases and particles at the oxide surfaces. Contemporary research in this area is characterized by attempts to bridge the gap between classical model systems in highly controlled environments and complex industrial alloys in experimental conditions mimicking their working environment.

In this thesis, the material gap is bridged by using industrial samples instead of single crystal model systems. Custom made composite aluminum alloys made for brazing applications, industrial aluminum alloys, and multiphase steels, are investigated. Simultaneously to the material gap, the pressure gap is addressed by exposing the materials to more realistic conditions using APXPS. This technique allows for measurements while the sample is exposed to different gases up to the lower mbar regime. By comparing APXPS with standard UHV measurements major differences in the resulting surface oxide composition are observed. The thickness of the native oxide films of the different samples is determined by XRR measurements performed at different experimental conditions ranging from UHV to air and water enviroments. XPEEM and LEEM is used to follow the surface development during heating of aluminum and steel samples on a sub-micron length scale. The microscopic imaging allows for the identification of the chemical state of the alloying elements and their lateral distribution in the surface layer.

Key words
aluminum alloy, brazing, AA 6063, duplex stainless steels, SAF 2507, XPS, APXPS, XPEEM, XRR, microstructure

Classification system and/or index terms (if any)

Supplementary bibliographical information

Language
English

ISSN and key title

ISBN
978-91-7753-900-1 (print)
978-91-7753-901-8 (pdf)

Recipient's notes

Number of pages
192

Price

Security classification

I, the undersigned, being the copyright owner of the abstract of the above-mentioned dissertation, hereby grant to all reference sources the permission to publish and disseminate the abstract of the above-mentioned dissertation.

Signature Lisa Rullik

Date 2018-11-05

Industrial Alloys Studied by Surface Sensitive Techniques

Doctoral Dissertation

by Lisa Rullik

LUND
UNIVERSITY

Faculty of Science
Department of Physics
Division of Synchrotron Radiation Research

A doctoral thesis at a university in Sweden takes either the form of a single, cohesive research study (monograph) or a summary of research papers (compilation thesis), which the doctoral student has written alone or together with one or several other author(s).

In the latter case the thesis consists of two parts. An introductory text puts the research work into context and summarizes the main points of the papers. Then, the research publications themselves are reproduced, together with a description of the individual contributions of the authors. The research papers may either have been already published or are manuscripts at various stages (in press, submitted, or in draft).

Cover image:
Photo of heated steel sample in the analysis chamber at the HERMES beamline, Soleil, Paris.

Funding information: The thesis work was financially supported by Swedish Foundation for Strategic Research (SSF project RMA11-0090, Aluminum oxides for processing and products, ALUX).

© 2018 Lisa Rullik and the respective publishers.

Faculty of Science
Department of Physics
Division of Synchrotron Radiation Research

ISBN: 978-91-7753-900-1 (print)
ISBN: 978-91-7753-901-8 (pdf)

Printed in Sweden by Media-Tryck, Lund University, Lund 2018

Ohne Geisteswissenschaften sind wir Barbaren,
ohne Naturwissenschaften Neandertaler.
-Stefan Hüfner-

Come on, Rory! It isn't rocket science, it's just quantum physics!
-The Doctor-

Contents

Preface **iii**

Abstract v
List of Publications vii
List of Abbreviations xi
Populärwissenschaftliche Zusammenfassung xiii
Populärvetenskaplig sammanfattning xv
Acknowledgements xvii

Industrial Alloys Studied by Surface Sensitive Techniques **1**

1 Introduction 1
2 Materials 5
  2.1 Aluminum 5
    2.1.1 Pure Aluminum 6
      2.1.1.1 Single Crystals 7
      2.1.1.2 Polycrystalline Aluminum 8
    2.1.2 Aluminum Oxide and Hydroxides 9
    2.1.3 Native Aluminum Oxide Films 10
    2.1.4 Aluminum Alloys 12
      2.1.4.1 Role of Alloying Elements 13
      2.1.4.2 Strengthening 15
      2.1.4.3 Brazing Sheets 17
  2.2 Iron and Stainless Steels 19
    2.2.1 Duplex Stainless Steels 21
      2.2.1.1 Super Duplex Stainless Steels 22
      2.2.1.2 Role of Alloying Elements 23
      2.2.1.3 Phases and Their Transformation 24
3 Instrumentation and Experimental Methods 27
  3.1 Electron and X-rays Sources 27
    3.1.1 Electron Sources 28
    3.1.2 X-ray Sources 28
    3.1.3 Synchrotron Radiation 29
    3.1.4 Experimental Considerations 30

3.2 Scattering Techniques 32
3.2.1 X-ray Reflectivity 32
3.2.2 Low Energy Electron Diffraction 34
3.3 Spectroscopy 37
3.3.1 X-ray Photoelectron Spectroscopy 37
3.3.1.1 Three-step model 38
3.3.1.2 Data Analysis 39
3.3.1.3 Ambient Pressure X-ray Photoelectron Spectroscopy 42
3.3.2 X-ray Absorption Spectroscopy 44
3.4 Microscopy 46
3.4.1 Mirror Electron Microscopy 48
3.4.2 Low Energy Electron Microscopy 49
3.4.3 Photoelectron Emission Microscopy 51
3.4.4 Scanning Electron Microscopy 53
3.4.5 Comparison 55
4 Summary of Papers 57
5 Outlook 63
References 67

Scientific publications **83**
Paper I: The thickness of native oxides on aluminum alloys and single crystals 85
Paper II: Surface development of an aluminum brazing sheet during heating studied by XPEEM and XPS 95
Paper III: Surface development of a brazing alloy during heat treatment–a comparison between UHV and APXPS 109
Paper IV: Surface Oxide Development on Aluminum Alloy 6063 during Heat Treatment 127
Paper V: Surface Development of Super Duplex Stainless Steel SAF 2507 during Heat Treatment 149

Preface

Abstract

This thesis reports on surface studies of industrial materials whose importance for society manifests in the vast range of applications. In industrial materials alloying is performed in order to improve the parent material's physical and mechanical properties such as strength, corrosion and wear resistance, as well as high temperature performance in comparison to the pure metal. Even though metals like copper, tin, and zinc have been alloyed since approximately 2500 BCE, current research projects still try to unravel the complex interactions between the single alloying elements on an atomic scale. This thesis focuses on two groups of metallic alloys: aluminum alloys and steels.

For both alloy groups, the properties of their protective surface oxides are of major importance as they determine the material's performance with respect to corrosion, erosion, wear, joining, and coating. Therefore, a surface science approach was employed to study the chemical composition, thickness and distribution of phases and particles at the oxide surfaces. Contemporary research in this area is characterized by attempts to bridge the gap between classical model systems in highly controlled environments and industrial complex alloys in experimental conditions mimicking their working environment.

Here, the material gap is bridged by transitioning from single crystals to industrial alloy standards, see Papers I and IV. Custom made composite aluminum alloys made for brazing applications, Papers II and III, and multiphase steel, Paper V, are investigated in this thesis. Simultaneously to the material gap, the pressure gap is addressed by exposing the materials to more realistic conditions using ambient pressure X-ray photoelectron spectroscopy, see Papers III and IV. This technique allows for measurements while the sample is exposed to different gases up to the lower mbar regime. By comparing X-ray photoelectron spectroscopy with standard UHV measurements major differences in the resulting surface oxide composition are observed. The thickness of the native oxide films of the different samples is determined by X-ray reflectivity measurements performed at different experimental conditions ranging from UHV to air and water environments, Papers I and IV. X-ray photoelectron emission microscopy and low-energy electron microscopy was used to follow the surface development during heating of aluminum and steel samples on a sub-micron length scale, Papers II, IV, and V. The microscopic imaging allows for the identification of the chemical state of the alloying elements and their lateral distribution in the surface layer. Overall, this thesis highlights the need to develop the surface science techniques, which are not commonly used in material science, further to allow measurements on industrial samples in more realistic environments.

List of Publications

This thesis presents my work concerning the surface development of model systems such as pure aluminum and industrial materials, aluminum alloys and duplex stainless steels, throughout heat treatment in different sample environments. To follow the change in the surface region several surface sensitive X-ray techniques were employed. The main focus of this thesis is to combine industrial samples with modern surface science techniques and adjust these techniques to allow experiments in realistic sample environments concerning pressure and temperature.

The thesis is composed of two parts. In the first part, the materials studied and the experimental methods used are introduced. The second part is a compilation of the publications that present the results obtained.

Parts of this thesis have previously been presented in my licentiate thesis *"Aluminum alloys and single crystals studied by XPEEM, XPS, and XRR"*.

This thesis is based on the following publications, referred to by their Roman numerals:

I **The thickness of native oxides on aluminum alloys and single crystals**

J. Evertsson, F. Bertram, F. Zhang, L. Rullik, L. R. Merte, M. Shipilin, M. Soldemo, S. Ahmadi, N. Vinogradov, F. Carlà, J. Weissenrieder, M. Göthelid, J. Pan, A. Mikkelsen, J.-O. Nilsson, E. Lundgren
Appl. Surf. Sci. **349** (2015) 826–832

I was involved in the measurements and discussion about the paper.

II **Surface development of an aluminum brazing sheet during heating studied by XPEEM and XPS**

L. Rullik, F. Bertram, Y. R. Niu, J. Evertsson, T. Stenqvist, A. A. Zakharov, A. Mikkelsen, E. Lundgren
Mater. Res. Express **3** (2016) 106506

I was responsible for the planning and performing the experiment. I analyzed the data and wrote the manuscript.

III **Surface development of a brazing alloy during heat treatment–a comparison between UHV and APXPS**

L. Rullik, N. Johansson, F. Bertram, J. Evertsson, T. Stenqvist, E. Lundgren
J. Phys.: Condens. Matter **30** (2018) 024004

I was responsible for the planning and performing the experiment. I analyzed the data and wrote the manuscript.

IV **Surface Oxide Development on Aluminum Alloy 6063 during Heat Treatment**

L. Rullik, J. Evertsson, N. Johansson, F. Bertram, J.-O. Nilsson, A. A. Zakharov, A. Mikkelsen, E. Lundgren
Surf. Interface Anal. (2018), *Submitted*

I was responsible for the planning and performing the experiment. I analyzed the data and wrote the manuscript.

V **Surface Development of Super Duplex Stainless Steel SAF 2507 during Heat Treatment**

L. Rullik, N. Vinogradov, J. Evertsson, E. Bettini, A. A. Zakharov, A. Mikkelsen, E. Lundgren
In manuscript

I was responsible for the planning and performing the experiment. I analyzed the data and wrote the manuscript.

Papers not included in this thesis, to which I have contributed:

VI **Integration of electrochemical and synchrotron-based X-ray techniques for in-situ investigation of aluminum anodization**

F. Zhang, J. Evertsson, F. Bertram, L. Rullik, F. Carlà, M. Långberg, E. Lundgren, J. Pan
Electrochim. Acta **241** (2017) 299–308

VII **Anodization of Al (100), Al (111) and Al Alloy 6063 studied in situ with X-ray reflectivity and electrochemical impedance spectroscopy**

J. Evertsson, F. Bertram, L. Rullik, G.Harlow, E. Lundgren
J. Electroanal. Chem. **799** (2017) 556–562

VIII **Observation of Pore Growth and Self-Organization in Anodic Alumina by Time-Resolved X-ray Scattering**

N. A. Vinogradov, G. S. Harlow, F. Carlà, J. Evertsson, L. Rullik, W. Linpé, R. Felici, E. Lundgren
ACS Appl. Nano Mater. **1** (2018) 1265–1271

IX **Self-organization of porous anodic alumina films studied in situ by grazing-incidence transmission small-angle X-ray scattering**

J. Evertsson, N. A. Vinogradov, G. S. Harlow, F. Carlà, S. R. McKibbin, L. Rullik, W. Linpé, R. Felici, E. Lundgren
RSC Adv. **8** (2018) 18980-18991

X **In-situ Synchrotron GIXRD Study of Passive Film Evolution on Duplex Stainless Steel in Corrosive Environment**

C. Örnek, M. Långberg, J. Evertsson, G. Harlow, W. Linpè, L. Rullik, F. Carlà, R. Felici, E. Bettini, U. Kivisäkk, E. Lundgren, J. Pan
Corrosion Science **141** (2018) 18-21

List of Abbreviations

AA	Aluminum alloy
AEY	Auger electron yield
ALUX	Aluminum oxides for processing and products
APXPS	Ambient pressure X-ray photoelectron spectroscopy
BCC	Body-centered cubic
BCT	Body-centered tetragonal
BFP	Back focal plane
BSE	Back scattered electrons
CA	Contrast aperture
DSS	Duplex stainless steel
EIS	Electrochemical impedance spectroscopy
ESCA	Electron spectroscopy for chemical analysis
FCC	Face-centered cubic
FWHM	Full width at half maximum
FY	Fluorescence yield
HCP	Hexagonal close packed
HV	High vacuum
IMFP	Inelastic mean free path
IP	Image plane
LEED	Low-energy electron diffraction
LEEM	Low-energy electron microscopy
MEM	Mirror electron microscopy
PEEM	Photoelectron emission microscopy
PES	Photoelectron spectroscopy
PEY	Partial electron yield
PREN	Pitting resistance equivalent number
SE	Secondary electrons
SEM	Scanning electron microscopy
SDSS	Super duplex stainless steel
SPELEEM	Spectroscopic photoemission and low-energy electron microscope
ST	Simple tetragonal
SV	Start voltage
TEY	Total electron yield
UHV	Ultrahigh vacuum
UV	Ultraviolet
XA	X-ray absorption
XAS	X-ray absorption spectroscopy
XAS-PEEM	PEEM in X-ray absorption mode
XP	X-ray photoelectron
XPEEM	X-ray photoelectron emission microscopy
XPS	X-ray photoelectron spectroscopy
XRR	X-ray reflectivity
XUV	Extreme ultraviolet

Populärwissenschaftliche Zusammenfassung

Nahezu alle metallischen Materialien, die wir heute anwenden, sind Legierungen. Der Grund hiefür liegt in deren, im Vergleich zu den einzelnen Legierungselementen, verbesserten physikalischen Eigenschaften wie Festigkeit, Verschleißbeständigkeit, Korrosionsbeständigkeit und Hochtemperaturverhalten. Legierungen aus Kupfer, Zinn und Zink werden schon seit ungefähr 2500 Jahren vor unser Zeitrechnung verwendet. Da die Wechselwirkungen zwischen den einzelnen Legierungselementen sehr komplex sind, versuchen sogar noch heute Forscher diese auf atomarem Niveau zu verstehen. Die hier vorliegende Arbeit beschäftigt sich hauptsächlich mit zwei Sorten von Legierungen: Aluminiumlegierungen und Stähle.

Da in beiden Legierungssorten die Korrosionsbeständigkeit von den Oxidschichten abhängt, werden in dieser Arbeit oberflächenphysikalische Messverfahren angewandt, um die chemische Zusammensetzung, die Dicke und die Verteilung verschiedener Phasen und Körner darin zu bestimmen. Die Spitzenforschung auf diesem Gebiet beschäftigt sich mit dem Übergang von Experimenten an vereinfachten Modellsystemen in gut kontrollierbaren Messumgebungen zu Messumgebungen, die denen der Industrie mehr ähneln.

Die in dieser Arbeit verwendeten Methoden haben gemeinsam, dass sie Elektronen und Röntgenstrahlen zur Charakterisierung der Oberfläche nutzen. Die Röntgenstrahlen werden dafür in einem kreisförmigen Teilchenbeschleuniger, einer sogenannten Strahlungsquelle, erzeugt. Synchrotronstrahlung wird hervorgerufen, wenn Elektronen, die in dem Beschleuniger Geschwindigkeiten nahe der des Lichtes haben, durch ein starkes Magnetfeld abgelenkt werden. Experimentelle Messstationen ermöglichen die Erforschung der industriellen Proben mit den unterschiedlichsten Methoden, wie unter anderem, die in dieser Arbeit besprochenen Methoden der Röntgenreflektometrie, Röntgenphotoelektronenspektroskopie und Photoemissionselektronenmikroskopie. Diese Messmethoden geben Informationen über die Dicke der Oxidschicht, die Elemente in ihr und deren chemischer Zustand sowie deren laterale Verteilung.

Die Erforschung des Einflusses der Probenumgebung auf diese Eigenschaften ist Teil des ALUX- (ALUminium oXides for processing and products) Projektes, in dessen Rahmen die vorliegende Arbeit angefertigt wurde. Das Projekt hat sich zum Ziel gesetzt, mit neuen Messmethoden und grundlegenden Theorien zur Entwicklung von Aluminiumprodukten mit verbesserter Vielseitigkeit und Korrosionsbeständigkeit beizutragen.

Um dies zu erreichen, haben sich experimentelle und theoretische Physiker mit der schwedischen Aluminiumindustrie innerhalb des ALUX-Projektes zusammengeschlossen. Während diser Zusammenarbeit hat sich ein Interesse an weiteren industriellen Materialien entwickelt. Daher beinhaltet diese Arbeit auch die Untersuchung von Stahlproben.

Meine Arbeit trägt zu den Zielen des ALUX-Projektes bei, indem sie klassische oberflächenphysikalische Methoden für die Charakterisierung von komplexen Aluminiumlegierungen und Stählen sowie deren Oxidschichten verwendet. Die Ergebnisse dieser Arbeit zeigen, dass große Unterschiede in der Dicke und der Zusammensetzung der Oxidschicht entstehen je nachdem ob die Probe in Ultrahochvakuum oder in industrienahen Probenumgebungen charakterisiert wurde. Daher ist es von großer Bedeutung, neue Messmethoden, wie z.B. Hochdruckröntgenphotoelektronenspektroskopie, zu entwickeln und diese zur Verbesserung des Verständnisses industrieller Materialien einzusetzen.

Populärvetenskaplig sammanfattning

Nästan alla metalliska material som används idag är legeringar. Detta beror på att legeringen har förbättrade fysiska egenskaper som hållfasthet, slitstyrka och korrosionsbeständighet och dessutom bättre prestanda vid höga temperaturer jämfört med de enskilda rena metallerna. Legeringar av koppar, tenn och zink har används sedan ungefär 2500 fvt men än idag försöker forskare utröna de komplexa växelverkningarna mellan legeringskomponenter på atomär nivå. I denna avhandling ligger fokus på två legeringsgrupper: aluminiumlegeringar och stål.

De båda legeringsgruppernas oxidskikt är avgörande då dessa bestämmer materialens korrosionsbeständighet. I denna avhandling har ytfysikmetodik använts för att undersöka den kemiska sammansättningen, tjocklek och fördelning av faser och partiklar inom dessa oxidskikt. Forskningsfältets framkant utmärks av försök att överbrygga skillnaden mellan förenklade modeller i välkontrollerade omgivningar och kommersiella legeringar med experimentförutsättningar som avspeglar de industriella villkoren.

De metoder som används i denna avhandling har gemensamt att de använder röntgenstrålar och elektroner för att karakterisera ytan. De röntgenstrålar som används genereras i en cyklisk partikelaccelerator som kallas synkrotron. Synkrotronljusstrålning uppstår när elektroner, som i acceleratorn har en fart nära ljusets, böjs genom ett starkt magnetfält. Experimentstationer tillåter forskning på industriella prover med olika metoder, så som röntgenreflektivitet, röntgenfotoelektronspektroskopi och fotoemissionselektronmikroskopi. Dessa metoder ger information om tjockleken på oxidskiktet, vilka ämnen som ingår i oxidskiktet samt deras kemiska tillstånd och fördelning på ytan.

Att studera hur materialets egenskaper förändras på grund av olika provmiljöer, till exempel tryck av olika gaser eller provtemperatur, är en del av ALUX-projektet (ALUminium oXides for processing and products) i vilket detta arbete utförts. Projektets mål är att använda nya mätmetoder och grundläggande teorier för att bidra till utveckling av produkter med förbättrad mångsidighet och korrosionsbeständighet. För att nå detta mål inleddes ett samarbete mellan experimentella och teoretiska fysiker och den svenska aluminiumindustrin i ett gemensamt projekt: ALUX-projektet. Under samarbetet inom ALUX-projektet utvecklades ett intresse att studera flera industriella legeringar och därför inkluderades också stål.

I detta arbete har vi försökt att nå vissa delmål inom ALUX-projektet, genom att tillämpa klassiska men också mer nyutvecklade ytfysikaliska metoder för karakterisering av komplexa aluminiumlegeringar och stål samt deras oxidskikt. Resultaten i avhandlingen visar att det finns stora skillnader i tjockleken och sammansättning på oxidskiktet mellan de klassiska experiment som utförs i ultrahögvakuum och de som används i mer industrilika provmiljöer. Därför är det av största vikt att utveckla nya mätmetoder såsom högtrycksröntgenfotoeletronspektroskopi och använda dessa nya metoder för att förbättra förståelsen av industriella material.

Acknowledgements

During the course of my PhD studies I met and worked with a lot of different people which all in one way or the other contributed to this thesis. I would like to take the opportunity to thank you all.

First of all, I would like to thank my supervisor, Edvin Lundgren, for being a supportive and encouraging teacher. You are always curious about new samples and interested in trying out different techniques to study them. I am very thankful for your trust in me and everything you though me about being a researcher. I gladly look back on all the measuring, traveling, discussing, analyzing, and presenting. Finally, I need to tell you, yes, bubbling beverages are simply better than the ones without bubbles.

I would also like to thank my co-supervisor, Anders Mikkelsen, for his help with mostly microscopy-related questions. Your door is always open if it is for a quick question or a long discussion about a lot of confusing images and how to make sense out of them.

The major amount of experiments I did together with Jonas Evertsson, Florian Bertram, and Nikolay Vinogradov. Thank you a lot for all the hours we shared measuring and fixing things in the lab. You also helped a lot with analyzing data and finally writing papers. When it comes to microscopy I would like to thank Alexei Zakharov and Yuran Niu for introducing me to the world of LEEM and PEEM. Thank you Alex for even helping me to measure on other instruments than yours. This brings me to the HERMES beamline at Soleil, where Rachid Belkhou, Sufal Swaraj, and Antoine Barbier helped me to get nice PEEM images of different steel samples. Thanks to Jan-Ingo Flege I also got fascinating *in-situ* LEEM movies on heated steels. I would also like to thank Milad Yazdi and Mats Göthelid for nice XPS beamtimes still at the old Max-lab. At the new MAX IV I got some APXPS 'anodetime' at the SPECIES beamline and I would like to than Samuli Urpelainen, Mikko-Heikki Mikkelä, and Esko Kokkonen for making that possible.

I would like to thank Torkel Stenqvist, Jan-Olov Nilsson, and Eleonora Bettini for providing me with samples and an insight into the Swedish metal industry. The visits at your companies really motivated me to tackle these complicated systems. With that I would also like to thank all members of the ALUX and the HEXCHEM projects for the nice workshops and the lively discussions about my data.

During my time as a PhD student I was a member of the ADMIRE graduate school and I would like to thank Maria Messing for coordinating it. I am very thankful for the graduate schools travel grants that allowed me to attend international conferences. The ADMIRE board, thank you all, gave me the opportunity to influence the development of courses and to gain insights into the university's administration as a student representative.

Handling administrative tasks without Patrik Wirgin, Anneli Nilsson Ahlm, and Anne Petersson would have been much harder. Thank you for always helping me with the paper work. For being uncomplicated when it comes to administrative questions I would like to thank the previous and current heads of the division, even though they seem to be multiplying.

I would like to thank all of my former and current colleagues at SLJUS for the great atmosphere at the division and lively discussion that regularly occur in the lunch room. The lunch room at SLJUS is always a good place for a fika and especially when sharing cakes and chatting about sometimes more or less scientific topics with Estephania Lira, Sarah McKibbin, and Milena Moreira. A lot of small things made the time as a PhD student at SLJUS fun, like discussing with Sara Blomberg how to transform manure into gold (or methanol), planning third oppositions with Payam Shayesteh, considering if owning a horse or at least a pony is an asset when searching for apartments in Lund with Uta Hejral, and dreaming about life as a free elf with Olesia Snezhkova and Andrea Troian.

I would also like to take this opportunity to thank my friends and family. A big thank you to Karolina and Kenneth for sharing drinks, food, travel, the passion for cottages and saabs, and even a mulltoa. The time in Lund without you would not have been half as weird and funny. I would like to thank my sister and my parents to always keep me connected to Germany. Thanks to all your messages, calls, and visits, Lund never felt really far from home. I would also like to thank Ann and Jörgen for making Småland my Swedish home.

Last but definitely not least, I need to thank you Niclas. You are my favorite co-author and you made me travel as far as Fuji for a date with you. It does not matter if we are building a bathroom for Trollheim or mounting samples, it is always more fun together with you. Thank you for always being there for me!

Industrial Alloys Studied by Surface Sensitive Techniques

1 Introduction

Mankind has been using materials such as wood, stones, ceramics, glass, metals and alloys for millennia. Over time the material properties were refined and the development of new materials had such a great impact on entire civilizations that even whole time periods of mankind's history are named after these materials, e.g., Chalcolithic[1] Period, the Bronze Age and the Iron Age. Depending on the use of materials their properties have been altered to accommodate for the changing needs of their users. To meet today's requirements on material properties, most metallic materials are alloyed.

The two material groups that are studied in this thesis are metal alloys: aluminum alloys and iron based alloys, steels. These two alloy groups are also the world's most important engineering materials. In 2017 the world's steel production was about 1.69 billion metric tons [1] and for aluminum it was about 53.5 million metric tons [2] making steel and aluminum the two most commonly produced metals.

The dominance of steels as a structural material is explain by several reasons. First of all, iron is the most abundant element on Earth by mass and even the fourth most common element in the Earth's crust. Further, even iron scrap, the second source for industrial production of steels, is cheap and widely available. The main reason for the popularity of steels as materials is however its multitude of properties. By changing the amount and composition of alloying elements in the steel production, a vast variety of steels grades can be produced with very different physical and mechanical properties, so that steels can be used as keys, frying pans, vacuum chambers, and as structural material in buildings ranging from stables to nuclear power plants.

The iron alloy that was studied in this thesis, SAF 2507, is a specialized alloy for applications in highly corrosive environments that belong to the group of super duplex stainless steels. Its excellent corrosion resistance in combination with its very high mechanical strength makes it suitable for tough applications such as in the oil and gas industry, pulp and paper production, and chemical processing. The reason for the excellent corrosion resistance of the steel is its surface oxide film which mainly consists of chromium oxide. This surface oxide film is also why it is very interesting to study steels from a surface science perspective as done in this thesis.

---

[1] Chalcolithic is derived from the Greek works $\chi\alpha\lambda\kappa\acute{o}\varsigma$ (chalcos) = copper and $\lambda\acute{\iota}\theta o\varsigma$ (lithos) = stone.

However, the main focus in this thesis is on aluminum alloys. These are of great industrial, economic and political interest as they can play an important role in achieving environmental targets set by governmental agencies such as the EU's 2050 vision. Aluminum can contribute to these goals in two sectors: industry and transportation. The aluminum industry can largely reduce its greenhouse gas emission by recycling aluminum scrap as the secondary production is about 90% more energy efficient than the production of primary aluminum from bauxite. However, for successful recycling the understanding of the impact of impurities on the performance of the alloys needs to be improved.

The other sector in which aluminum can contribute to the environmental target is transportation. Currently the demand on the transportation industries to create less emission leads to the increased interest in light weight structural materials. These demands can be met by the use of aluminum alloys due to their high strength-to-weight ratio. In addition, just as with steels, aluminum alloys have a good corrosion resistance due to their native aluminum oxide film, which is about 5 nm thick.

Although great for corrosion resistance, the aluminum oxide film is a major obstacle when it comes to joining work pieces made of aluminum or aluminum alloys. To achieve good wetting of the two surfaces by the filler material, see Papers II and III, the oxide layer has to be removed. However, pure aluminum oxide has a high melting point (2072°C) and very good adherence to the underlying aluminum.

One method of removing the oxide is flux brazing. This approach is problematic since furnace brazing with a flux contains vapor of dilute hydrochloric acid with minor amounts of hydrofluoric acid which creates a considerable amount of problems regarding work safety, environmental issues, and corrosion at the furnace. Another method is vacuum brazing which has been used for a number of specialized applications such as in the aerospace industry. In the 1980s, aluminum products were increasingly considered for the automotive industry which lead to the development of furnace brazing with a flux under a protective atmosphere of nitrogen, known as the NOCOLOK process [3].

To understand changes in the microstructure during industrial relevant processes like heat-treatment, anodization, and corrosion, *ex-situ* studies on model systems are not sufficient. Investigating industrial processes under (or close to) realistic conditions can yield more relevant information although such studies increases the complexity of the experimental setup and data analysis.

Using actual industrial materials instead of model systems introduces a number of challenges. For instance, using composite aluminum alloys instead of single crystals, more elements and structures in the sample have to be considered. The inhomogeneity of industrial samples with respect to microstructure, precipitates, constituent particles is also significant. Further, it is necessary to consider that each batch has a composition that is slightly deviating from the nominal composition.

To overcome all these challenges, a unique constellation from Swedish academia and aluminum industry has been assembled under the SSF-program *ALUminium oXides for processing and products* (ALUX) [4]. This project aims for an improvement of the corrosion resistance and versatility of aluminum products by combining the different skills from industry, theory and experimental science.

My contribution to this project is within the experimental area as I am applying a range of electron and synchrotron-based X-ray techniques for spectroscopy, microscopy and diffraction experiments to study aluminum alloys and steels. This thesis introduces a variety of aluminum based samples and steels in chapter 2 as well as electron and synchrotron-based X-ray techniques in chapter 3 to provide a background for the appended publications. The last chapter provides an outlook on how the gained insights can be transferred to future experiments.

2 Materials

In this thesis, two material groups have been studied: Aluminum alloys and duplex stainless steels. The first part of this chapter introduces the different types of aluminum samples that have been investigated. The first section, 2.1.1, focuses on the properties of pure single crystal and polycrystalline aluminum. Due to aluminum's high oxygen affinity it is almost always covered by a layer of aluminum oxide. Therefore, aluminum oxides and their relevance with respect to industrial processes will be discussed in section 2.1.2. Moving towards more applied samples, section 2.1.4 introduces the standards for wrought aluminum alloys with a special emphasis on the role of the different alloying elements and the effects of heat treatment of aluminum alloys. The last aluminum related section, section 2.1.4.3, will explore the complicated interaction within composite aluminum alloys designed for brazing applications.

The second part of this chapter will give a brief introduction to the wide field of steels with focus on duplex stainless steels. To understand the differences between the steel grades it is important to understand the role of the alloying elements as they stabilize different phases. This is discussed in section 2.2.1.2. Since the phases found in duplex stainless steels are dependent on the heat treatment, the effect of heat treatment is discussed in the last section.

2.1 Aluminum

Aluminum is the third most abundant element in the earth's crust. Despite its great abundance, aluminum was not recognized as an element until the Danish physicist and chemist Hans Christian Ørsted succeeded in producing minor amounts of metallic aluminum by reacting potassium amalgam with anhydrous aluminum chloride. Later, in 1827, the German chemist Friedrich Wöhler succeeded in preparing the first pure sample of aluminum powder by using potassium and aluminum chloride [5].

A possible reason for the late discovery of aluminum may be due to its chemical properties. Aluminum is very reactive when exposed to air and hence, it is almost only found in its various forms of oxide and silicate compounds. The high oxygen affinity of aluminum is the reason for the occurrence of its surprisingly adherent passive oxide film which is the foundation for its well-known corrosion resistance.

To improve commercial aluminum products, the fundamental understanding of the interaction between aluminum and its alloying elements and the formation

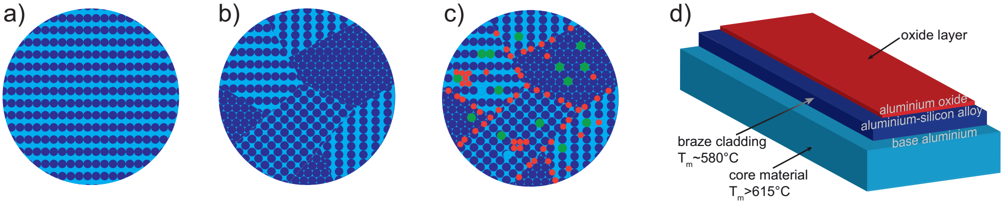

Figure 1: Models of a) an FCC(110) single crystal surface, b) a polycrystalline sample with different surface orientations, c) a polycrystalline alloy with alloying elements at the surface, and d) model of a composite material, here a brazing sheet consisting of two different aluminum alloys. These models illustrate how the structures increase in complexity and hence create more challenges during data acquisition and analysis.

of the protective oxide layer on its surface needs to be understood. The oxide formation on aluminum has been studied for decades with a variety of surface science techniques, e.g. [6–12]. One major drawback with the conventional surface science approach is the use of model systems in controlled environments. Aluminum single crystals have been studied extensively but questions about the influence of alloying elements, heating and aqueous environments on the microstructure remain. Therefore, this thesis is aiming to extend the classical surface science approach by moving towards industrial alloys. Fig. 1 describes this transition graphically and illustrates how the complexity of the system increases and hence the demands on the experimental setup and data analysis.

2.1.1 Pure Aluminum

The crystal structure of pure aluminum is face centered cubic (FCC). The melting point of pure aluminum is 660°C and its density is low, ρ=2.7 g·cm^{-3}, which is about a third of the density of iron [13, 14]. This makes aluminum and especially it's alloys a light-weight structural material.

As previously mentioned, a characteristic property of aluminum is its strong affinity to oxygen. Therefore, the most common ore of aluminum consists of a mixture of aluminum oxide, aluminum hydroxides, and oxyhydroxides. This type of ore is called bauxite, which also contains varying amounts of iron oxides and silicates.

Bauxite can be converted to aluminum oxide via the Bayer process [15]. In the Bayer process the aluminum oxide contained in the bauxite reacts with sodium hydroxide in a pressure vessel at a temperature of 150-200°C to form sodium aluminate. By cooling the filtered solution and passing carbon dioxide through it, aluminum hydroxide precipitates. Today it is more common to use a supersaturated solution of sodium aluminate seeded with aluminum hydroxide crystals to precipitate aluminum hydroxide, which is transformed into aluminum oxide by heating.

The resulting alumina is then smelted by electrolytic reduction, known as the Hall–Héroult process [16]. The Hall–Héroult process uses cryolite, Na_3AlF_6, to lower the melting point of alumina. Since the Hall–Héroult process requires large quantities of energy, recycling plays an important role in the aluminum industry today. The production of secondary aluminum only requires about 90% of the energy used in producing aluminum from its ore.

2.1.1.1 Single Crystals

To study pure aluminum it is often used in the form of a single crystal. Single crystals are grown artificially by controlled phase transformation from the disordered liquid phase. They are common substrates for surface science studies since the geometrical arrangement of the atoms is clearly defined. This is the case because a crystal consists of atoms or a group of atoms arranged in a periodically repeating pattern in three dimensions.

The entire structure of a single crystal can be constructed by a translational displacement of the smallest repeating entity, the so-called unit cell. The unit cell is defined by its lattice parameters, the lengths a, b, c of the three independent cell edges and the angles α, β, γ between these edges. Using the lattice vectors $\overrightarrow{a}$, $\overrightarrow{b}$, $\overrightarrow{c}$ and translations operations the entire crystal structure can be defined by Eq. 1.

$$\overrightarrow{R} = n_1\overrightarrow{a} + n_2\overrightarrow{b} + n_3\overrightarrow{c} \quad \text{,where } n_1, n_2, n_3 \in \mathbb{Z} \tag{1}$$

Originating from a lattice point, the positions of all atoms inside the unit cell are described by a set of vectors, see Eqn: 2.

$$\overrightarrow{r} = x\overrightarrow{a} + y\overrightarrow{b} + z\overrightarrow{c} \quad \text{,where } 0 \leq m, n, o \leq 1. \tag{2}$$

The crystal structure of most metals is cubic, thus the unit cell parameters are equal, i.e. $a = b = c$, and the angles are $\alpha = \beta = \gamma$=90°. By adding an atom in the center of the simple cubic unit cell (SC), see Fig. 2 a), a body centered unit cell (BCC) is formed as shown in Fig. 2 b). Aluminum has a FCC lattice and therefore atoms are not only placed on the corners of the unit cell but also at the center of each of the six faces, see Fig. 2 c).

Other examples of metals with a FCC crystal structure are nickel and copper. Iron, manganese, chromium, and molybdenum are typical metals that have a

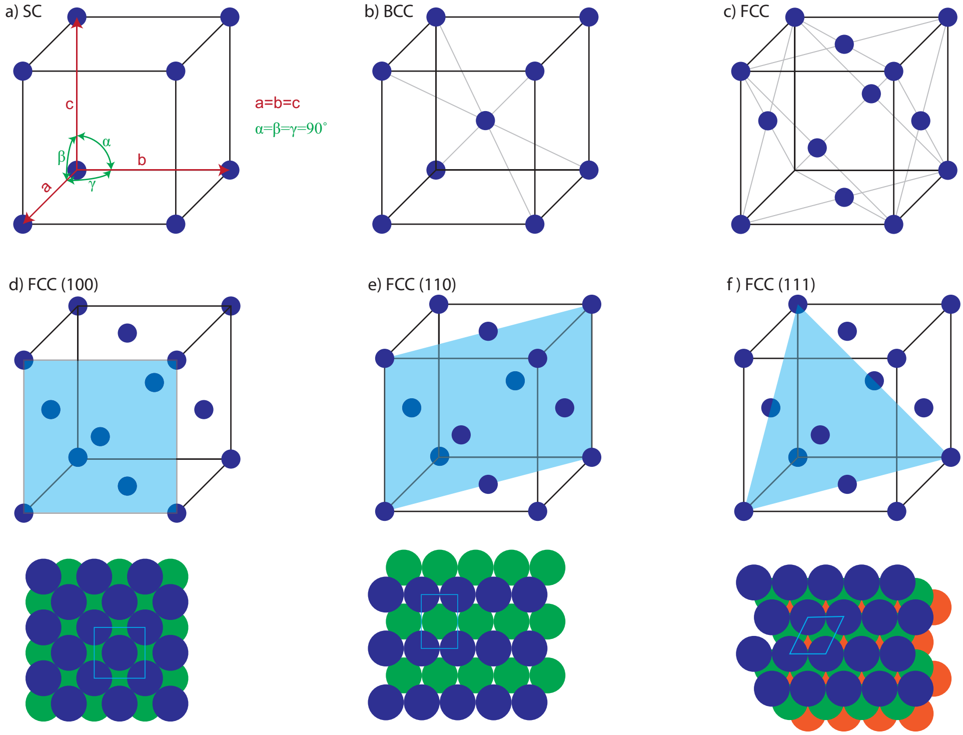

Figure 2: Illustrations of cubic units cells a) simple cubic, b) body centered cubic, c) face centered cubic and low index crystal planes d) (100), e) (110), f) (111) in a FCC crystal structure and the corresponding surfaces. In a cubic unit cell the cell parameters are equal (a=b=c) and the angles are $\alpha = \beta = \gamma = 90°$. The light blue lines in the bottom models describe the primitive surface unit.

BCC crystal structure. Another common crystal structure is hexagonal close packed (HCP), see Fig. 7, it is observed in, e.g. magnesium and titanium.

The structure and orientation that a single crystal exhibits at the surface depends on how the crystal is cut with respect to the crystal planes. In surface science the conventional way of denoting crystal planes is by the inverse of the interception between crystal plane and the coordinate axes defined by the lattice vectors. This index of the plane is represented by the three smallest integer combination in brackets (hkl). These indices are also referred to as Miller indices. Miller indices only containing values of one and zero are called low index planes. The three low index planes of a FCC crystal are shown in Fig. 2 d)-f).

2.1.1.2 Polycrystalline Aluminum

The prefix *poly* come from ancient Greek $\pi o\lambda \upsilon \varsigma$ (polús) meaning many or much, hence polycrystalline aluminum consist of many entities of crystalline aluminum. The main difference between single crystal and polycrystalline aluminum is the presence of grain boundaries and different surface planes. Therefore, the mechanical and corrosion properties are different in comparison to single crystals.

The grain size in polycrystalline aluminum varies greatly depending of the history of the sample (annealing, rolling, etc.) and can range from a few μm to several mm. The surface of a polycrystalline aluminum sample can exhibit random orientations for each single grain or the same orientation but laterally rotated towards each other. However, surface atoms can reconstruct from open to more close-packed arrangements to lower their surface energy. Samples of polycrystalline aluminum can be used as an intermediate step towards industrial materials since they contain grains and grain boundaries but no alloying elements.

2.1.2 Aluminum Oxide and Hydroxides

Due to aluminum's high oxygen affinity it will form aluminum oxides as soon as aluminum is exposed to an oxygen containing environment. This effect is explained by the large negative Gibb's free energy [17] for the reaction of aluminum with oxygen:

$$2\mathrm{Al(s)}+\frac{3}{2}\mathrm{O_2(g)} \rightarrow \alpha - \mathrm{Al_2O_3(s)}\ ; \Delta G^\circ = -1583\ \mathrm{kJ/mol} \tag{3}$$

or the reaction of aluminum with water:

$$2\mathrm{Al(s)}+3\mathrm{H_2O(l)} \rightarrow \mathrm{Al_2O_3(s)} + 3\mathrm{H_2(g)}\ ; \Delta G^\circ = -871\ \mathrm{kJ/mol.} \tag{4}$$

The thermodynamically stable and most dominant crystalline form of aluminum oxide is α-Al_2O_3 also referred to as corundum [18]. The structure of α-Al_2O_3 is described as an HCP sublattice of oxygen anions with aluminum cations filling two thirds of the octahedral sites [19]. The lattice parameters of the unit cell are $a = b = 4.7589$ Å and $c = 12.991$ Å. An illustration of the α-Al_2O_3 unit cell is shown in Fig. 3.

Aluminum can form a range of metastable oxides. According to their arrangement of the oxygen anions these can be divided into two subgroups, FCC and HCP. The different polymorphs of each of these two subgroups are obtained by varying the distribution of aluminum cations. Aluminum cations usually occupy octahedral or tetrahedral interstitial sites within the oxygen lattice. The close packing of four spheres creates a tetrahedral interstitial site and the closed packing of six spheres gives an octahedral site. Alumina structures based on HCP packing of oxygen besides α-Al_2O_3 include κ-(orthorhombic) and χ-(hexagonal)

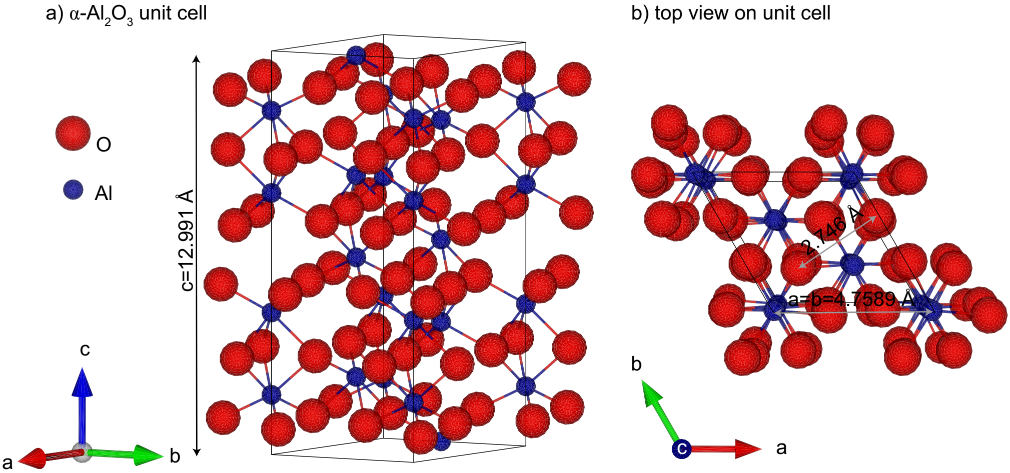

Figure 3: a) Unit cell of $\alpha{-}Al_2O_3$ which consists of a HCP sublattice of oxygen anions and 2/3 of the octahedral sites filled with aluminum cations. b) gives a top view of the unit cell marking the lattice parameters a and b as well as the interatomic distance for the oxygen in the unit cell. Oxygen anions are represented in red and aluminum cations in blue. Illustration created by using VESTA [20] and the crystallographic data can be found in Ref. [19].

phases. Examples of FCC based alumina structures are γ-, η (cubic) and θ-(monoclinic) phase.

Aluminum forms besides the oxides a wide range of hydroxides. Gibbsite and Bayerite are the most common structures of aluminum trihydroxides, $Al(OH)_3$ whereas Boehmite and Diaspore are frequent monohydroxides, AlOOH [18]. Aluminum hydroxides typically consist of stacked oxygen double layers (O-Al-O) with aluminum occupying the octahedral interstitial sites. The hydrogen is usually arranged between the adjacent oxygen layers.

2.1.3 Native Aluminum Oxide Films

The above described aluminum oxides all exhibit a well defined chemical and crystallographic structure. The native aluminum oxide films found on aluminum alloys are usually amorphous and vary depending on the underlying alloy. Hence, they are not well described by conventional techniques for structural analysis. Nonetheless, these amorphous oxides play an important role concerning cohesion and stability of the interfacial bonding between the metallic aluminum and its protective oxide layer. Due to the strong cohesion between metal and oxide, aluminum has a naturally occurring abrasion and corrosion protection, which makes it a very utile material.

The native aluminum oxide film, grown under room temperature and atmo-

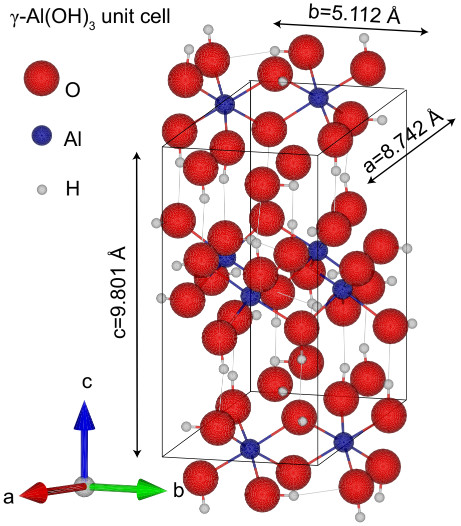

Figure 4: Model of a Gibbsite, $\gamma Al(OH)_3$, unit cell. Illustration was created by using VESTA [20] and the crystallographic information can be found in Ref. [21].

spheric pressure, has a thickness ranging from 2-7 nm [22]. It is usually described as an amorphous film which contains different amounts of ordered oxide and hydroxide patches. By growing the aluminum oxide film at elevated temperatures the amorphous oxide growth begins to compete with the growth of γ-Al_2O_3 since the Gibb's free energies of formation become nearly equal. Further, crystalline aluminum oxide is more likely to form on more densely packed surfaces of the substrate, hence more γ-Al_2O_3 develops on Al (111) than on Al (100) or Al (110) [23].

The native aluminum oxide film provides aluminum products with a good corrosion resistance since the interface layer between aluminum and the oxide, the so-called barrier layer, has a very low conductivity for both electrons and ions which makes it an insulator for electrochemical reactions. If mechanical damage to the oxide layer occurs, it regrows immediately. The passive oxide film is essentially insoluble in pH-values ranging from 4 to 9. However, the exposure to corrosive environments, eg. seawater containing chlorides and sulfates, can lead to localized corrosion [24].

The corrosion protection in harsh environments can be improved by increasing the thickness of the alumina films, which can be realized by anodic anodization. During anodization, aluminum is immersed into an acid electrolyte as part of an electrochemical cell. By applying an electric potential a thicker oxide layer is grown. Anodization of aluminum provides industry with a process to enhance the abrasion and corrosion resistance. Further, the approach provides a product finish with a high thermal stability. However, the excellent stability of alumina imposes a drawback in other applications of aluminum and its alloys.

In this thesis, one common application where the stability of alumina is an obstacle is investigated: brazing, see Papers II and III. During brazing the filler metal is heated above its melting temperature, for aluminum alloys around $580°C$, between the work pieces. Then the filler is left to solidify into a joint between these work pieces. The major challenge for creating a good joint is to obtain a smooth continuous filling. This is only possible if the aluminum oxide covering the faying surface is broken up, so that the molten filler can easily wet the surfaces.

When considering an aluminum oxide film on aluminum, the alumina can only be broken by the difference in the thermal expansion coefficients since the liquidus of alumina is above 2000°C. The thermal linear expansion coefficient for aluminum is $23.1 \cdot 10^{-6}\mathrm{K}^{-1}$ and of alumina $8.1 \cdot 10^{-6}\mathrm{K}^{-1}$ at 25°C [25]. Hence, cracks in the aluminum oxide film will occur during heating.

The break-up of the aluminum oxide layer on aluminum alloys is influenced by several factors. First of all, the alloying elements change the thermal expansion behavior of the substrate. Secondly, alloying elements can act like dopants within the aluminum oxide film which affects the thermal stability of the film. Thirdly, alloying elements can diffuse towards the interface between alloy and oxide film, form particles, react with the oxygen in the film, and thereby expand and burst the oxide film. Further, the sample environment influences these segregation behavior of the alloying elements in various ways. Each alloying element can therefore influence the way the alumina film is decomposing. Previous studies, e.g. [26, 27], and the research presented in Papers II and IV show a major role of magnesium on the aluminum oxide break-up. The next section gives a general introduction to aluminum alloys and the influence of the alloying elements on the material properties of the alloy.

2.1.4 Aluminum Alloys

By increasing the complexity of the studied material further than polycrystalline samples with oxide layers on the surface one arrives at the actual industrial alloy. The main reason for alloying metal is to improve the physical and mechanical properties. Typical alloying elements for aluminum alloys are copper, manganese, silicon, magnesium, iron, and zinc.

Alloying requires that aluminum and the various alloying elements are mixed thoroughly while in a molten state. Common aluminum alloys contain up to 15 wt.% of total alloying elements. Aluminum alloys are separated into cast and wrought products. Wrought aluminum alloys, e.g. rolled plate, foils and extrusions, are grouped into different series depending on their main alloying elements. The series of the alloy determines the first of an assigned four-digit number, which identifies all industrial standard wrought aluminum alloys. Tab. 1 gives an overview over the different series. Each of the different standards has a defined composition range and hence characteristic properties.

To select the most suitable alloy for a distinct application in for example transportation, construction, or packaging one needs to consider other factors besides the chemical composition. These include amongst others if there is a possibility of strengthening the alloy in various ways, in which environment the alloys will be used, and if and how single workpieces should be joined.

The following sections will give an introduction to these considerations starting with the diverse roles of the alloying elements and continuing with how the alloys can be strengthened with a special focus on heat treatment. Finally the influence of the previous factors on the corrosion properties will be discussed.

Table 1: The Aluminum Association [28] alloy designation system for wrought alloys.

Series	Major alloying elements	Heat treatable
1XXX	Al$\geq$ 99%	no
2XXX	Al-Cu-(Mg)	yes
3XXX	Al-Mn	no
4XXX	Al-Si	no/yes
5XXX	Al-Mg	no
6XXX	Al-Mg-Si	yes
7XXX	Al-Zn-(Mg)-(Cu)	yes
8XXX	Al-(other elements)	yes/no

2.1.4.1 Role of Alloying Elements

By adding a certain amount of different alloying elements, properties such as strength, density, workability, electrical conductivity, and corrosion resistance are greatly influenced. However, not all elements in the alloy are deliberate additives but are rather impurities from the production or traces from the recycling process. Tab. 2 gives an overview of the nominal composition of the different aluminum alloys used in the papers included in this thesis.

Iron is the most common impurity in aluminum products. The iron contamination originates from the aluminum ore, which contains iron oxides, and from ferrous containers and tools used in the production. Iron has a high solubility in molten aluminum and therefore contamination easily occurs during the hot stages of production. On the other hand, the solubility of iron in solid aluminum is very low, which makes iron form intermetallic particles often in combination with aluminum and silicon. In some alloys of the 1XXX series, iron is added intentionally to increase its strength slightly [13]. If iron and silicon are present in the alloy, AlFeSi intermetallic particles form, whose exact compositions and impact on the corrosion behavior are under discussion [29, 30].

Silicon is the main alloying element of the 4XXX series. It is commonly added to aluminum alloys to lower their melting point and to improve the fluidity of the melt and therefore silicon is often found in cast alloys but it also used in braze claddings or welding wires. Silicon has a low solubility in aluminum at room temperature and at 12.5 wt.% silicon forms a eutectic with aluminum [13]. In the 6XXX, series silicon and magnesium are the main alloying elements. Levels up to 1.5 wt.% are used to produce Mg_2Si (magnesium silicide) precipitates during age hardening, where the fine precipitates increase the strength [5].The intermetallic Mg_2Si-particles can however also influence the local corrosion or anodization of aluminum alloys [30].

Magnesium is also used on its own as a major alloying element in the 5XXX series. Maximum 17.4% of magnesium can be dissolved in aluminum [13] but usually not more than 5.5% of magnesium are used in wrought aluminum alloys. Due to the high solubility of magnesium, the alloys can be strengthened by solid solution hardening. By this treatment, aluminum-magnesium alloys obtain their high strength and corrosion resistance. Aluminum alloys containing more than 3% of magnesium have a tendency to precipitate the intermetallic compound β-Al_8Mg_5 at grain boundaries [14].

Table 2: Chemical composition of aluminum alloys which were investigated in this thesis. FA7856 and FA7825 are custom made alloys used in brazing sheets. Quantities given in wt.%. Aluminum is remainder for all alloys.

	Si	Fe	Cu	Mn	Mg	Cr	Zn	Ti	Bi
AA 6005	0.50-0.90	0.35	0.30	0.50	0.40-0.70	0.30	0.20	0.10	–
AA 6060	0.03-0.60	0.01-0.30	0.10	0.10	0.35-0.60	0.05	0.15	0.10	–
AA 6063	0.02-0.60	0.35	0.10	0.10	0.45-0.90	0.10	0.10	0.10	–
AA 7075	0.40	0.50	1.2-2.0	0.30	2.1-2.9	0.18-0.28	5.1-6.1	0.20	–
FA 7856	9.7	0.22	–	–	0.67	–	–	–	0.08
FA 7825	0.16	0.22	0.33	0.83	0.23	–	–	0.16	–

Other important alloying elements include copper, which increases strength and hardness, chromium, which is used in aluminum-magnesium alloys to prevent grain growth and recrystallization in aluminum-magnesium-silicon during heat treatment. However, an excess of chromium (Cr>0.35%) leads to the formation of coarse constituents with other alloying elements. Manganese is used to produce moderate strength non-heat treatable alloys of the 3XXX series. The combination of zinc with other alloying elements such as copper and magnesium leads to high strength heat treatable alloys.

The impact of alloying elements within the bulk on the mechanical properties of aluminum alloys has been studied extensively because of its industrial importance. The local effect of the various alloying elements on the surface layer has however not been investigated equally thorough. This is surprising, since the understanding of the surface behavior is important for applied processes such as abrasion, anodization, brazeability, corrosion, coating, and optical appearance amongst others. To gain more relevant information on the behavior of the oxide film, recent studies focused on conducting experiments *in-situ* during anodizing, heating or in contact with liquids [30–34].

2.1.4.2 Strengthening

To create alloys with the optimal physical, mechanical and technological properties, e.g. machinability and weldability, mechanical and thermal treatments are applied to aluminum alloys. To distinguish which of the several strengthening methods was applied to the alloy, temper designations are used. F marks alloys that are kept as fabricated whereas O stands for annealed wrought alloys. The temper designation H indicates strain hardening, which is a common way of strengthening non-heat treatable aluminum alloys. Strain hardening, which is also referred to as work hardening, moves dislocations, and induce changes within the crystal structure, by plastic deformation to increase the strength. The grain size is changed by strain hardening, too.

Solid solution strengthening is based on internal strains that are generated when atoms of one metal are introduced into the crystal lattice of another metal. The solute atoms can either occupy interstitial sites or they can substitute for solvent atoms in the lattice site. The factors governing the substitutional solubility in alloys are commonly referred to as the Hume-Rothery rules. They state that the size difference between the two atoms should be 15% or less, the crystal structure should be similar, and valency and electronegativity should be similar to be soluble in a larger extent [14]. The strengthening effect, on the other hand, is greater if the difference between the atomic radii is dissimilar because it poses a larger strain in the lattice.

The solubility of other phases in aluminum is crucial to precipitation strengthening which can be part of a heat treatment and therefore has the temper designation T. Wrought alloys from the 2XXX, 6XXX, and 7XXX series are often age hardened. A typical precipitation hardening system in aluminum alloys is the β-Mg_2Si-system [35]. In precipitation strengthening a second phase is dissolved in the aluminum by heating the alloy and then rapidly quenching it to create a supersaturated alloy. By holding the supersaturated solid solution at a temperature below the solvus, which defines the limit of solid solubility, the second phase will try to reach equilibrium and thus start precipitating. This process is also refereed to as aging. If the alloy is kept at a too high temperature, coarse precipitates can form that do not result in the desired strengthening effect. Fig. 5 shows a schematic representation of precipitation strengthening. Common precipitates for alloys of the 6XXX series are Mg_2Si and FeSiAl particles. The 7XXX series forms amongst others $MgZn_2$ and Mg_2Si [14]. The particles forming during heat treatment of AA 6063 are studied in Paper IV.

Other particles influencing the strength and other properties are dispersoids and constituent particles. Dispersoids are particles comprised of elements that have a very low solubility in aluminum. Their typical size ranges from 0.05-0.5 μm. Constituent particles are much larger, reaching sizes of 10 μm. They are formed most often by alloying elements such as iron, silicon, manganese, and magnesium.

The occurrence of any of the described particles can greatly influence the strength of aluminum alloys but they also affect the oxide layer growth if they are formed in the surface near region.

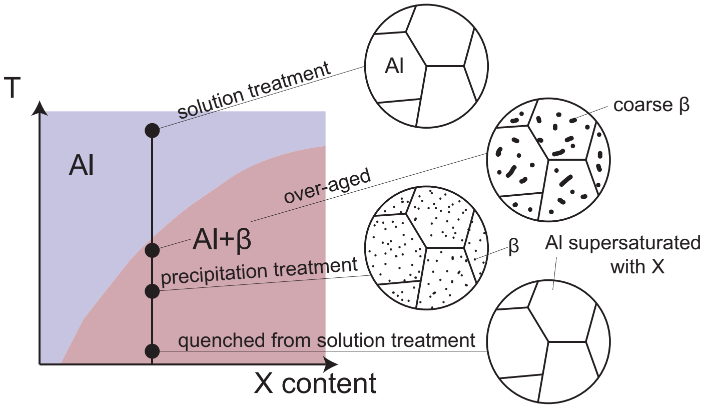

Figure 5: Generic phase diagram representing the different stages of a solution treatment followed by a rapid quenching and aging. By heating an aluminum alloy above the solvus temperature, a second phase, here shown as β, can dissolve in it. This second phase can be retained in the solution by rapid quenching and aged at a specific temperature to form precipitates of the desired size. If the second phase forms coarse precipitates the alloy is called over-aged.

2.1.4.3 Brazing Sheets

The joining of work pieces can be achieved by different processes, e.g. mechanical joining and adhesives. Hot joining processes for metals include soldering, brazing, and welding. Brazing is defined as a hot joining process in which temperatures above 450°C but below the solidus, the highest temperature at which a phase is completely solid, of the parent material are used. It is used in applications that require a permanent joint with similar strength and thermal conductivity to the parent material. Work pieces with either very thin or very thick cross sections or assemblies with a large number of joints as found in heat exchangers, see Fig. 6 b), are also often brazed.

A typical brazing sheet is a composite material which consists of a core alloy and a braze cladding. The core has a higher melting temperature and therefore can maintain the structure while the braze cladding can be melted selectively. The liquid phase is then drawn between the different close-matched work pieces by capillary forces. Upon cooling, a solid joint between the workpieces is formed by the braze cladding.

For aluminum alloys the braze cladding typically consists of an aluminum-silicon alloy as the silicon lowers the melting temperature. The surface of the brazing sheet is covered by a native aluminum oxide film, see Fig. 6 a). The aluminum oxide has a greater thermal stability than both the braze cladding and the core alloy and therefore, it is important to know at which temperature the aluminum oxide layer breaks up and how the surface changes during melting of the braze cladding. This is the case since the surface has a major influence on the wetting, the ability of the liquid phase to stay in contact with the solid phase, and the capillary effects, which pull the liquid into the space between the work pieces.

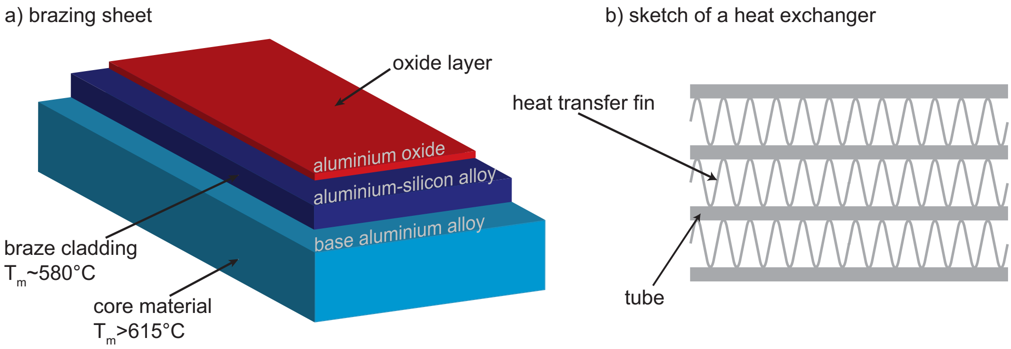
a) brazing sheet

b) sketch of a heat exchanger

Figure 6: a) Illustration of a typical composition of a brazing sheet and b) sketch of assembly of brazing sheets for a heat exchanger which can be found e.g. in heat exchangers in cars.

Brazing of aluminum can be done either with a flux or in vacuum. Fluxes can be applied to the brazing alloy in form of a powder, a paste, a liquid, or vapor. They are applied to the brazing sheet to remove the surface oxide layer. Vacuum brazing is considered to be a fluxless brazing method which is performed in vacuum furnaces that maintain pressures around 10^{-5} mbar. The advantages of vacuum brazing are the absence of corrosive fluxes in the furnace, the possibility to form a large number of joints, the option to perform hardening in the same furnace, and the high repeatability of the brazing result.

The brazing sheets that were investigated in this thesis are designed for vacuum brazing. This particular composite alloy finds application in heat exchangers. How the single brazing sheets can be assembled to form parts of a heat exchanger is shown in Fig. 6 b). The composition of the brazing sheet is given in Tab. 2. There it is shown that the braze cladding FA7856 has a significantly higher content of silicon and magnesium than the core material FA7825. Silicon was added to the braze cladding to lower the liquidus and magnesium is needed for facilitating the decomposition of the aluminum oxide film. Papers II and III of this thesis follow the break-up of the oxide during heat treatment.

2.2 Iron and Stainless Steels

Iron is the most important base metal for structural and magnetic materials. It undergoes two phase transitions when heated. At normal pressures, ferrite is transformed into austenite at 911°C,

$$\alpha(\mathrm{BCC}) \leftrightarrow \gamma(\mathrm{FCC}),\ \text{at } 911^\circ\mathrm{C} \tag{5}$$

further heating leads to the transformation of austenite into delta iron,

$$\gamma(\mathrm{FCC}) \leftrightarrow \delta(\mathrm{BCC}),\ \text{at } 1392^\circ\mathrm{C} \tag{6}$$

which is structurally indistinct from α-ferrite. For sketches of BCC and FCC unit cells, see Fig. 2. The δ-ferrite remains the stable phase in normal pressure until melting at 1536°C.

A magnetic phase transition occurs at 769°C,

$$\alpha_{\text{ferromagnetic}} \leftrightarrow \alpha_{\text{paramagnetic}},\ \text{at } 769^\circ\mathrm{C}, \tag{7}$$

which previously was incorrectly thought to be the β allotrope of iron. A HCP phase, see Fig. 7, of iron exists at elevated pressures [36].

The different phases of iron and their transitions are the foundation for the wide range of microstructures in steels resulting in a variety of properties. Since allotropic transitions in steels can occur in different ways, displacive or reconstructive, structures like the body centered tetragonal (BCT) martensite can be formed, see Fig. 7 b).

The need for a higher corrosion resistance in steels led to the development of stainless steels, which were invented in the beginning of the 20th century. Ever

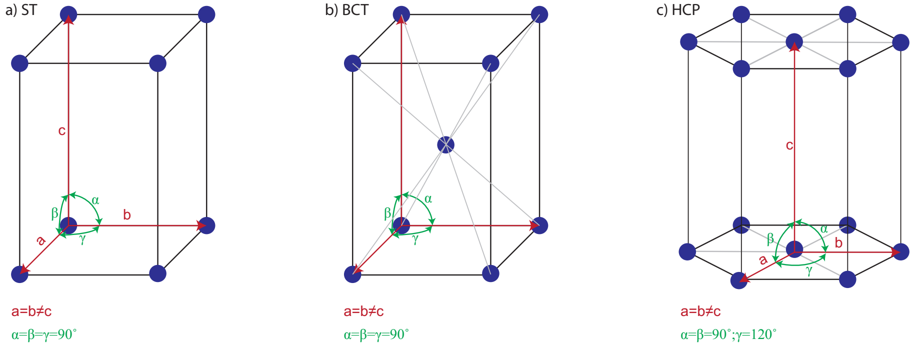

Figure 7: Illustrations of a) simple tetragonal, b) body centered tetragonal, and c) hexagonal closed packed unit cell. In a tetragonal unit cell only two cell parameters are equal (a=b) as in comparison to cubic units cells shown in Fig. 2. However the angles are the same as in a cubic unit cell with $\alpha = \beta = \gamma = 90^\circ$.

since, their technical importance has lead to numerous research efforts, as shown in this review [37]. Their characteristic chromium content of at least 13 wt.% gives them their excellent corrosion properties.

Their high corrosion resistance originates from, just as for aluminum alloys, the spontaneously formed passive oxide film. Here it is, however, a chromium oxide and hydroxide based film. The corrosion resistance of stainless steels can further be increased by the addition of other alloying elements such as nickel, molybdenum, tungsten, manganese, silicon, copper, cobalt, aluminum, and nitrogen. Through the addition of more alloying elements, the interaction between the single additions must be considered.

Today there are numerous steel grades created for various applications, which all exhibiting different compositions, microstructures and physical properties, are standardized worldwide. To be able to group them roughly together, they are typically divided in three groups based on their chemical composition: carbon steels, low-alloy steels, and high-alloy steels. Of these three groups the carbon steels are the by far most produced type of steel. They contain maximum 1% carbon and have restrictions on how much of other alloying elements can be contained in the composition. Low-alloy steels reach a content of alloying elements up to 8% as any composition containing more alloying elements is regarded as a high-alloy steel [36].

As stainless steels require a chrominum content above 8%, they belong to the group of high-alloy steels. Stainless steels are commonly subdivided into four groups based on their microstructure: ferritic, austenitic, martensitic, and duplex (α and γ). Two other common groups of stainless steels include precipitation hardening stainless steels and Mn-N substituted austenitic stainless steels [37].

All these different kinds of stainless steels are obtained by slightly changing the amount of alloying elements, which results in the stabilization of different phases. This enables the production of a wide range of steel grades, each having different mechanical and corrosion properties. The steels studied in this thesis, SAF 2507, is a duplex stainless steel (DSS). The characteristics of DSSs and their subgroup super duplex stainless steels (SDSS) as well as the role of the alloying elements and common phases observed in these steels are discussed in the following sections.

2.2.1 Duplex Stainless Steels

DSSs have a banded dual phase structure, which consists of approximately equal amounts of austenite and ferrite, see Fig. 9. Both phases are stainless, and thus have more that 13wt.% Cr. The austenite phase increases the ductility and provides a uniform corrosion resistance, whereas the ferrite phase supplies the material with high strength and corrosion resistance. The development of duplex stainless steels is based on the demand from the chemical industry for high-strength steels with a good corrosion resistance beyond the performance of austenitic steels and the discovery of Bain and Griffith of the duplex structure that the Fe-Cr-Ni system exhibits [38, 39]. Besides the superior performance of DSSs the content of the expensive alloying element nickel is lower, which makes DSS also an economic competitor of austenitic steels.

DSS typically solidify as δ-ferrite and the austenite phase develops during the cooling [36, 40], see the phase digram in Fig. 8. The ratio between austenite and ferrite is highly dependent on the heat treatment and the subsequent cooling. During the phase transformation, also a redistribution of alloying elements occurs. In comparison to austenitic steels, DSS are not applicable for temperatures above 250°C due to the thermal instability of the ferrite phase. The thermal spinodal decomposition of ferrite into a chromium-rich and an iron-rich ferrite is commonly referred to as 475°C embrittlement [41], which causes a reduced toughness of the steel. Also hot working, typically in the range of 1000-1200°C, and welding of DSSs leads to unwanted changes in the microstructure as it exposes the steels to the δ+γ-phase region. Further, the precipitation of unwanted secondary phases, e.g. σ-phase, can occur. Hence, DSSs are often solution annealed at 1050-1100°C and quenched [42].

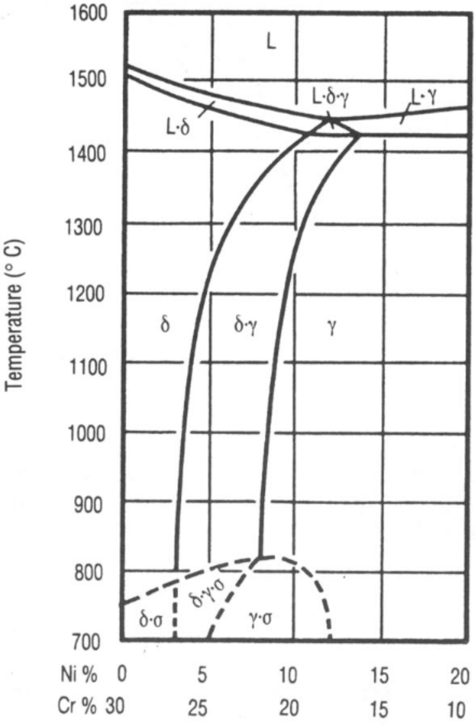

Figure 8: Pseudo-binary phase digram for the Fe-Cr-Ni system with a constant iron content of 70 wt.%, taken from [40].

2.2.1.1 Super Duplex Stainless Steels

A subgroup of DSSs are Super DSSs, where the 'super' refers to their even higher strength and corrosion resistance than DSSs. These characteristic properties are obtained by the large amount of alloying elements, making the SDSSs a complex system to study. For a DSS to qualify as a SDSS it needs to possess a Pitting Resistance Equivalent Number (PREN) of 40 and above. The PREN in weight percent is defined as:

$$\text{PREN} = \%\text{Cr} + 3.3\text{x } \%\text{Mo} + 16\text{x } \%\text{N} \tag{8}$$

Due to their high corrosion resistance SDSSs are suitable for applications in aggressive environments [41] such as seawater handling and process systems, heat exchangers in geothermal exploitation units, and chloride containing bleaching environments among others.

Table 3: Nominal composition in weightpercent of the SAF 2507. Chemical composition is shown as maximum unless indicate as a range.

element	Fe	Cr	Ni	Mo	N	Mn	Si	P	C	S	others
wt%	bas.	25	7	4	0.27	$\leq$1.2	$\leq$0.8	$\leq$0.035	$\leq$0.03	$\leq$0.015	0.3

The SDSS studied in this thesis is SAF 2507. Its nominal composition is given in Tab. 3. The minimum PREN value for Sandvik SAF 2507 is 42.5 for both the ferrite phase and the austenite phase. Typically the phase with the lowest PREN value will be limiting for the actual pitting corrosion resistance but in SAF 2507 the PREN value is equal in both phases. Images showing the dual phase structure of SAF 2507 are given in Fig. 9.

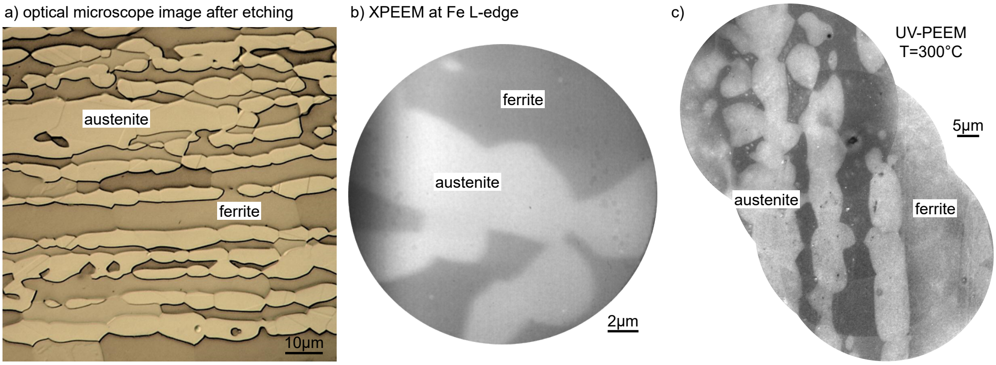

Figure 9: a)Optical microscope image taken after treating the surface with Murakamis etchant, revealing the typical banded two phase structure of SDSS SAF 2507. b) XPEEM for SAF 2507 at Fe L-edge with hν=706.65 eV showing the clear two phase structure. c) UV-PEEM images joined to show a larger area of the surface of SAF 2507 after heating to 300°C.

2.2.1.2 Role of Alloying Elements

As super duplex stainless steels belong to the group of highly-alloyed steels the influence from the different alloying elements on the steels performance is of major importance. The alloying elements can generally be grouped by their ability to stabilize a certain phase in the steel. Tab. 4 shows examples of commonly used stabilizers for austenite and ferrite [43]. All the alloying elements listed in Tab. 4 further suppress the martensite formation. [36]

Table 4: Commonly used alloying elements to stabilize either the ferritic or austenitic phase in stainless steels.

austenitisers	Ni, C, N, Co, Mn, Cu
ferritisers	Cr, Si, Mo, V, Al, Ti, W

Chromium is the main alloying element in stainless steels and it is used to improve the steels' strength, stabilize the ferrite phase, and to obtain the corrosion resistance of the alloy as it forms a passive oxide film on the surface. In duplex grades the chromium content typically ranges from 20-30%. The optimal limit of the chromium content is heavily influenced by other alloying elements such as carbon and nitrogen, which lead to the formation of chromium carbides (M_23C_6) and nitrides (Cr_2N). These have a negative impact on the toughness, ductility, and corrosion resistance of the steel. Another ferritiser is molybdenum, which also increases the stability of the passive oxide layer [44]. The combination of a high Mo content with a high Cr content leads, however, to the nucleation of intermetallic compounds [45].

The austenite phase in DSSs is stabilized by nickel, as shown in Fig. 10 a). Excessive amounts of nickel result in an austenite fraction above 50% and will increase the partitioning of chromium and molybdenum in the ferrite phase [43]. The austenite phase can also be stabilized by nitrogen, which additionally increases the strength of the DSS by acting as an interstitial solid solution element [46]. Further, N enhances the high temperature stability of the duplex structure and it improves the localized corrosion resistance. The N content in SDSSs has been increased until the solution limit.

To roughly estimate the impact of all the ferrite and austenite forming elements combined, the so-called Schaeffler diagram can be used, see Fig. 10 a). It uses equivalents for the chromium and nickel [36] content according to:

$$\%\mathrm{Cr_{equ}} = \%\mathrm{Cr} + \%\mathrm{Si} + 1.5\%\mathrm{Mo} + 5\%\mathrm{V} + 5.5\%\mathrm{Al} + 1.5\%\mathrm{Ti} + 0.7\%\mathrm{W} \tag{9}$$

$$\%\mathrm{Ni_{equ}} = \%\mathrm{Ni} + \%\mathrm{Co} + 0.5\%\mathrm{Mn} + 0.3\%\mathrm{Cu} + 25\%\mathrm{N} + 30\%\mathrm{C}. \tag{10}$$

2.2.1.3 Phases and Their Transformation

Phase transformation in stainless steels can also de induced by heat treatment. This is particularly important when considering high temperature applications, hot working, and the welding of steels as the superior corrosion and strength properties can be affected by the precipitation of different phases. The heating and cooling rates can determine if and which phases form. To predict the phase changes, a Schaeffler diagram, see Fig. 10 a), can be used. To obtain a better knowledge on the phase changes in a certain composition thermodynamic models are used to calculate the fraction of the equilibrium phases as a function of the heating temperature. A theoretical phase diagram for SAF 2507 was calculated using Thermo-Calc [47], as shown in Fig. 10 b).

Besides the two wanted phases, austenite and ferrite, other secondary phases are observed in SAF 2507. The most well-known phase is the σ-phase as it forms in many DSSs [41]. The σ-phase is a Fe-Cr-Mo rich phase that has a tetragonal phase structure in which the lattice sites can be filled with the different alloying elements [37]. It is formed by ferrite decomposing into austenite and σ-phase in a eutectoid transformation in a temperature range from 600-1000°C [48]. The precipitates of the σ-phase typically occur at the phase boundaries between austenite and ferrite [41, 49]. Already small amounts of the σ-phase have a negative impact on the steels toughness and corrosion resistance [50, 51].

A commonly observed precipitate in DSSs is chromium nitride. Chromium nitrides have the compositions CrN or Cr_2N and typically form in temperatures ranging from 700-900°C [37]. The precipitates typically forms on austenite/ferrite or ferrite/ferrite boundaries [52]. Heating to high temperatures

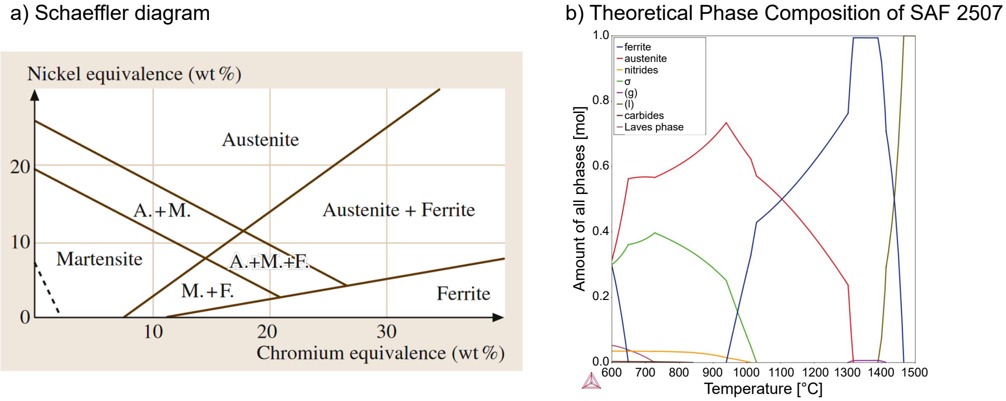

Figure 10: a) Schaeffler diagram showing the phase of steels as a function of the chromium and nickel equivalent elements. Image taken from [36] b) Thermodynamic calculations of equilibrium phase fraction for SAF2507 as function of temperature. Courtesy of Eleonora Bettini.

followed by rapid cooling, as occurring during welding, appears to leads to the formation of non-equilibrium nitrides [41].

In SDSS SAF 2507 only very small amount of carbides are expected, see Fig. 10 b). This is due to the quite low carbon content that DSSs and SDSSs exhibit. Another phase that is found in SAF 2507 is the intermetallic Laves phase.

The phases described here are only a small portion of the possible phases that occur in stainless steels. A summary of the different phases and precipitates found in stainless steels containing their lattice parameter can be found here [37]. An illustration of the magnitude of phases that are present on the the surface of a duplex stainless steel after heat treatment is shown in Fig. 11.

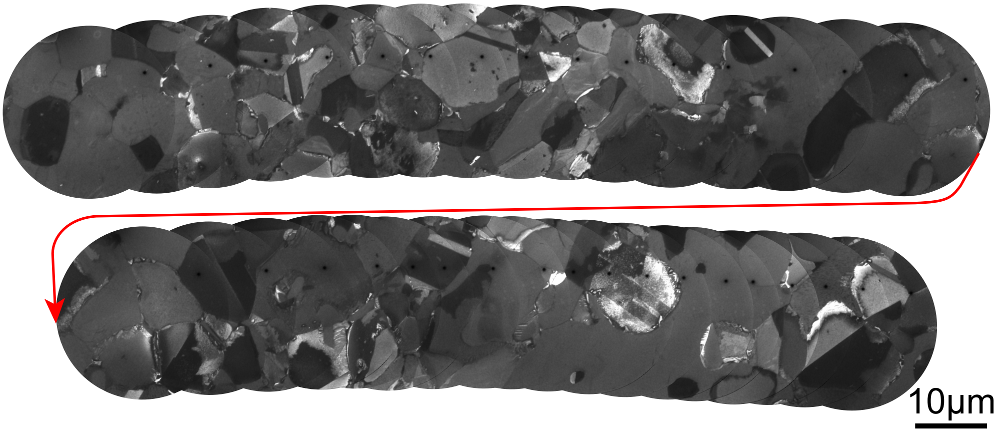

Figure 11: LEEM overview compilation of the surface of SAF 2507 after being heated to 1200°C showing the multitude of phases and grains forming.

3 Instrumentation and Experimental Methods

This chapter gives a short description of the different surface science techniques used in this thesis. Due to the fact that the experimental methods are based on the use of X-rays and electrons, section 3.1 begins with an introduction to electron emitters as well as to X-rays and their generation in a synchrotron. Since generated waves either scatter or absorb when interacting with matter, the two following sections, sections 3.2 and 3.3, describe these interactions and the different experimental methods derived from them: reflection, diffraction, and spectroscopy. The last section, section 3.4, focuses on how the different methods can be used for imaging the samples' surface.

The multitude of experimental techniques is necessary since the application of a single experimental technique only describes part of the material's properties. Therefore, the material analysis relies on a multi-technique approach, where the different techniques provide complementary information.

3.1 Electron and X-rays Sources

In surface science many experimental techniques rely on electrons and photons as probes. Depending on the energy, the probes have different characteristics and different properties of the sample can be studied. Photons in the energy range of 100 eV-100 keV, X-rays, can just as all electromagnetic radiation either be described as waves or as particles. The photon's energy is given by

$$E = \frac{hc}{\lambda}, \tag{11}$$

where h is Planck's constant, c is the speed of light in vacuum, and λ is its wavelength. X-rays can be used to probe core-level electrons, which allows the determination of the elements present in the sample and the chemical state it is in. X-rays can also be used for different kinds of scattering techniques, like X-ray reflectivity (XRR) as used in this thesis.

Electrons can create similar excitations in materials as photons but there are major differences in how the excitations are created as electrons are particles with mass, charge, momentum, and spin. Electrons with low kinetic energies, 0-500 eV, are used in mirror electron microscopy (MEM), low-energy electron microscopy (LEEM), and low-energy electron diffraction (LEED) whereas sacnning electron microscopy (SEM) uses high energy electrons in the keV range. The low energy electrons are used because of their high surface sensitivity.

3.1.1 Electron Sources

Collimated electron beams with controllable energy are generated in so called electrons guns. They are be based on different types of electron emitters such as thermionic emission, field emission, photoemission, as well as combinations of them. A typical material for a thermionic emitter is LaB_6, commonly used in the form of a (100) oriented single crystal rod with a conical tip. The low work function of the (100) surface, 2.70 eV, allows operation already at 1800 K [53].

The electrons emitted are focused by a Wehnelt cylinder and accelerated to a well-defined energy by the voltage of an anode plate or another positively biased component. The Wehnelt is negatively biased with respect to the electron emitter allowing electron emission only from a small area at its tip. By adjusting the Wehnelts bias the electron sources' size and current is set. The energy resolution of the electron beam is mainly determined by the spread of energies in the electrons that leave the cathode.

3.1.2 X-ray Sources

When W. C. Röntgen studied the phenomena occurring when an electric current passed through a gas of extremely low pressure in 1895, he discovered an unknown type of radiation, X-rays. Röntgen's work was followed by W. H. Bragg and W. L. Bragg's discovery that crystalline samples produced a characteristic diffraction pattern when irradiated by X-rays, and later M. von Laue described X-rays as waves in 1912. All four scientists received a Nobel prize in physics for their work. These discoveries have enabled scientists to probe and interpret the crystalline structure of materials at the atomic level.

Conventional X-rays are produced by bombarding a metal target with high-energy electrons as shown in Fig. 12 a). The X-rays generated in this way consists of a broad spectrum, bremsstrahlung, with additional sharp lines from electronic transitions, see Fig. 12 b). These transitions occur when the bombarding electron has sufficient energy to eject an inner shell electron from the metal target, creating an electron vacancy.

Here, an electron from a higher level fills the vacancy and a photon is emitted with a sharply defined energy equal to the energy difference between the vacancy level and the initial energy level of the electron. These emission lines are characteristic for every element. Common metal targets for X-ray lab sources are magnesium, aluminum, molybdenum, and copper. To obtain a well defined X-ray energy, monochromators are used.

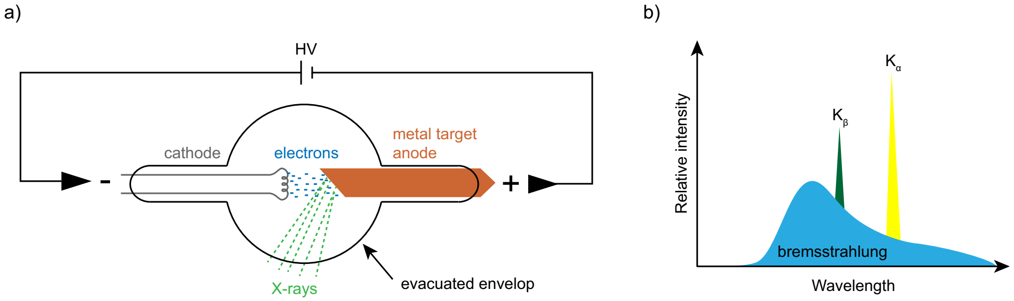

Figure 12: a) Schematic drawing of an X-ray tube and b) a typical X-ray radiation spectrum produced by an X-ray tube.

Typically, to create XUV radiation, 10-125 eV, atomic emission lamps are used, where an electric discharge is sent through an ionized gas. Typical emission lines are those of H (10.2 eV) and He (21.1 and 40.82 eV). The He lamp in particular has been a workhorse for lab-based ultraviolet photoelectron spectroscopy (UV-PES) and photoelectron emission microscopy (PEEM) experiments.

3.1.3 Synchrotron Radiation

Classical electrodynamics describes how charged particles that are accelerated emit energy in form of electromagnetic waves. The total power radiated of non-relativistic particles is very small and scales only with the square of the change of the charged particles momentum, as described by Larmor [54].

In synchrotrons, relativistic particles are used. Thus, they need to be described by relativistic electrodynamics. This is done by applying a Lorentz transformation to time and momentum. By further considering, that the charged particles are accelerated on a circular path, as in a bending magnet, the following expression can be derived, as done by Liénard [55], where c is the speed of light in vacuum, ε_0 the permittivity of free space and R the bending radius of the orbit the accelerated particle

$$P_s = \frac{e^2 c}{6\pi\varepsilon_0} \frac{1}{(m_0 c^2)^4} \frac{E^4}{R^2} \tag{12}$$

In Eq. 12 the radiated power, P_s, for particles with the elementary charge, e is proportional to the fourth power of the particle energy, E, and inversely proportional to the fourth power of the rest mass, m_0. Thus, mostly particles with a low rest mass, usually electrons, at relativistic velocities are used to produce synchrotron radiation.

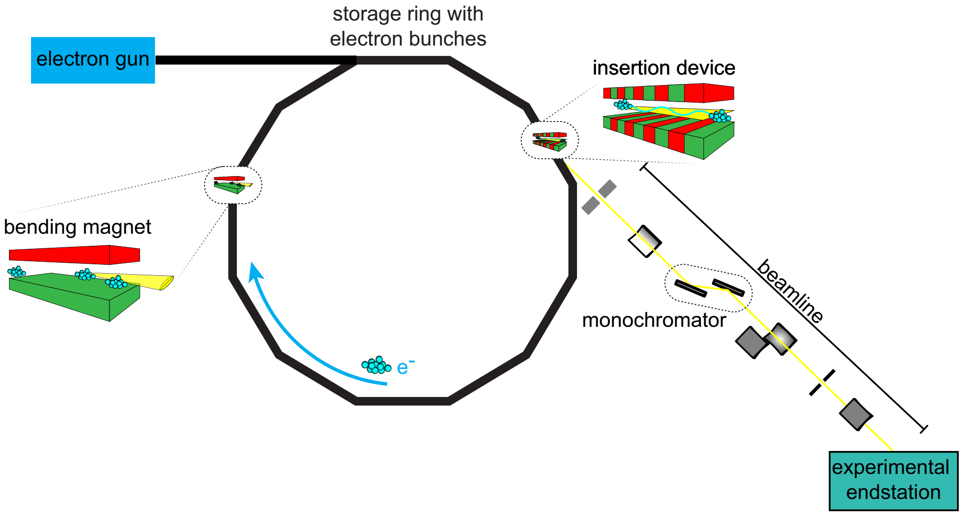

Figure 13: Schematic layout of a synchrotron radiation facility. Electrons are generated in the electron gun and are accelerated to a speed close to the speed of light. X-rays are generated in bending magnets or insertion devices, e.g. a undulator. The X-ray beam is focused and monochromatized until it reaches the experimental endstation, where the instruments for the different techniques are placed.

By combining several short bending magnets with alternating polarity into an undulator or wiggler, the electrons are forced onto an sinusoidal path, which allows for the production of a more intense and highly collimated beam. Today, dedicated storage rings are used instead of synchrotrons because they operate at constant energy and thus, provide a more stable beam.

The main advantages of using synchrotron radiation sources are high intensity, good tunability with respect to the wavelength, low divergence and a small beam size. A more complete description can be found here [56,57]. The general layout of a synchrotron radiation facility is shown in Fig. 13, where the synchrotron radiation produced by a storage ring is delivered through a beamline to the experimental endstation.

3.1.4 Experimental Considerations

By using the interaction of electrons and X-rays with matter to study materials, certain restrictions with respect to the experimental conditions are given. Classically ultrahigh vacuum (UHV) conditions are used in surface science to keep the samples surfaces atomically clean during the experiment. However, also if industrial 'dirty' samples that do not require clean surfaces are studied, restrictions occur.

When working with electrons, especially with low energy electrons, the strong interaction between matter and electrons often requires high vacuum conditions to limit gas phase scattering. The average distance that a particle, e.g. an electron, can travel in gas phase between collisions can be derived from a simple hard-sphere collision model [58], where the mean free path, λ, of the particle is approximated by

$$\lambda[m] = \frac{kT}{1.414P\sigma}, \tag{13}$$

where P is the pressure $[Nm^{-2}]$, k is the Boltzmann constant, T is the temperature [K], and σ is the collision cross section $[m^2]$. This means that high vacuum conditions, 10^{-3}- 10^{-7} mbar, are necessary to keep the electrons path collision free, whereas maintaining atomic clean surfaces require strict UHV conditions.

UHV is not a necessary requirement when working with X-rays as their interaction with matter is much weaker compared to electrons with the same energy. To use X-rays for surface sensitive studies, small angles of incidence can be utilized [59]. This is used in different grazing incident techniques such as XRR and GISAX (grazing-incidence small-angle X-ray scattering).

Restrictions when using X-rays are more concerned with the ability to focus the beam as with increasing energy the absorption cross-section increases, hence lenses and mirrors used in optics with visible light are not very effective and special optics are required. These are not within the scope of this thesis and a review on X-ray optics can be found here [60].

3.2 Scattering Techniques

X-ray scattering techniques are widely used to identify and quantify phase, determine the crystal and surface structure and their orientation and texture as well as studying strain through changes in lattice parameters, and measure the sizes of grains, pores, particles, and thickness of layers. The main differences between the scattering techniques are which probe is used, e.g. photons, electrons or neutrons, if the scattering observed is elastic or inelastic, and which angles are used.

The two scattering techniques used in this thesis are XRR and LEED. XRR uses X-rays to study the structure of surfaces, interfaces, and thin films. With XRR, information on the roughness and the thickness of a sample's surface and interfaces can be derived in a non-destructive manner down to a few hundreds of a nm. LEED is used for surface structure determination by the diffraction of low energy electrons and observing the angular distributions of the scattered electrons.

3.2.1 X-ray Reflectivity

In XRR, the sample is irradiated with a monochromatic X-ray beam with a wavelength, λ, at an incident angle of $\alpha_i < 5°$. These X-rays are then partially reflected at the surface or an interface at an angle of $\alpha_f = \alpha_i$. The reflected intensity is recorded as a function of the incident angle α_i. Typically, in XRR as in other techniques using grazing incidence X-rays as probe, the incident angle is reported as the angle between the X-ray beam and the surface in contrast to conventional optics, where the incident angle refers to the angle between the beam and the surface normal.

To describe the reflectivity of a material the complex refractive index n is used. It is defined as

$$n = 1 - \delta + i\beta, \text{ with } \delta = \frac{\lambda^2}{2\pi} r_0 \rho \text{ and } \beta = \frac{\lambda}{4\pi}\mu, \tag{14}$$

where δ is the dispersion coefficient and β is related to the absorption coefficient, μ. Both, δ and β, represent material specific constants. δ itself is dependent on the wavelength of the incoming beam, λ, the Thomson scattering length, r_0, and the electron density ρ. Typical values for δ are in the range of 10^{-6} for solid materials and 10^{-8} for air, which is about two orders of magnitude larger than usual values for β.

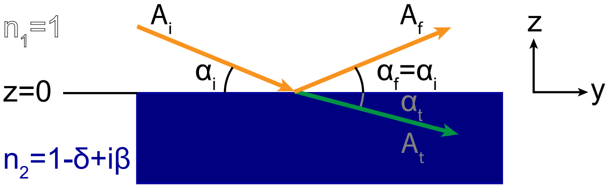

Figure 14: Sketch illustrating X-ray reflection and refraction at an interface where the refractive index n_1 is unity and n_2 is less than unity. The incoming X-ray beam A_i is partially reflected at the interface at an angle of reflection, $\alpha_f = \alpha_i$. Another part of the beam is refracted and transmitted as A_t at an angle of α_t. Total reflection only occurs at angles smaller than the critical angle, α_c. The remaining part of the X-ray beam is absorbed.

If, as shown in Fig. 14, an X-ray beam is reflected at the interface between vacuum and a medium with a refractive index smaller than unity, total external reflection occurs at incoming angles, α_i, smaller than the critical angle, α_c. The critical angle is given by Snell's law $\cos\alpha_c = n\cos\alpha_t$. As β is very small the refractive index can be approximated as $n = (1-\delta)$. By using a Taylor series expansion for small angles the critical angle can be approximated as

$$\alpha_c = \sqrt{2\delta}. \tag{15}$$

Since air has a low density this approximately hold true for experiments in air, too. The critical angle α_c is usually below 1° for vacuum(air)/solid interfaces. At angles higher than the critical angle, α_c, the specularly reflected intensity decays rapidly with a $\frac{1}{q^4}$ dependency, where q is the scattering vector.

Now considering reflection from a multilayer system, the first reflection of the impinging X-ray beam originates at the interface between vacuum and the sample's surface. The part of the X-ray beam that is transmitted is reflected and refracted at the next interface, whereof the transmitted beam undergoes reflection and refraction again. The parts of the beam that are reflected at the interface either constructively or destructively interfere with each according to the Bragg condition, $2d\sin\theta = n\lambda$. This interference creates oscillations in intensity, so called Kiessig fringes, which are superimposed onto the decaying curve, as shown in Fig. 15. The periodicity of these oscillations can be used to determine the thickness of the different layers in the sample according to

$$D = \frac{2\pi}{\Delta q_z}. \tag{16}$$

A more detailed descriptions of XRR theory and models for data analysis can be found in the literature, e.g. [59, 61–63].

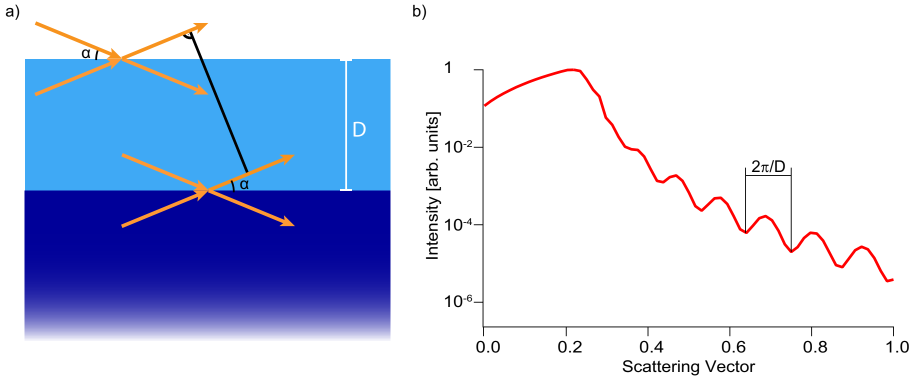

Figure 15: a) X-ray reflection and refraction in a multilayer system, here showing the surface and the first interface. b) Simulated reflectivity curve showing typical Kiessig fringes. The distance between the fringes can be used for thickness determination.

3.2.2 Low Energy Electron Diffraction

To study the materials introduced in chapter 2 on an atomic scale, a probe with the same length scale, 0.3 to 3 Å, is necessary. As electrons can be also treated as waves they can be used to investigate periodic arrangements of atoms. Electrons with kinetic energies between 20 and 500 eV have a de Broglie wavelength in the range of that length scale. The electron's de Broglie wavelength, λ, can be calculated by

$$\lambda(\text{Å}) = \frac{h}{\sqrt{2m_e \cdot E}} = \sqrt{\frac{150.6}{E(eV)}}, \tag{17}$$

where h is the Planck constant, m_e is the mass of an electron, and E is the electron's kinetic energy. It follows that electrons with a kinetic energy of 100 eV have a de Broglie wavelength of 1.2 Å.

The theoretical foundation of LEED measurements was in fact laid by Louis de Broglie's work on the wave-particle duality. This led to the possibility to probe the periodic structure of crystals. First experiments were made by Clinton Davisson and Lester Germer [64] and later Clinton Davisson and George Thompson were awarded the Nobel prize "for their experimental discovery of the diffraction of electrons by crystals" [65]. This started the extensive use of electron diffraction studies in solid state physics.

LEED is one of the most commonly used methods today to determine the surface structure because of the short inelastic mean free path (IMFP), see Fig 16, of low energy electrons. Hence, these electrons only probe the utmost few atomic layers.

In LEED, a monochromatic electron beam which typically has an energy range, E_p, from 20 to 500 eV is generated in an electron gun. The electrons emitted by the filament are collimated by the Wehnelt cylinder and afterwards pass electrostatic lenses which are used to accelerate and focus the electron beam. The focused electron beam is impinging on the sample at normal incidence. The electrons undergo diffraction and are backscattered. The elastically backscattered electrons undergo constructive interference and create intensity spots on a spherical fluorescent screen.

For electrons to be detected on the fluorescent screen they have to pass the grids, shown as G1-G4 in Fig. 17 a). Grids G1 and G4 are usually grounded to create a field-free region. The two inner grids, G2 and G3, are used as suppressor grids to cut-off the inelastic scattered electrons by holding them at a negative potential, $V=-E_p+\Delta V$, where ΔV is typically in the range of 0-10 V. Since only high energy electrons cause light emission from the fluorescent screen, it is biased at a high positive voltage of a few keV. A schematic drawing of the LEED setup is shown in Fig. 17 a).

Fig. 17 b) illustrates the diffraction process in reciprocal space in a LEED experiment. Here, electrons are impinging on the sample's surface at normal incidence with a wave vector k. All the different possible scattered waves k' construct the Ewald sphere and its radius is equal to the length of the incoming wavevector k,

$$|k| = \frac{2\pi}{\lambda}. \tag{18}$$

Since the incidence angle is fixed normal to the surface $k_{||}$=0 and the change in direction due to scattering will be $\Delta k_{||} = k'_{||}$. Constructive interference occurs

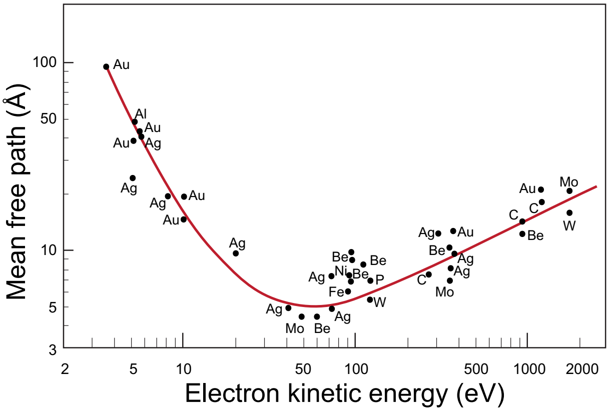

Figure 16: Universal curve for the electron mean free path as function of the kinetic energy. It explains why electron based methods are very surface sensitive in the energy range of 10-2000 eV. Adapted from [66].

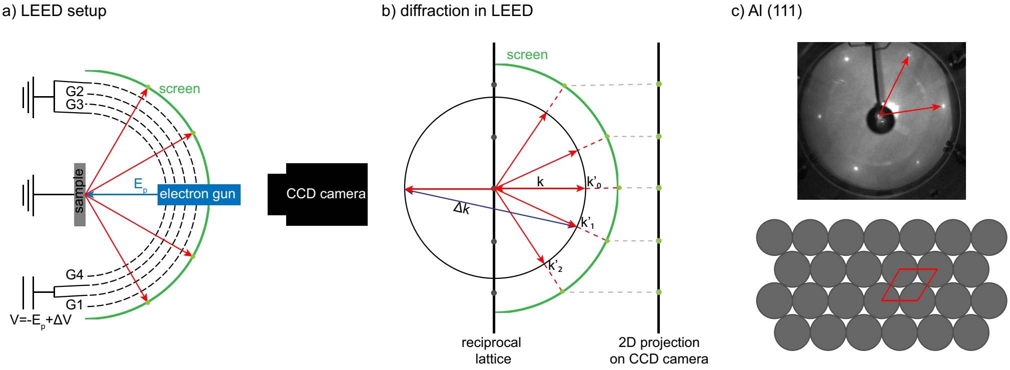
a) LEED setup
G2
G3
screen
sample
E_p
electron gun
CCD camera
G4
G1
V=-E_p+ΔV
b) diffraction in LEED
screen
k
k'_0
Δk
k'_1
k'_2
reciprocal lattice
2D projection on CCD camera
c) Al (111)

Figure 17: a) A schematic drawing of a four-grid LEED setup. A monochromatic electron beam with an energy E_p is generated in the electron gun. The electrons impinging on the sample scatter and the elastically scattered electrons produce an intensity spot on the fluorescent screen by interfering constructively. b) Schematic representation of the scattering process in reciprocal space. c) Experimental LEED pattern of Al (111) and model of an Al (111) surface.

in directions where the Laue condition is fulfilled meaning that the scattered wave vector is a reciprocal lattice vector.

The scattering condition in LEED can only be varied by changing the electron energy, where a higher energy of incoming electrons results in a smaller radius of the Ewald sphere and reflections being closer to the specular (0,0) reflection. An example of experimental LEED image and the corresponding surface model for Al (111) are shown in Fig. 17 c). A more detailed description of the method can be found here [67].

3.3 Spectroscopy

The term spectrum was coined by Sir Isaac Newton when describing how visible light is dispersed through a prism. Later the meaning of the term was expanded to cover the whole range of electromagnetic radiation. Today the term spectroscopy refers to measurements of a response to a certain varying stimulus, e.g. photons and electrons.

This section introduces two spectroscopic techniques based on X-rays, namely X-ray Photoelectron Spectroscopy (XPS) and its application in ambient pressures as well as X-ray Absorption Spectroscopy (XAS). The phenomena introduced here are also used to create images in X-ray Photoelectron Emission Microscopy (XPEEM) as described in the microscopy section 3.4.

3.3.1 X-ray Photoelectron Spectroscopy

XPS is one of the most commonly used techniques to study the chemical composition of surfaces. It is based on the concept of the photoelectric effect, which was discovered by H. Hertz in 1887 [68]. The photoelectric effect is the name for the process of removing an electron from the surface of a solid by irradiating it with photons. A. Einstein [69] explained this phenomenon in 1905 and later, in 1921, he was awarded the Nobel Price in physics "for his services to Theoretical Physics, and especially for his discovery of the law of the photoelectric effect" [70].

K. Siegbahn discovered that the core-level binding energy of an electron in an atom is influenced by the chemical surroundings of the photoemitting atom and he coined the term Electron Spectroscopy for Chemical Analysis (ESCA) [71]. In 1981 K. Siegbahn received the Nobel Prize in physics "for his contribution to the development of high-resolution electron spectroscopy" [72]. Since the chemical surrounding of the atom can be deduced from an X-ray photoelectron (XP) spectrum, XPS measurements give information on the electronic and chemical state of the atom.

Typical XPS measurements use X-rays in the energy range from 10 to 1000 eV. Even though X-rays at these energies can penetrate the sample up to several μm, the photoelectrons emitted originate only from the topmost layers of the sample. This is due to the short IMFP of electrons in solid materials as discussed in section 3.2.2 for LEED and shown in Fig. 16. This means that e.g. photoelectrons emitted with a kinetic energy of 100 eV from solid aluminum originate from the topmost 5 Å of the sample [73].

3.3.1.1 Three-step model

The processes taking place during an XP experiment are shown in Fig. 18 and can be explained in a classic way by the simplified three step model which was developed by Berglund and Spicer [74, 75]. In the first step a photon with an energy of $h\nu$ impinges on the surface and excites a system with the initial energy E_i. After the excitation the electron is transported to the surface. Finally, the electron has to overcome the vacuum barrier and becomes a free electron, which has a kinetic energy of E_{kin} and and the system remains with a final state energy of E_f. The process is illustrated in Fig. 18.

Invoking the law of conservation of energy, the following equations can be deduced

$$E_i + h\nu = E_f + E_{kin} \tag{19}$$

$$E_{kin} = h\nu - E_B - \Phi \tag{20}$$

By considering that the difference between the initial energy E_i and the final energy E_f is equal to the ionization potential E_I, which itself is equal to the sum of binding energy E_B and work function Φ of the sample, we can rearrange Eq. 19 to arrive at 20. From that it is clear that by detecting the kinetic energy, E_{kin}, it is possible to extract the binding energy, E_B, if a monochromatic light source with a known photon energy, $h\nu$, is used and the sample is kept at the same potential as the analyzer, the sample Fermi level, E_F. In an XP experiment, the actual work function that is observed corresponds to the analyzers work function.

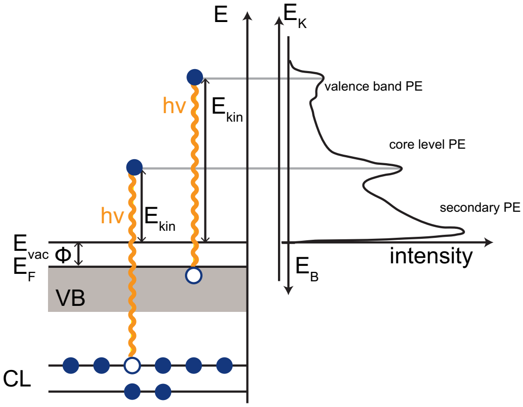

Figure 18: Energy diagram illustrating the principle of the valence and core-level photoemission process in a classical description. A photon with an energy of $h\nu$ impinges the surface and is absorbed by a core-level electron. After the excitation the electron is transported to the surface and overcomes the vacuum barrier E_{vac} and becomes a free electron, which has a kinetic energy of E_{kin}.

Even though the three-step model makes the photoemission process more comprehensible, it is only an approximation since it violates the Heisenberg uncertainty principle by assuming that the excitation occurs at a point of time before the electron propagates to the surface and transmits into the vacuum. Another part that is not covered by the three-step model is the interpretation of the band structure.

A more accurate picture of the photoemission process is given in the one step model. In that model one considers the initial state to be a Bloch state and for the final state a time inverse LEED wave function is used to describe outgoing photoelectron. A more rigorous treatment of the theoretical background on photoionization can be found e.g. in Ref. [76–78].

3.3.1.2 Data Analysis

XP spectra are created by plotting the detected intensity of photoelectrons as a function of the kinetic energy E_{kin} or binding energy E_B. Typically, the peaks in the spectrum are labeled with the element symbol and the emitting core-level. In the case of the spectrum shown in Fig 19 b), the core-level peaks for aluminum are observed. The 2 following Al stands for the principle quantum number, $n = 1, 2, 3...$ or $n = K, L, M, ...$, of the shell of the atom and the p is the orbital quantum number, ℓ, designating the subshell. The orbital quantum number quantifies the orbital angular momentum and it takes values of $\ell = n - 1$ but is typically referred to as $s, p, d, ...$, which originates from an outdated system describing the spectral lines as "sharp", "principal", and "diffuse" [79].

In high-resolution XP spectra closely separated peaks can be observed for core-levels with $\ell > 0$, as in the Al 2p spectrum in Fig 19. The reason for the close spaced doublet is the spin-orbit coupling in the final state. In the initial state aluminum has a completely filled inner core electronic configuration. After the emission of the photoelectron a single unpaired electron is left in the emitting core-level. If this unpaired electron resides in an orbital that has a non-zero orbital angular momentum, coupling between the electrons spin, $s = \pm\frac{1}{2}$, and the orbital angular momentum, ℓ, occurs. This coupling is commonly describes with the LS-coupling approximation (also referred to as Russell–Saunders coupling [80]) or the j-j coupling approximation.

In LS-coupling, the resulting total angular momentum of the unpaired electron is described by the quantum number, j. In the case of Al 2p the different values for total angular momentum are $j = \ell \pm \frac{1}{2}$. Resulting in $j = 1 + \frac{1}{2} = \frac{3}{2}$, when the two angular momenta are aligned, and $j = 1 - \frac{1}{2} = \frac{1}{2}$, when they are opposed. Since the configuration in which the spin and orbital momenta are opposing each other is energetically favored, the peak with the lower j-value is observed at higher binding energies.The intensity ratio between the two energy levels is given by their degeneracy. The number of possibilities for equal energy states ranges from $-J$ to J, giving $2J+1$ values of M_J, where $M_J\hbar$ is the z component of the total angular momentum J. With the Al 2p example, this yields in a ratio of 1:2 between the Al $2p_{1/2}$ to Al $2p_{3/2}$.

Besides the spin-orbit splitting, small variations in binding energy, known as chemical shifts, can be used to deduce the chemical state of the core-level photoemitting atom and it's chemical environment. Chemical shifts are related to the potential that the emitting atom is exposed to. Therefore, chemical shifts to higher binding energies are either caused by a increased positive formal charge of the atom or the chemical environment increasing the Coulombic attraction. The relation between core-level, kinetic energy and shift in the XP spectrum is illustrated in Fig. 18. The number of components in a core-level XP spectrum is corresponding to the number of chemically different atoms. Hence, shifted peaks can be observed for different compounds. The energy calibration in XPS is often done towards the Fermi edge but also by using well-known lines such as Au 4f for energy referencing.

Often the shifts between different chemical species are less than 1 eV, hence they are not clearly separated. Therefore, it is sometimes necessary to deconvolute the spectra for interpretation. The detected full width at half maximum (FWHM), ΔE, of a photoemission peak can be described as a convolution of the natural linewidth of the electron hole, ΔE_n, the width of the photon source, ΔE_p, and the resolution of the analyzer, ΔE_a:

$$\Delta E = \sqrt{\Delta E_n^2 + \Delta E_p^2 + \Delta E_a^2}. \tag{21}$$

Eq. 21 assumes that all components have a Gaussian line shape.

The natural width, ΔE_n, is determined by the uncertainty in the lifetime, τ, of the final ion state after photoemission occurred. The lifetime broadening, in accordance to the Heisenberg uncertainty principle, is given by

$$\Delta E_n = \frac{h}{\tau} = \frac{4.1 \cdot 10^{-15}}{\tau} eV, \tag{22}$$

where h is Planck's constant in electronvolt-seconds. The natural linewidth is modeled by Lorentzian function. The components from experimental broadening have a Gaussian line shape, where especially the analyzers resolution plays an important role. To model the two broadening mechanisms, typically a Voigt function is used as it is a convolution between a Gaussian and a Lorentzian.

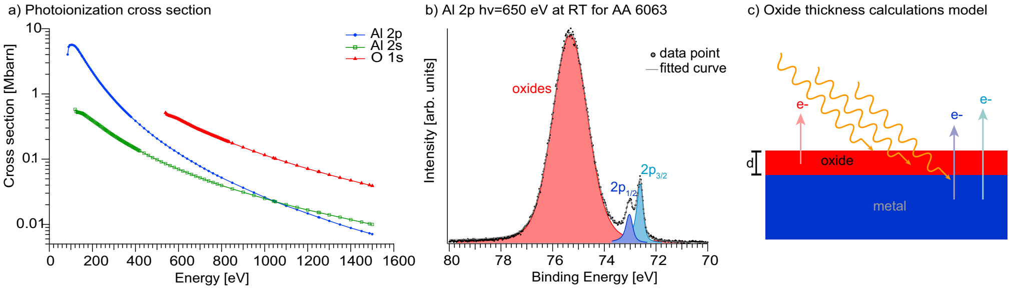

Figure 19: a) Photoionization cross section for Al 2p, Al 2s, and O 1s [81]. b) Al 2p XP spectrum from AA 6063 at RT recorded at 650 eV illustrating the spin-orbit splitting of the metallic peak into Al $2p_{1/2}$ and Al $2p_{3/2}$ as well as the shifted component for the aluminum oxides. c) Illustration showing the model used for XPS oxide thickness determination.

Due to inelastically scattered electron the peaks often exhibit an asymmetry, therefore are asymmetric Voigt functions used for curve-fitting. However, in the spectra presented in this thesis the asymmetry in the peaks mainly originate from unresolved peaks of different chemical species.

In practice, the spectra analysis is carried out by first normalizing the spectra towards photon flux and photoinonization cross section, followed by the subtraction of background and curve-fitting of the different components. In addition the spectra are calibrated to the Fermi edge or another well known and resolved core-level peak.

To quantitatively analyze XP spectra they need to be normalized. Typically for experiments conducted at synchrotron radiation facilities, the beamcurrent is used as a measure to compensate for the fluctuating photon flux. Other extrinsic factors are the transmission of the analyzer and the efficiency of the detector. Besides the external variation in the experimental parameters also intrinsic differences between different elements and their core-levels are observed for varying excitation energies. The probability of photoionization to an ion state is quantified by the photoionization cross-section, σ. Tabulated values of the photoionization [81] cross-sections allow to chose core-levels that produce high intensity in their respective spectra. To be able to quantitatively compare the spectra of different elements and core-levels the photoionization cross sections are also used for normalization. Fig. 19 a) shows the photoionization cross section for Al 2s, Al 2p, and O 1s.

XPS can also be used to determine the surface oxide thickness by extracting the integrated intensity of the core-level peaks. In the case of the Al 2p shown in Fig. 19, three asymmetric Voigt functions are fitted after subtracting a linear background. The aluminum oxide thickness, d_{XPS}, can then be calculated according to Eq. 23:

$$d_{XPS} = \lambda_{OX} \sin(\theta) \ln \left(\frac{N_{ME} \lambda_{ME} I_{OX}}{N_{OX}, \lambda_{OX} I_{ME}} + 1 \right) \tag{23}$$

in which λ is the IMFP, N is the volume density, where the ratio of the volume densities calculated from the densities is $N_{ME}/N_{OX} = 1.4$ [82], and I is the integrated peak intensity for the aluminum oxide (OX) and the metallic aluminum (ME) [83]. Further, θ is the photoelectron emission angle, which in the case shown in Fig. 19 b) was 90°, i.e. normal photoelectron emission geometry. The IMFP for specific core-levels can be calculated using the software QUASES-IMFP-TPP2M [84], which is based on the publications from Tanuma et al. [85, 86].

When using the above described method to determine the oxide thickness, it must be considered that the model is based on a homogeneous oxide layer with a uniform thickness, as shown in Fig. 19 c). Since the alloys studied in this thesis are not homogeneous, the calculated thicknesses should be understood as estimates.

3.3.1.3 Ambient Pressure X-ray Photoelectron Spectroscopy

Even though XPS is a very powerful technique for surface analysis it had one major drawback: it required high-vacuum (HV) conditions due to the short IMFP of electrons in gases, as discussed in section 3.1.4. In addition, other components of an XPS instrument requires HV conditions for operation, e.g. the detector.

For studies on industrial materials it is, however, desirable to investigate the surface properties under condition close to the real environments that the materials are exposed to. This can be achieved by applying a differential pumping scheme to reduce the pressure on the electrons path from the sample environment to the analyzer and detector.

The foundation for the development of ambient pressure XPS (APXPS) instruments was laid by the group of Kai and Hans Siegbahn at Uppsala University already in the 1970s [87–89]. Later other groups also developed further instruments [90–92] but all of them employed laboratory X-ray sources, which provide a comparatively low photon flux. Hence, the use of these instruments was limited until they were combined with the high photon flux that can be obtained at synchrotron radiation labs. The first synchrotron radiation-based APXPS was installed at the Lawrence Berkeley National Lab (LBNL) [93, 94].

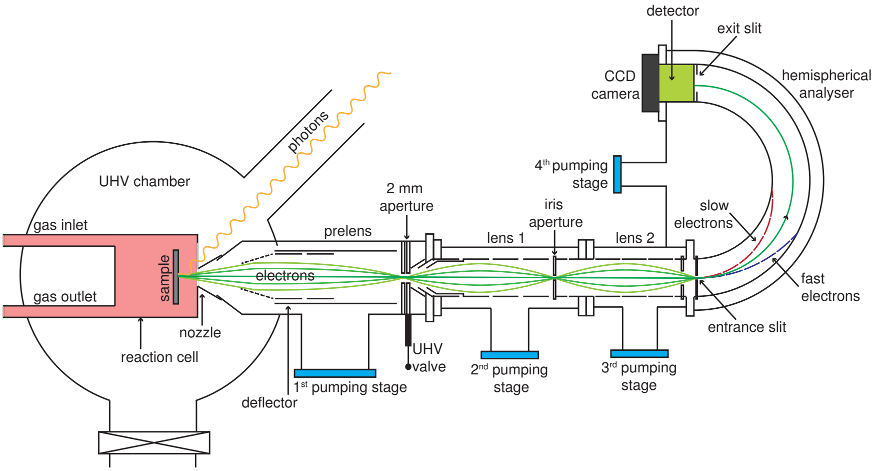
detector
exit slit
CCD camera
hemispherical analyser
photons
UHV chamber
4th pumping stage
2 mm aperture
iris aperture
slow electrons
gas inlet
prelens
lens 1
lens 2
electrons
sample
gas outlet
fast electrons
entrance slit
nozzle
UHV valve
reaction cell
2nd pumping stage
3rd pumping stage
1st pumping stage
deflector

Figure 20: A schematic drawing of the APXPS instrument at the SPECIES beamline at MAXIV laboratory using a SPECS Phoibos 150 NAP analyzer. The principle layout is based on the cell-in-cell concept. The image is based on [95].

The APXPS instrument, used in this thesis, is the one of the SPECIES beamline [96] at MAX IV laboratory, previously positioned at beamline I511 at the MAX II electron storage ring. This instrument employs the cell-in-cell/Lund approach [97], where a reaction cell is placed inside the UHV chamber, see Fig. 20. This allows both APXPS and conventional UHV-type experiments in one instrument as the reaction cell can be detached from the spectrometer. The reaction cell is equipped with an X-ray transparent window to enable the X-rays to reach the sample.

The spectrometer used in this setup is a SPECS Phoibos 150 NAP analyzer as illustrated in Fig. 20. The aperture nozzle has a diameter of 0.3 mm and is placed about 0.6 mm away from the sample to ensure a homogeneous pressure above the sample's surface [98, 99]. The photoelectrons traveling through the nozzle are collected and focused by the prelens, lens 1, and lens 2 on the following apertures enhancing the transmission. The three electrostatic lenses are also used to retard the electrons before the energy separation in the hemispherical energy analyzer occurs. The four different pumping stages reduce the pressure from several mbars in the reaction cell to UHV condition at the electron detector.

In Papers III and IV this setup was used to compare the surface development at elevated temperatures in different oxygen rich environments. These publications highlight the importance of APXPS for material science experiments as major changes in the surface oxide composition were observed. Other areas of research that frequently use APXPS include catalysis [100–102], atomic layer deposition [103, 104], and film growth [105].

3.3.2 X-ray Absorption Spectroscopy

The excitation of a system with photons can lead to the emission of electrons into the vacuum, i.e. they become photoelectrons as in XPS shown in Fig. 21 a), or electrons can be promoted into unoccupied state in the conduction band, which is the case in XAS, see Fig. 21 b). Typically XAS measurements are performed by scanning across the absorption edge of a specific element by varying the photon energy.

Since instruments often combine XPS and XAS, it is experimentally easier to detect photoelectrons rather than photons to determine how much the intensity was reduced due to absorption. This also results in more surface sensitive XAS measurements. Hence, many XAS instruments use an indirect way of obtaining the signal via the core hole decay. The core hole created by the initial excitation can either be filled through fluorescence decay or Auger decay. In Auger decay a valence electron fills the core hole but the excess energy is transferred to another electron which then has sufficient energy to escape into the vacuum, see Fig. 21 c). Since the number of core holes created by the initial X-ray absorption is proportional to the emitted electrons from the Auger decay, their signal can be used measure the absorption signal [106]. X-ray absorption (XA) spectra in Auger decay mode are generated by detecting the intensity of the Auger electrons as a function of photon energy, referred to as Auger electron yield (AEY) mode.

During fluorescence decay the core hole is filled by a valence electron transitioning into the lower energy state and releasing the excess energy as radiation, see Fig. 21 d). XAS measurements in fluorescent yield (FY) mode are less surface sensitive as the emitted photons have a longer escape depth.

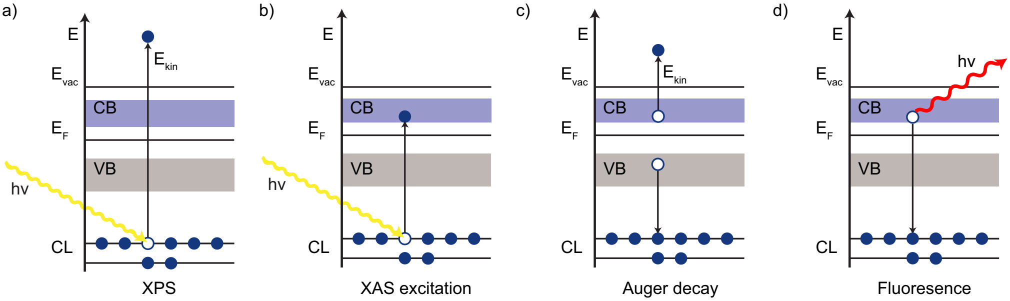

Figure 21: Energy diagrams comparing photoemission, X-ray absorption and core hole decay processes. a) In XPS a core-level electron is ejected due excitation of incoming photons. b) During X-ray absorption, a core-level electron is promoted into a higher level in the conduction band. c) Illustration of one of the decay processes that can occur after X-ray absorption, Auger decay. In Auger decay, the core hole is filled by a valence band electron and the simultaneous emission of a Auger electron carrying the excess energy. d) Core hole decay by fluorescence as the excess energy of the system is emitted by a photon.

Other modes of detection are total electron yield (TEY) and partial electron yield (PEY). In TEY mode all ejected electrons are measured including secondary electrons that are generated by inelastic scattering events. The amount of secondary electrons does not correspond to the amount of initial electron holes as the primary electrons exchange energy and momentum with other electrons in the material. Hence, a larger number of secondary electrons than core holes can be created, making it easy to detect them. Further, measurements in TEY contain more bulk sensitive information in the signal. In PEY only electrons above a certain kinetic energy are detected, which is used to cut off the intensity generated by secondary electrons.

Since these spectra are characterized by transitions to unoccupied states, they contain information about the chemical state as e.g. the oxidation state. Collecting parts of the absorption spectrum at energies lower or higher energies than the absorption edge gives Near-Edge X-ray Absorption Fine Structure (NEXAFS) and Extended X-ray Absorption Fine Structure (EXAFS). These can provide information on coordination number and interatomic distances [107, 108].

3.4 Microscopy

The term microscopy comes from the two Ancient Greek words *μικρός* and *σκοπεῖν*, which mean ”small” and ”to see”, hence microscopy aims to observe objects that cannot be seen by the naked human eye. The tools that the field of microscopy provides for resolving small things range from simple magnifying glasses to the traditional optical light microscopes to sophisticated setups that can resolve structures on the atomic scale.

The resolving power of a microscope, which refers to the distance at which two objects can still be distinguish from each other, for conventional visible light microscopes is defined by the diffraction limit. There are two commonly used criteria for the resolving power, the Abbe and the Reyleigh criterion, which vary only slightly in their description of the diffraction limit. The Abbe criterion states that the resolution is proportional to the wavelength of the incoming light and inversely proportional to the diameter of the objective's entrance aperture [109]. This means that the maximum resolution that can be achieved by visible light is about 200 nm.

The most feasible way in improving the resolution of a microscope is hence by decreasing the wavelength. Therefore, electron microscopes can achieve a resolution at the picometer scale as the electrons wavelength is determined by the De Broglie wavelength, see Eq. 17. Two major groups of electron microscopes that use this effect are SEM and transmission electron microscopes (TEM). The working mechanism of a SEM is described in section 3.4.4.

The main set of microscopy techniques that were used in this thesis belong to the group of cathode lens microscopy. A cathode lens microscope has a strong electrostatic field between the sample, which serves as cathode, and the objective lens [110]. By this arrangement the electrons originating from the sample's surface can quickly be accelerated from very low, typically 0-100 eV, to their final energy around 10-20 keV. The strength of the accelerating field is of major importance for the lateral resolution as it is inversely proportional to the resulting resolution. Other factors that impact the resolution are the sample-to-objective distance, diffraction at apertures, chromatic and spherical aberrations in the objective lens and space charge effects [111]. Depending on which imaging technique is used, a resolution of a few nm can be obtained. Aberration corrected LEEMs can achieve a lateral resolution of 2 nm [112, 113] whereas XPEEMs reach a lateral resolution of 20 nm [114, 115]. Calculations indicate that the highest achievable resolution in aberration-corrected LEEM is about 0.5 nm, and about 3.5 nm in PEEM [116].

As the sample is a part of the objective lens in cathode lens microscopy its properties also impact the the maximal resolution obtainable. The perfect sample in cathode lens microscopy would be completely flat and perfectly aligned to the normal of the optical axis. It should further be a good conductor. Any deviation from this ideal situation does not only reduce the resolution but can also cause charging of the sample or sparking from sharp objects on the surface when applying the operating voltage of typically 20 kV.

The presented work includes mainly microscopy data from measurements performed at the SPELEEM (Spectroscopic PhotoEmission and Low Energy Electron Microscope) from Elmitec GmbH [117], that was situated at the soft X-ray beamline I311 [118] and has been transferred to the new synchrotron facility MAX IV Laboratory in Lund, where it is now available at the MAXPEEM beamline. At both locations a synchrotron is used as a tunable X-ray source. A schematic describing the general layout of the SPELEEM is shown in Fig. 22.

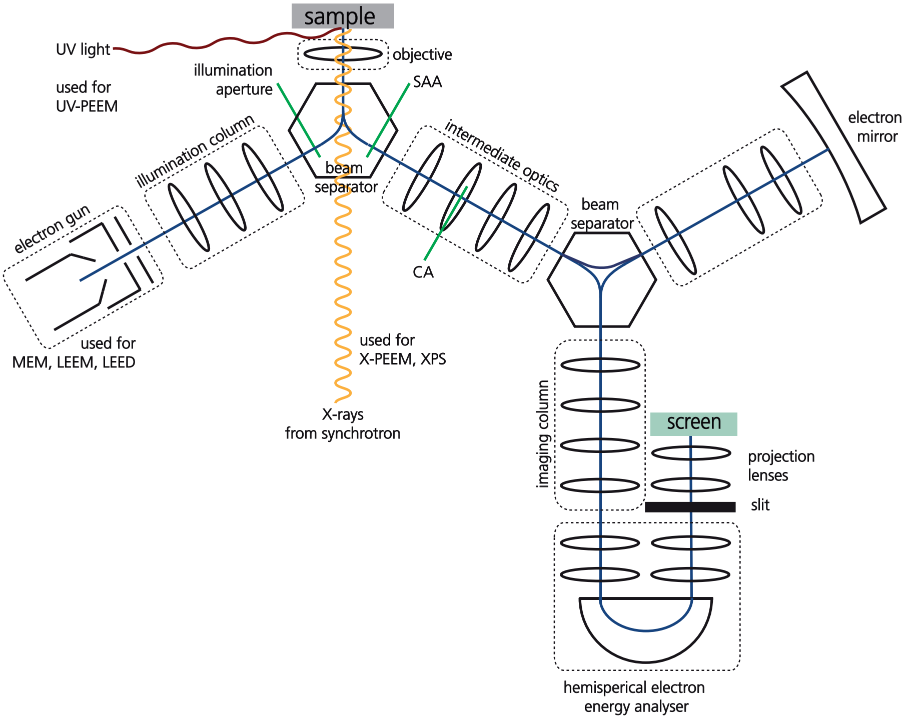
sample
UV light
used for
UV-PEEM
illumination
aperture
objective
SAA
illumination column
beam
separator
intermediate optics
electron
mirror
electron gun
beam
separator
CA
used for
MEM, LEEM, LEED
used for
X-PEEM, XPS
X-rays
from synchrotron
imaging column
screen
projection
lenses
slit
hemisperical electron
energy analyser

Figure 22: Schematic of the AC-SPELEEM setup now situated at the MAXPEEM beamline, MAXIV laboratory. There are three different sources for imaging: an UV-light source for UV-PEEM, an electron gun for MEM, LEEM, and LEED, and X-rays from the synchrotron for XPEEM, and XPS. The electron trajectories are marked in blue, the ellipses depict electron lenses.The slit after the energy analyzer can be used to select photoelectrons with a selected energy. (The aberration correction column with the electron mirror was added after the data presented in Paper II was collected.)

Other microscopes that were used in this thesis include the XPEEM at the HERMES beamline [119, 120] at Synchrotron Soleil, Saint-Aubin, France and the LEEM III situated at the Institute for Solid State Physics, University of Bremen, Bremen, Germany. An in depth coverage of the historic development and theoretical concepts behind cathode lens microscopy can be found in Ref. [53], a book written by one of the inventors of LEEM and PEEM, Ernst Bauer.

A wide range of electron-sample interactions can be used for imaging, e.g. reflected electrons, elastically or inelastically scattered electrons, thermionic emitted electrons, and (X-ray) photoelectrons [121]. The following section will give an introduction to the different microscopy techniques used in this thesis, namely MEM, LEEM, XPEEM, and SEM, and compare them.

3.4.1 Mirror Electron Microscopy

Imaging in MEM is easily achievable in a common LEEM setup as additional parts, e.g. energy analyzers, are not necessary. When operating the microscope in MEM mode, the electrons that probe the sample are accelerated to 20 keV in an electron gun. On the way to the sample the electron beam is focused in the illumination column by the condenser lenses. The illumination aperture can be used to adjust the area of the sample that should be illuminated by the electron beam. The magnetic beam separator (sector field) deflects the electron beam by 60° towards the sample, see Fig. 22. The sample itself has a potential of -20 kV-SV (start voltage), see Fig. 3.4.1 a), decelerating the incoming electrons. The negative SV in MEM causes the sample to act as an electrostatic mirror, hence the name mirror electron microscopy. This causes the electrons to be reflected by an equipotential surface several nanometers above the real surface [122]. By adjusting the strength of the condenser lenses the Gaussian image plane (IP), shown in Fig. 24 b), can be projected onto the detector screen, which in this instrument is a MCP (micro-channel plate) detector with a CCD (charge-coupled device) camera.

The contrast in MEM comes from variations in the electric field that originate from the surface topography, differences in work function, magnetic fields and similar [123], as shown in Fig. 23 a). These disturb the trajectory of the electrons on the way towards and back from the equipotential surface [124]. MEM allows for surface studies of amorphous samples as the electrons don't impinge on the surface but interact with the near-surface field of the sample.

The exact contrast formation and resolution in MEM is, however, still under discussion. A recent comparison between different imaging theories can be found

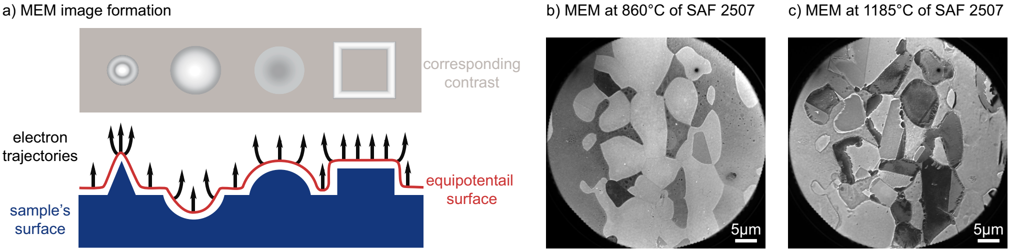
a) MEM image formation

b) MEM at 860°C of SAF 2507

c) MEM at 1185°C of SAF 2507

Figure 23: a) Sketch showing how the topography of the surface affects the contrast in the resulting MEM image. Features on the surface create local fields that cause deviation in the photoelectrons path leading to an altered contrast in the resulting image. (Image according to [126, 127]) Example MEM images of SAF 2507 after a) heating to 860°C and c) 1185°C. At 860°C the typical partitioning between austenite and ferrite can be observed whereas at 1185°C new phases form.

here [125]. Both experimental and theoretical work suggest that the depth resolution in MEM is significantly better than the lateral resolution, which makes MEM sensitive to topographic height variations [53]. Examples on how MEM can be used to follow surface changes due to heating are shown in Fig. 23 b) and c).

3.4.2 Low Energy Electron Microscopy

In LEEM mode the electrons interact with the sample's surface due to the positive SV as in contrast to MEM mode, see Fig. 24 a). However, the electrons are still retarded to low energies, typically ranging from 5 to 100 eV. Hence, the interacting electrons are very surface sensitive. These electrons will then be diffracted by the sample's surface, as explained in section 3.2.2. Besides the diffraction contrast, other contrast mechanisms, e.g. phase contrast, based on the interference of the reflected electrons, and magnetic contrast in spin polarized LEEM (SPLEEM) [128], can be used in LEEM. After the interaction with the surface, the electrons are reaccelerated to 20 keV to enable the focusing by the electromagnetic lenses on their path to the detector. By either projecting the back focal (diffraction) plane (BFP) or the Gaussian IP onto the screen, the LEED pattern or the real space LEEM image can be detected, see Fig. 24 b).

By inserting a contrast aperture (CA) into the BFP a specific diffraction spot can be selected for imaging. If the CA is positioned around the specular (0,0) diffraction spot, the image is collected in bright field LEEM. Bright field LEEM images obtain their contrast from the differences in composition and structure of the sample. By selecting another diffraction spot, areas of the sample with the same structure as the diffraction spot chosen, will appear bright in the LEEM image. This technique is referred to as dark field LEEM and is useful to identify the abundance of a specific structure or to distinguish different domains.

Fig. 24 c) compares images of the same sample made of polycrystalline aluminum recorded in different modes. The leftmost image displays a flat sample topography in MEM mode, the second to the left shows a μ-LEED pattern of one of the grains. The four following images depict LEEM images acquired using diffraction spots from different rotated domains selected with the contrast apertures.

One major advantage of LEEM, and also MEM, is that it allows real-time imaging. This has been successfully applied to study *in-situ* growth processes, e.g. CeO_x-Ru (0001) [129] and graphene on Ni (111) [130]. In this thesis, LEEM movies were used to follow the phase transitions occurring in super duplex stainless steels during heat treatment, complementary to the XPEEM data described in Paper V. Throughout the measurements, the sample's thermal drift and defocussing due to changing distance between the sample's surface and the objective lens are the main problems.

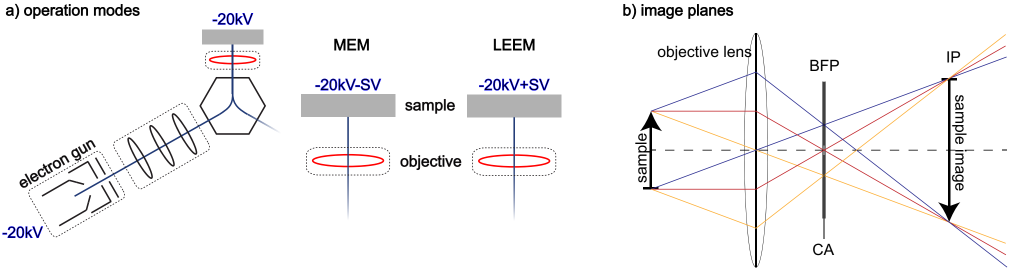

c) images corresponding to the different modes of operation

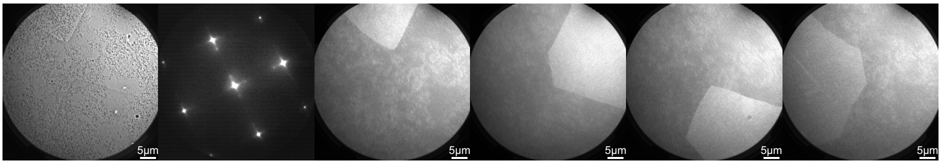

MEM without CA μ-LEED of single grain LEEM images with differently positioned CA in BFP

Figure 24: a) Schematic drawings illustrating the different modes of operation, MEM and LEEM. In MEM a negative SV is applied to the sample leading to reflect the electron beam several nanometers above the surface. If a positive SV is applied the low energy electrons are diffracted at the surface and either the (0,0) or another diffraction spot can be selected for imaging leading to bright field and dark field LEEM images. b) Sketch of image planes. In the BFP the diffraction pattern is formed and in the Gaussian IP the real space image is created. c) Comparison between different imaging modes.

3.4.3 Photoelectron Emission Microscopy

In PEEM the sample is not probed by electrons as in MEM and LEEM but it is illuminated with a relatively wide photon beam. This gives rise to various excitation and emission processes in the same fashion as discussed for spectroscopy in section 3.3. The sample can be illuminated with photons from different sources, typical for lab-based instruments are UV-lamps. The UV-lamp emits photons with a broad spectrum that typically has strong lines around an energy of 5 eV. Instruments situated at synchrotron radiation labs can profit from a bright light source with tunable energy and a narrow wavelength range.

If photons with low energies are used to excite the sample, only electrons from the highest occupied energy level/valence band are emitted and the resulting photoelectrons have a low kinetic energy. Photoelectrons with low kinetic energies can also be generated by secondary events. Here, the primary photoelectron undergoes inelastic scattering and thereby transfers energy to a secondary electron. Since inelastic scattering can occur multiple times, several secondary electrons can be created by one original excitation as the secondary electrons themselves can undergo inelastic scattering leading to a cascade. Secondary electrons have lost the information about the primary excitation event. However, they are frequently used for imaging as they have a high intensity. Variations in the work function arise from differences in chemical composition, e.g. doping. These differences are observed in the onset of the secondary electrons.

To obtain a chemical contrast in the PEEM image, photons with a higher energy, X-rays, are used to emit core-level electrons. A description of the photoexcitation process was given previously in section 3.3.1. To image a certain element a photoexcitation energy above the core-level binding energy of the desired elements is chosen and the SV is adjusted to fulfill Eq. 24. Using the hemispherical energy analyzer, a small energy range of photoelectrons are chosen for imaging. The probing depth in XPEEM is up to 5 nm as determined by the electron inelastic mean free path, see Fig. 16. As the amount of emitted photoelectrons is much lower than the secondary electron emission, PEEM images using core-level photoelectrons are obtained with a longer acquisition times to reach similar counts.

$$E_B = h\nu - SV - \phi \tag{24}$$

Another method to obtain chemical contrast in PEEM is absorption mode (XAS-PEEM). It follows the physical principles described previously for XAS, see section 3.3.2. In XAS-PEEM mode secondary electrons with typically energies of less than 10 eV are used for imaging. The IMFP increases for lower energy electrons and the primary excitation can originate from deeper within the sample, hence the probing depth increases to up to 10 nm. An advantage of XAS-PEEM is that the instrument does not need to have an energy analyzer as all electrons emitted at a certain excitation energy are used for imaging.

PEEM images display areas with a high concentration of the chosen core-level or absorption edge as bright spots as a high intensity of electrons is reaching the detector from those areas [131]. This allows to directly identify spatial distribution of a specific atom or ion. The lateral resolution of XPEEM images is slightly less than the one achieved in LEEM and is typically around 20 nm. The reduced lateral resolution in PEEM is mainly due to chromatic aberrations. Another effect that occurs at bright light sources, like a synchrotron, is blurring of the image due to space charge effects [132].

When imaging with PEEM there are several factors contributing to the image contrast: work function, chemical composition, surface orientation, electronic structure, local electrostatic fields, areas of altered conductivity, partial charging and magnetic domains. Each of these material properties affects the contrast but to a varying extent depending on which mode of operation is chosen, e.g. the contribution of work function contrast is high when using low excitation energies but very weak at high excitation energies [126]. Additionally, the topography of the surface influences the contrast. Features, e.g. scratches and particles on the surface, alter the potential and lead to deflection, focusing or defocussing of the photoelectrons. How these local fields affect the images is also depending on other experimental parameters, e.g. accelerating voltages [127].

To generate images that only contain the chemical contrast, images are often acquired in so called stacks. A stack of images typically varies the binding

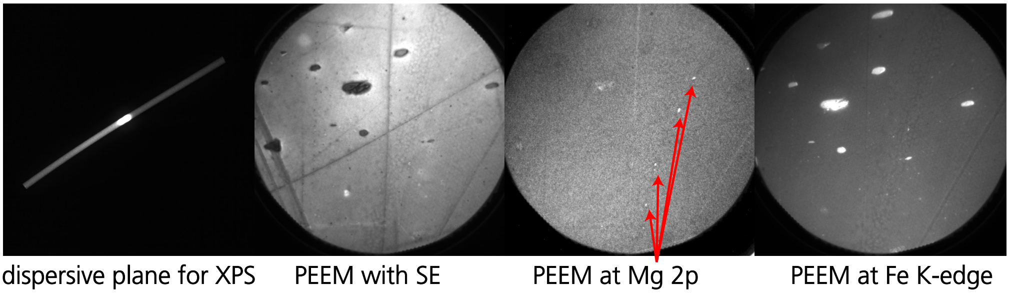

Figure 25: Imaging modes using the energy analyzer. Left image of the dispersive plane used to create XP spectra, here an Al 2p core-level spectrum of AA 6063. The following three PEEM images are from the same alloy using different imaging modes. Left PEEM with secondary electrons using mostly a work function and topography contrast, center showing a chemical contrast corresponding to the Mg 2p core-level, right XAS-PEEM image obtained at the Fe K-edge.

or photon energy range depending on the mode to scan across a core-level or absorption edge in small energy steps. This way images at the core-level peak or on the absorption edge can be background corrected by subtracting an image acquired before the respective peak showing only contrast due to other effects, e.g. topography.

Fig. 25 shows dispersive plane used to create XP spectra and three different PEEM images obtained from the same sample area. The leftmost PEEM image has a contrast mainly from work function and topographic differences, whereas the center and right image have mainly an element specific contrast. The center image was recorded using the Mg 2p core-level binding energy and shows small magnesium particles segregated along the grain boundary. The rightmost image was acquired by using the Fe K-absorption edge, which enables the identification of large iron-rich particles.

A review on the historic development of XPEEM over the past decades can be found here [133] and an overview on recent advances in the field is given in [134].

3.4.4 Scanning Electron Microscopy

SEM has been used as an additional technique to characterize the surface of the samples studied in this thesis. SEM is a raster scanning technique in contrast to the previously discussed microscopy techniques. Here, a narrow focused electron beam, typically 0.1-5 nm, is scanned across an array of positions on the surface of the sample and a signal is detected for each position. The image is then constructed pixel-by-pixel correlating the scanning position and it's corresponding detected signal.

As SEMs also use electrons as probes, they typically require UHV conditions as discussed previously, see section 3.1.4. Fig. 26 a) shows a schematic digram of a SEM in which the entire pathway of the electrons is evacuated. The electrons used in SEM are generated by an electron gun, as described in section 3.1.1, and accelerated over a voltage, typically 1-30 kV. The condenser lenses are used to bundle the electrons in the beam into a given aperture size. By adjusting the strength of the condenser lenses and the diameter of the aperture, the probe current reaching the sample is set. The objective lens focuses the beam and the deflection coils position the beam on the sample allowing the beam to raster scan over the sample's surface.

Once the electrons interact with the sample, several different signals can be collected using designated detectors. Due to the difference in the interaction of the

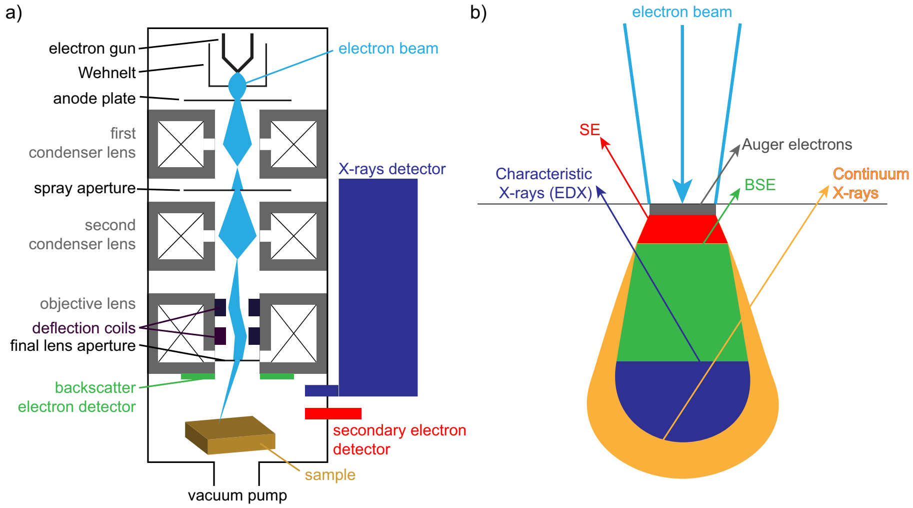
a)
electron gun
Wehnelt
anode plate
first condenser lens
spray aperture
second condenser lens
objective lens
deflection coils
final lens aperture
backscatter electron detector
electron beam
X-rays detector
secondary electron detector
sample
vacuum pump
b)
electron beam
SE
Auger electrons
Characteristic X-rays (EDX)
BSE
Continuum X-rays

Figure 26: a) Schematic diagram of a SEM with different detectors for backscattered and secondary electrons as well as X-rays. b) Illustration of interaction volume for the different electron-sample interactions generating different signal, which can used for image generation in SEM.

electrons with the sample resulting in the various signals their probing depth, see Fig. 26 b), and information content changes. This means that complementary information about the sample's surface is obtained by detecting different signals. Other parameters that affect the probing depth are the acceleration voltage, the beam's convergence angle, and the sample's density.

Commonly, backscattered electrons (BSE) are used for imaging, which are incident electrons elastically scattered by the atoms in the sample. These electrons have interacted with atoms located deeper within the sample and they maintain higher energies after the sample interaction, in contrast to the secondary electrons (SE), which provide information on the topography of the sample, as used in Papers II and V.

Other signals that can be detected in SEM include Auger electrons and characteristic X-rays, which are generated when filling a core-hole the decay processes described for XAS, section 3.3.2. The main difference is that the core-hole in SEM was generated by excitation with electrons instead of X-rays. Characteristic X-rays can be used to identify and quantify elements present in the sample if the SEM is equipped with an energy dispersive X-ray (EDX) detector. The continuum X-rays originate from beam electrons being decelerated in the electrical field of the atoms emitting the excess energy in the form of bremsstrahlung. A typical spectrum including characteristic and continuum X-rays is shown in Fig. 12 b). A more in-depth discussion concerning the instrumentation and signal generation in SEM is found in Ref. [135, 136].

3.4.5 Comparison

This chapter introduced a range of different microscopy techniques. The reason for using such a multitude of techniques is that they all use different probe-sample interaction mechanisms for the image creation. Hence, the contrast mechanisms and the probing depth are different. Also the lateral resolution is dependent on the technique as well as on the instrument itself. An overview comparing the key parameters, which are typical for the different techniques, is given in Tab. 5.

Table 5: Comparison of the key parameters of the different microscopy techniques used in this thesis.

Technique	**Interaction**	**Depth**	**Main contrast**	**Resolution**
MEM	reflection of electrons	$\sim$0 nm	topography	$\sim$2 nm
LEEM	diffraction of electrons	$\sim$1 nm	crystal structure	$\sim$2 nm
XPEEM	photoelectron emission	$\sim$5 nm	element/ chemical state	$\sim$20 nm
XAS-PEEM	X-ray absorption, secondary electrons	$\sim$10 nm	element/ chemical state	$\sim$20 nm
SEM (BSE)	elastically scattered electrons	$\sim$1 μm	Z of elements	$\sim$1 nm
SEM (SE)	secondary electrons	$\sim$100 nm	topography	$\sim$1 nm

4 Summary of Papers

The articles presented in this thesis demonstrates the successful application of surface science techniques to model samples as well as to industrial materials in sample environments ranging from UHV to ambient pressures and even liquid water. Paper I combines XPS and XRR with Electrochemical Impedance Spectroscopy (EIS) to determine the oxide thickness on several aluminum single crystals and industrial aluminum alloys in a range of sample environments. Paper II uses XPS and a range of cathode lens microscopy techniques to follow the decomposition of the aluminum oxide film on an aluminum brazing sheet during heating. The same kind of brazing alloy is studied with XPS in Paper III, highlighting the differences in the surface development caused by a different background pressure. Paper IV continues the comparison between different sample environments on the aluminum standard alloy AA 6063, which was also studied in Paper I. The characterization of the surface oxide is however also done by XPEEM and XRR. The last of the included papers, Paper V, expands the range of studied industrial material to steel. The steel studied, SAF 2507, increases the complexity of the studied materials further as it consists already in its pristine state of two phases: austenite and ferrite. The surface oxide characterization was also performed at elevated temperatures.

Paper I: The thickness of native oxides on aluminum alloys and single crystals

Paper I bridges the the gap between the typical surface science model system, single crystals, and industrial materials by investigating the native oxide thickness of two pure aluminum single crystals, a nickel aluminum single crystal, and four different industrial standard aluminum alloys. The differences between the samples and the information obtained by the three experimental techniques, XPS, XRR, and EIS, used are discussed.

In XPS the oxide thickness is deduced from the fitted intensities of the oxide and the metallic peaks in the aluminum spectrum. Additionally, the tabulated volume densities for aluminum and aluminum oxide as well as the IMFP for both layers are necessary to estimate the thickness according to Eq. 23. Calculating the thickness according to this model, which assumes a pure and homogeneous oxide and metal layer, is more descriptive of an aluminum single crystal than of an alloy since it does not take into account the additional oxide intensities of other alloying elements like magnesium.

Further, the variation in the IMFP and volume density by the presence of alloying elements is neglected making the thickness deduced by XPS approximative.

The thickness obtained from XRR are directly derived from the fits of the reflectivity curve. In Paper I, a multilayer model was fitted in which every layer is assigned a certain thickness and electron density. Since the initial parameters for the electron densities are optimized during the fitting procedure, the thickness obtained by XRR are not sensitive to the composition of the initial model.

In EIS the oxide layer is modeled as a parallel plate capacitor, which has a specific dielectric constant related to the structure and composition of the oxide. Since the same value for the dielectric constant was used for all samples, the calculated thickness is more reliable for the single crystals than for the alloys.

All three techniques indicate that the native oxide layer is thicker on aluminum alloys than on the single crystals. The increased thickness for the alloyed samples can be explained first of all by the grain structure. The single crystals have no grain boundaries that can act as transfer sites for ions and therefore they have a smaller mass transfer rate than the polycrystalline samples. Another aspect is the presence of alloying elements which exhibit different chemical reactivities and disrupt the continuous oxide film. Placing the samples in water also lead to an increased oxide thickness.

Paper II: Surface development of an aluminum brazing sheet during heating studied by XPEEM and XPS

Paper II focuses entirely on an industrial material: An aluminum alloy brazing sheet. Tracing the chemical changes on the surface of these brazing sheets is of great interest since the surface determines how well two work pieces can be joined by brazing. A combination of microscopy and spectroscopy techniques was used to follow the surface development during heating to the melting temperature of the braze cladding.

The chemical changes were studied with XPEEM for the three main elements in the braze cladding aluminum, silicon, and magnesium. To allow for the generation of XP spectra of certain areas within the XPEEM images, they were obtain in stacks. Here, images are acquired for a binding energy range of 10 eV in 0.25 eV steps. XPEEM stacks are particularly useful for inhomogeneous samples, like alloys, since it makes it possible to follow local chemical changes of different particles or phases simultaneously, as shown in Paper II Fig. 6. To understand how the sample is changing in average, conventional XPS measurements were performed for Al 2p, Si 2p, Mg 2p, and O 1s core-levels. Complementary to the chemical information, the sample's topography was studied with MEM/LEEM. Additionally, SEM images were recorded *ex-situ* to image the sample's topography after reoxidizing in air.

Using the different techniques, mixed aluminum and silicon-rich particles were identified as well as the formation of $MgAl_2O_4$-rich areas at 540°C. Further, micrometer large metallic magnesium particles segregated to the surface at 560°C. At the same temperature, the surface changes from being rich in aluminum and silicon oxides to a mainly metallic surface without silicon. By increasing the temperature to 580°C magnesium evaporates leaving a metallic aluminum surface behind. A sketch summarizing the chemical changes can be found in Paper II Fig. 10. It shows how the heterogeneous surface is being transformed from an oxide to a metallic surface by the diffusion of magnesium and how locally new $MgAl_2O_4$ phases are formed.

Paper III: Surface development of a brazing alloy during heat treatment–a comparison between UHV and APXPS

Since the actual industrial brazing process is not performed under UHV conditions, Paper III compares the surface development of aluminum brazing sheets under two experimental conditions: in UHV and in 0.01 mbar of oxygen. To allow XPS measurements at pressures exceeding the typical UHV environment a dedicated APXPS setup was used. The SPECIES beamline at the MAX IV laboratory supports measurements in pressures up to 25 mbar by combining a X-ray transparent window into a reaction cell with a differential pumped analyzer.

For the comparison, changes in thickness and composition of the surface oxide were followed after heating to 300°C, 400°C, and 500°C. The oxide thickness determined by XPS is similar for both measurements at RT, about 50 Å, and after heating to 300°C. After heating to 400°C and 500°C however, major differences occurred. After heating to 400°C, the oxide thickness increased for both sets but the gain in thickness is higher for the sample in the oxygen environment. By further heating to 500°C, the oxide thickness decreases for the sample in UHV to 37 Å, whereas the oxide in the oxygen environment increases even further to at least 88 Å. This change in oxide thickness growth can be directly related to the change in oxide composition. In the UHV case, an enrichment of magnesium and silicon oxides in the alumina is observed, as was also reported in Paper II. However, the amount of non-aluminum oxides does not exceed 5.5%. The sample heated within an oxygen rich atmosphere, however, shows a complete transition from aluminum oxide to magnesium oxide throughout the heat treatment.

These two sets of measurements highlight that the surface development strongly depends on the environment in which the sample is heated. Further, it underlines the need for experimental techniques to be adapted to industrial-like sample conditions to obtain knowledge relevant for the production and processing of these materials.

Paper IV: Surface Oxide Development on Aluminum Alloy 6063 during Heat Treatment

The strong influence of the partial oxygen pressure on the development of the surface oxide covering an industrial aluminum alloy is also shown in Paper IV, where the aluminum alloy standard 6063 is investigated during heating from room temperature up to 500°C using a range of synchrotron radiation based surface science techniques.

Similar to Paper I, XRR measurements enable to follow the changes in thickness of the oxide and XPS provides, additionally to the thickness estimate, information on the chemical composition. Further, XPEEM was used to study the lateral distribution of alloying elements. The effects of heat treatment on AA 6063 are similar to the effects observed for the brazing alloy studied in Papers II and III. At ambient pressures the surface oxide is dominated by MgO at elevated temperatures, whereas at UHV conditions aluminum oxides remain present at the surface. At UHV conditions the distribution of the alloying elements was studied with XPEEM showing that iron-rich particles ranging from 0.5 μm to 4 μm in diameter were distributed across the surface and that these particles were mainly unaffected by heating up to 500°C. Further, the segregation of magnesium-rich particles at grain boundaries and at elevated temperatures within the grain was observed. The segregation of magnesium at the surface in UHV occurs first at grain boundaries at 300°C and at certain places all over the sample at 400°C.

Further, the initial oxide thickness of 45 Å as determined with XPS and XRR is in good agreement with the thickness determined for the same alloy in Paper I. Heating up to 300°C lead to a decrease in thickness to 30 Å. The further growth is governed by the background pressure, resulting in an oxide thickness of 63 Å after heating to 500°C in 10^{-2}mbar of air. The dependence of the surface oxide thickness on the sample environment was emphasized by XRR measurements indicating that higher partial oxygen pressure leads to increased oxide formation.

Paper V: Surface Development of Super Duplex Stainless Steel SAF 2507 during Heat Treatment

Paper V applies the techniques from the previous papers to a new class of materials: steels. In this particular case a super duplex stainless steel with 25% Cr and 7% Ni, SAF 2507. SDSS introduce extra challenges in comparison with the aluminum alloys as they already in their pristine condition exhibit a dual phase structure consisting of typically equal volume fractions of austenite and ferrite. In addition, the chemical composition of these two phases is not the same as different alloying elements stabilize different phases. Further, it is known that SDSS form a range of unwanted phases at elevated temperatures. Moreover, changes in the passive film on the SDSS affect their corrosion resistance, which is of major importance as they find application in corrosive environments. To study the overall changes in the surface near region XPS measurements were performed in UHV at RT and after heating to 400°C, 700°C, and 800°C. The segregation of the different alloying elements in the various phases was observed with XAS-PEEM after the exposure to temperatures up to 1000°C.

The XPS data shows that the native oxide consist mainly of iron and chromium oxides with small amounts of molybdenum oxides. By exposure to higher temperatures the composition changes to a mixed CrMnMo oxide. After heating the sample to 800° the sample's surface is nearly completely reduced and the remaining oxide contains embedded ammonium while also chromium nitrides are present. Imaging with XPEEM allows to follow the partitioning of the alloying elements into the different phases. After heating to 500°C the typical duplex structure is still present. After exposing the sample to higher temperatures a multitude of phases forms with varying content of alloying elements. The imaged surface after heating to 1000°C is dominated by three phases, of which the chromium-rich one exhibits the formation of terraces on the surface. The iron and chromium rich phase is disrupted by needle shaped particles which are depleted of iron. The third phase is rich in Ni and Fe and shows a homogeneous distribution of elements.

This paper highlights how an industrial multi-phase system can be studied at elevated temperature, relevant for the material's field of application, with the means of classical surface science spectroscopy and microscopy techniques.

5 Outlook

A large part of this thesis shows how the material and pressure gap of surface science can be bridged to study 'real' materials in relevant environments. The need to develop instruments that can enable more realistic sample environments are of special interest for the material science community as they will allow to investigate processes *in-situ* which previously have been studied *ex-situ* and often in destructive ways, e.g. elemental depth profiling with sputtering followed by XPS. These processes include strengthening and hardening mechanisms, joining processes like brazing and welding as well as electrochemical processes as corrosion and anodization. Further, protection of surfaces by the application of various coatings and how these coating bond to the surface are exciting questions to study *in-situ*.

All these processes and treatments used in material science have in common that they require conditions that are usually not found in surface science such as high pressures and temperature as well as wet conditions. However, some surface science techniques are already more commonly applied to study industrial materials. Examples of these are *in-situ* electrochemical atomic force microscopy (EC-AFM) [137, 138], environmental SEM and TEM [139, 140], *in-situ* anodization of aluminum alloys [141], and phase transformation and corrosion with XRD [142, 143]. Techniques that are rarely used in the material science community include the methods used in this thesis, even though they have a great potential for further studies.

One of the developments in APXPS allow now to study the interface between solids and gases or even liquids by applying various sample arrangements [144, 145]. Especially, the use of hard X-rays can facilitate the probing of these interfaces as the IMFP for higher energy electrons increases allowing for longer probing depth [146]. Even ambient pressure scanning photoelectron microscope (SPEM) has been successfully demonstrated [147]. The combination of APXPS with electrochemistry is very promising from an material science perspective as it will allow to study the corrosion in liquids *in-situ* at different potentials [148].

Another promising development in XPS is the installation of fast detectors, which are currently mainly used for temperature-programmed (TP) measurements that study thermal desorption adsorption phenomena [149] by obtaining fast high-resolution XP spectra. Instruments equipped with a fast detector and an ambient pressure cell can in the future be used to study segregation properties in industrial material in a non-destructive way. So far the combination of APXPS with fast detection has been used for *in situ* studies of heterogeneous catalysts [101, 150]. By following the segregation behavior of alloying elements in the ms timescale, insights in the diffusion kinetics could be obtained.

To follow changes at the surface with chemical sensitivity or with phase contrast is possible with LEEM and PEEM. However, these cathode lens microscopy techniques encounter major obstacles when trying to combine with more realistic sample environments as a high acceleration voltage is applied between the sample and the objective lens. Nevertheless, first attempts of constructing XPEEM setups that can probe in gas [151] or through liquid have been made [117, 152].

A major strength of XPEEM and LEEM instruments is that they can perform measurements with video-rate frequency which will enable real-time monitoring of surface processes. To compensate for the thermal drift that is occurring during heating experiments, samples can be patterned with focused ion beam lithography (FIB). This will allow an easy recognition of the different areas on the sample even if large thermal drift occurs at high temperatures.

First results from using LEEM movies to follow the phase transitions occurring at elevated temperatures in super duplex stainless steels are shown in Fig. 27. Here, LEEM images with a FoV of 50 μm were acquired every 0.5 sec binning two images with an exposure time of 0.25 sec while heating the sample from RT up to 1340°C.

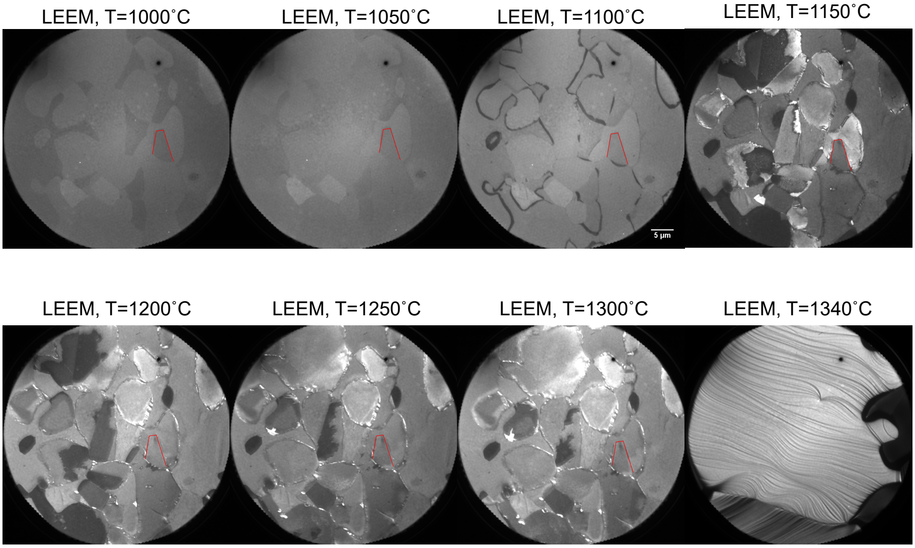

Figure 27: Image series taken from an *in-situ* LEEM movie heating of the duplex stainless steel SAF 2507 highlighting how the phase changes can be followed live. The red marker is used to indicate the same area.

The heating was interrupted for further characterization at certain temperatures to obtain μ-LEED patterns from regions of interest, see Fig. 28, and I(V)-LEEM stacks, which are a sequence of images with an increasing electron energy in bright-field mode. The (00)-beam I(V)-LEEM image can be used to create I(V) curves for each pixel in the image by plotting the recorded intensity as a function of the kinetic energy. These I(V)-curves can then be used for structural fingerprinting [153, 154]. By matching the I(V)-curves from regions with known μ-LEED patterns with the individual I(V) of each pixel, it will be possible to calculate the relative abundance of a phase within the FoV of the LEEM image. Repeating this at several places on the sample at different temperatures can then be used to generate 'phase diagrams'. The data presented in Fig. 27 and 28 will provide additional information to the data presented in Paper V, which focused more on the chemical changes of the surface oxide composition of the super duplex stainless steel, SAF 2507.

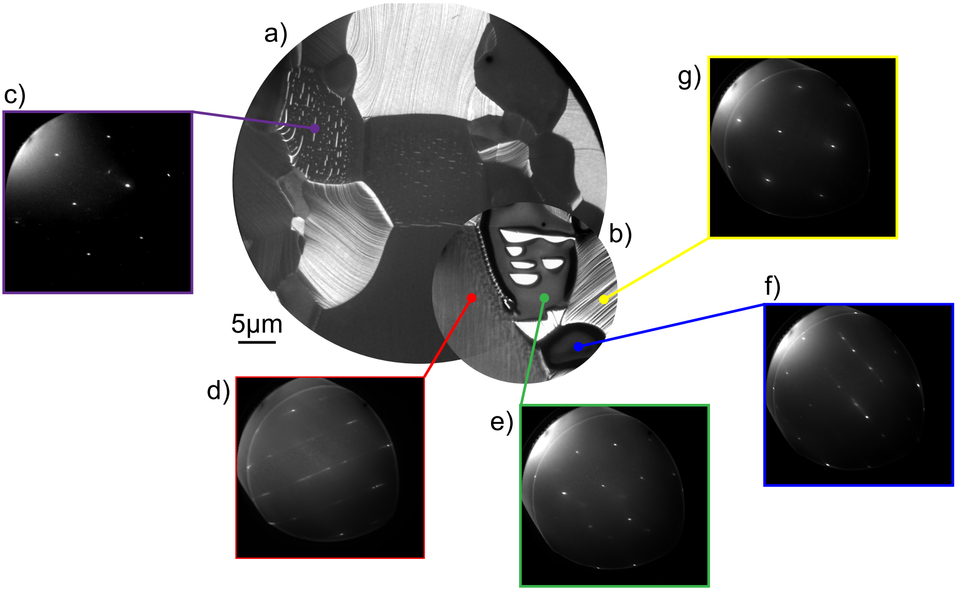

Figure 28: a) and b) are overlayed LEEM images of SAF 2507 after two heating cycles while the sample is at 300°C. c)-g) LEED patterns from the indicated areas.

These few examples show that the topic of this thesis, using surface science techniques on industrial samples in environments that mimic the industrial processes in various ways, has the potential for further development in the fields of surface and material science. The main challenges will be to handle increasingly complex experimental set-ups and the difficulties arising from data sets that depend on an increasing number of variables.

References

[1] Bureau of International Recycling. "World steel production and scrap consumption from 2005 to 2017 (in million metric tons) `https://www.statista.com/statistics/270835/world-steel-production-and-scrap-consumption/`". Web: Statista, accessed 26-Oct-2018.

[2] US Geological Survey. "Countries with the largest smelter production of aluminum from 2010 to 2017 (in 1,000 metric tons) `https://www.statista.com/statistics/264624/global-production-of-aluminum-by-country/`". Web: Statista, accessed 26-Oct-2018.

[3] P. Roberts. *Industrial Brazing Practice, Second Edition.* CRC Press, 2013. doi:10.1201/b14061.

[4] E. Lundgren. "SSF Program ALUminium oXides for processing and products ALUX `http://www.alux.lu.se/about/`". Web, accessed 23-Oct-2018.

[5] R. Lumley. *Fundamentals of aluminium metallurgy : production, processing and applications.* Cambridge : Woodhead Publishing Limited, 2010. doi:10.1533/9780857090256.

[6] C. McConville, D. Seymour, D. Woodruff and S. Bao. "Synchrotron radiation core level photoemission investigation of the initial stages of oxidation of Al(111)". *Surface Science*, 188(1-2), 1–14, 1987. doi:10.1016/s0039-6028(87)80138-3.

[7] C. Berg, S. Raaen, A. Borg, J. N. Andersen, E. Lundgren and R. Nyholm. "Observation of a low-binding-energy peak in the 2 pcore-level photoemission from oxidized Al(111)". *Physical Review B*, 47(19), 13063–13066, 1993. doi:10.1103/physrevb.47.13063.

[8] L. Jeurgens, W. Sloof, F. Tichelaar, C. Borsboom and E. Mittemeijer. "Determination of thickness and composition of aluminium-oxide overlayers on aluminium substrates". *Applied Surface Science*, 144-145, 11–15, 1999. doi:10.1016/s0169-4332(98)00755-7.

[9] P. Snijders, L. Jeurgens and W. Sloof. "Structure of thin aluminium-oxide films determined from valence band spectra measured using XPS". *Surface Science*, 496(1-2), 97–109, 2002. ISSN 0039-6028. doi:http://dx.doi.org/10.1016/S0039-6028(01)01591-6.

[10] N. Cai, G. Zhou, K. Müller and D. E. Starr. "Effect of oxygen gas pressure on the kinetics of alumina film growth during the oxidation of Al(111) at room temperature". *Physical Review B*, 84(12), 2011. doi:10.1103/physrevb.84.125445.

[11] M. Schmid, G. Leonardelli, R. Tscheließnig, A. Biedermann and P. Varga. "Oxygen adsorption on Al(111): low transient mobility". *Surface Science*, 478(3), L355–L362, 2001. doi:10.1016/s0039-6028(01)00967-0.

[12] D. Starodub, T. Gustafsson and E. Garfunkel. "The reaction of O_2 with Al(110): a medium energy ion scattering study of nano-scale oxidation". *Surface Science*, 552(1-3), 199–214, 2004. doi:10.1016/j.susc.2004.01.019.

[13] F. Goodwin, S. Guruswamy, K. U. Kainer, C. Kammer, W. Knabl, A. Koethe, G. Leichtfried, G. Schlamp, R. Stickler and H. Warlimont. *Metals*, pages 161–430. Springer Berlin Heidelberg, Berlin, Heidelberg, 2005. ISBN 978-3-540-30437-1. doi:10.1007/3-540-30437-1_5.

[14] W. Hosford. *Physical Metallurgy, Second Edition.* Informa UK Limited, 2010. doi:10.1201/b15858.

[15] A. N. Adamson, E. J. Bloore and A. R. Carr. "Basic Principles of Bayer Process Design". In "Essential Readings in Light Metals", pages 100–117. Wiley-Blackwell, 2013. doi:10.1002/9781118647868.ch14.

[16] W. E. Haupin. "Principles of Aluminum Electrolysis". In "Essential Readings in Light Metals", pages 3–11. Springer Nature, 2016. doi:10.1007/978-3-319-48156-2_1.

[17] D. V. Schroeder. *An Introduction to Thermal Physics.* Addison Wesley Pub Co Inc, 1999. ISBN 0201380277. doi:https://doi.org/10.1016/B978-0-12-803304-3.09981-6.

[18] I. Levin and D. Brandon. “Metastable Alumina Polymorphs: Crystal Structures and Transition Sequences”. *Journal of the American Ceramic Society*, 81(8), 1995–2012, 2005. doi:10.1111/j.1151-2916.1998.tb02581.x.

[19] SpringerMaterials. “Sapphire (Al_2O_3-rhom) Crystal Structure: Datasheet from “PAULING FILE Multinaries Edition – 2012””. Web, accessed 14-Jun-2017.

[20] K. Momma and F. Izumi. “VESTA 3for three-dimensional visualization of crystal, volumetric and morphology data”. *Journal of Applied Crystallography*, 44(6), 1272–1276, 2011. doi:10.1107/s0021889811038970.

[21] E. Balan, M. Lazzeri, G. Morin and F. Mauri. “First-principles study of the OH-stretching modes of gibbsite”. *American Mineralogist*, 91(1), 115–119, 2006. doi:10.2138/am.2006.1922.

[22] J. Evertsson, F. Bertram, F. Zhang, L. Rullik, L. Merte, M. Shipilin, M. Soldemo, S. Ahmadi, N. Vinogradov, F. Carlà, J. Weissenrieder, M. Göthelid, J. Pan, A. Mikkelsen, J.-O. Nilsson and E. Lundgren. “The thickness of native oxides on aluminum alloys and single crystals”. *Applied Surface Science*, 349, 826–832, 2015. doi:10.1016/j.apsusc.2015.05.043.

[23] L. Jeurgens, W. Sloof, F. Tichelaar and E. Mittemeijer. “Thermodynamic stability of amorphous oxide films on metals: Application to aluminum oxide films on aluminum substrates”. *Physical Review B*, 62(7), 4707–4719, 2000. doi:10.1103/physrevb.62.4707.

[24] N. L. Sukiman, X. Zhou, N. Birbilis, A. Hughes, J. M. C. Mol, S. J., X. Zhou and G. E. “Durability and Corrosion of Aluminium and Its Alloys: Overview, Property Space, Techniques and Developments”. In “Aluminium Alloys - New Trends in Fabrication and Applications”, InTech, 2012. doi:10.5772/53752.

[25] C. Vargel. “Physical Properties of Aluminium”. In “Corrosion of Aluminium”, pages 19–20. Elsevier BV, 2004. doi:10.1016/b978-008044495-6/50007-0.

[26] B. McGurran and M. Nicholas. “A study of aluminium brazes using hot-stage scanning electron microscopy”. *Journal of Materials Science*, 19(8), 2713–2718, 1984. ISSN 0022-2461. doi:10.1007/BF00550829.

[27] D. K. Creber, J. Ball and D. J. Field. “A Mechanistic Study of Aluminum Vacuum Brazing”. In “SAE Technical Paper”, SAE International, 1987. doi:10.4271/870185.

[28] The Aluminum Association. “`https://www.aluminum.org`”. Web, accessed 01-Nov-2018.

[29] N. Birbilis and R. G. Buchheit. “Electrochemical Characteristics of Intermetallic Phases in Aluminum Alloys”. *Journal of The Electrochemical Society*, 152(4), B140, 2005. doi:10.1149/1.1869984.

[30] F. Zhang, J.-O. Nilsson and J. Pan. “In Situ and Operando AFM and EIS Studies of Anodization of Al 6060: Influence of Intermetallic Particles”. *Journal of The Electrochemical Society*, 163(9), C609–C618, 2016. doi:10.1149/2.0061610jes.

[31] F. Bertram, F. Zhang, J. Evertsson, F. Carlà, J. Pan, M. E. Messing, A. Mikkelsen, J.-O. Nilsson and E. Lundgren. “In situ anodization of aluminum surfaces studied by x-ray reflectivity and electrochemical impedance spectroscopy”. *Journal of Applied Physics*, 116(3), 034902, 2014. doi:10.1063/1.4890318.

[32] J. Evertsson, F. Bertram, L. Rullik, G. Harlow and E. Lundgren. “Anodization of Al(100), Al(111) and Al Alloy 6063 studied in situ with X-ray reflectivity and electrochemical impedance spectroscopy”. *Journal of Electroanalytical Chemistry*, 799, 556–562, 2017. doi:10.1016/j.jelechem.2017.07.010.

[33] N. A. Vinogradov, G. S. Harlow, F. Carlà, J. Evertsson, L. Rullik, W. Linpé, R. Felici and E. Lundgren. “Observation of Pore Growth and Self-Organization in Anodic Alumina by Time-Resolved X-ray Scattering”. *ACS Applied Nano Materials*, 1(3), 1265–1271, 2018. doi:10.1021/acsanm.7b00303.

[34] J. Evertsson, N. A. Vinogradov, G. S. Harlow, F. Carlà, S. R. McKibbin, L. Rullik, W. Linpé, R. Felici and E. Lundgren. “Self-organization of porous anodic alumina films studied in situ by grazing-incidence transmission small-angle X-ray scattering”. *RSC Advances*, 8(34), 18980–18991, 2018. doi:10.1039/c8ra02913j.

[35] R. Smallman and A. Ngan. “Mechanical properties II — Strengthening and toughening”. In “Physical Metallurgy and Advanced Materials Engineering”, pages 385–446. Elsevier, 2007. doi:10.1016/b978-075066906-1/50010-x.

[36] W. Martienssen and H. Warlimont. *Springer Handbook of Condensed Matter and Materials Data*. Berlin, Heidelberg: Springer-Verlag, 2005. doi:10.1007/3-540-30437-1.

[37] K. Lo, C. Shek and J. Lai. “Recent developments in stainless steels”. *Materials Science and Engineering: R: Reports*, 65(4-6), 39–104, 2009. doi:10.1016/j.mser.2009.03.001.

[38] E. C. Bain and W. E. Griffiths. “An introduction to the iron-chromium-nickel alloys”. *Trans. AIME*, 75(166), 166–211, 1927.

[39] H. W. Paxton and J. B. Austin. “Historical account of the contributions of E. C. Bain”. *Metallurgical Transactions*, 3(5), 1035–1042, 1972. doi:10.1007/bf02642435.

[40] H. Solomon. “Stainless Steels: Duplex”. In “Encyclopedia of Materials: Science and Technology”, pages 8802–8804. Elsevier, 2001. doi:10.1016/b0-08-043152-6/01581-3.

[41] J.-O. Nilsson. “Super duplex stainless steels”. *Materials Science and Technology*, 8(8), 685–700, 1992. doi:10.1179/mst.1992.8.8.685.

[42] C. Shek, K. Wong and J. Lai. “Review of temperature indicators and the use of duplex stainless steels for life assessment”. *Materials Science and Engineering: R: Reports*, 19(5-6), 153–200, 1997. doi:10.1016/s0927-796x(97)00001-6.

[43] L. Weber and P. Uggowitzer. “Partitioning of chromium and molybdenum in super duplex stainless steels with respect to nitrogen and nickel content”. *Materials Science and Engineering: A*, 242(1-2), 222–229, 1998. doi:10.1016/s0921-5093(97)00521-2.

[44] T. J. Mesquita, E. Chauveau, M. Mantel and R. P. Nogueira. “A XPS study of the Mo effect on passivation behaviors for highly controlled stainless steels in neutral and alkaline conditions”. *Applied Surface Science*, 270, 90–97, 2013. doi:10.1016/j.apsusc.2012.12.118.

[45] I. Alvarez-Armas. “Duplex Stainless Steels: Brief History and Some Recent Alloys”. *Recent Patents on Mechanical Engineeringe*, 1(1), 51–57, 2008. doi:10.2174/2212797610801010051.

[46] J. Simmons. “Overview: high-nitrogen alloying of stainless steels”. *Materials Science and Engineering: A*, 207(2), 159–169, 1996. doi:10.1016/0921-5093(95)09991-3.

[47] E. Bettini, U. Kivisäkk, C. Leygraf and J. Pan. “Study of Corrosion Behavior of a 2507 Super Duplex Stainless Steel : Influence of Quenched-in and Isothermal Nitrides”. *International Journal of Electrochemical Science*, 9(1), 61–80, 2014. QC 20140123. Updated from accepted to published.

[48] D. M. E. Villanueva, F. C. P. Junior, R. L. Plaut and A. F. Padilha. "Comparative study on sigma phase precipitation of three types of stainless steels: austenitic, superferritic and duplex". *Materials Science and Technology*, 22(9), 1098–1104, 2006. doi:10.1179/174328406x109230.

[49] J. del Abra-Arzola, M. García-Rentería, V. Cruz-Hernández, J. García-Guerra, V. Martínez-Landeros, L. Falcón-Franco and F. Curiel-López. "Study of the effect of sigma phase precipitation on the sliding wear and corrosion behaviour of duplex stainless steel AISI 2205". *Wear*, 400-401, 43–51, 2018. doi:10.1016/j.wear.2017.12.019.

[50] H.-S. Wang. "Effect of Welding Variables on Cooling Rate and Pitting Corrosion Resistance in Super Duplex Stainless Weldments". *MATERIALS TRANSACTIONS*, 46(3), 593–601, 2005. doi:10.2320/matertrans.46.593.

[51] V. A. Hosseini, M. A. V. Bermejo, J. Gårdstam, K. Hurtig and L. Karlsson. "Influence of multiple thermal cycles on microstructure of heat-affected zone in TIG-welded super duplex stainless steel". *Welding in the World*, 60(2), 233–245, 2016. doi:10.1007/s40194-016-0300-5.

[52] C. Örnek and D. L. Engelberg. "Correlative EBSD and SKPFM characterisation of microstructure development to assist determination of corrosion propensity in grade 2205 duplex stainless steel". *Journal of Materials Science*, 51(4), 1931–1948, 2015. doi:10.1007/s10853-015-9501-3.

[53] E. Bauer. *Surface Microscopy with Low Energy Electrons*. Springer New York, 2014. doi:10.1007/978-1-4939-0935-3.

[54] J. D. Jackson. *Classical electrodynamics*. New York : Wiley, 1999.

[55] A. Liénard. "Champ Électrique et Magnétique". *LÉclairage Électrique*, 16, 5–14, 53–59, 106–112, 1898.

[56] A. Hofmann. *The Physics of Synchrotron Radiation*. Cambridge University Press, 2004.

[57] K. Wille. *The Physics of Particle Accelerators: An Introduction*. OXFORD UNIV PR, 2001. ISBN 0198505493.

[58] P. Atkins and J. de Paula. *Physical Chemistry, 9th Edition*. W. H. Freeman, 2009. ISBN 1429218126.

[59] D. M. Jens Als-Nielsen. *Elements of Modern X-ray Physics*. John Wiley and Sons Ltd, 2011. ISBN 0470973943.

[60] “X-Ray Focusing Elements Characterization”. In “Nanobeam X-Ray Scattering”, pages 39–87. Wiley-VCH Verlag GmbH, 2013. doi:10.1002/9783527655069.ch3.

[61] M. Tolan. *X-Ray Scattering from Soft-Matter Thin Films*. Springer Berlin Heidelberg, 1999. doi:10.1007/bfb0112834.

[62] G. Bracco and B. Holst (Editors). *Surface Science Techniques*. Springer Berlin Heidelberg, 2013. doi:10.1007/978-3-642-34243-1.

[63] M. Sardela (Editor). *Practical Materials Characterization*. Springer New York, 2014. doi:10.1007/978-1-4614-9281-8.

[64] C. Davisson and L. H. Germer. “Diffraction of Electrons by a Crystal of Nickel”. *Physical Review*, 30(6), 705–740, 1927. doi:10.1103/physrev.30.705.

[65] Nobel Media AB. “The Nobel Prize in Physics 1937 `https://www.nobelprize.org/prizes/physics/1937/summary/`”. Web, accessed 26-Oct-2018.

[66] J. W. Niemantsverdriet. *Spectroscopy in Catalysis*. Wiley VCH Verlag GmbH, 2007. ISBN 3527316515.

[67] M. A. V. Hove, W. H. Weinberg and C.-M. Chan. *Low-Energy Electron Diffraction*. Springer Berlin Heidelberg, 1986. doi:10.1007/978-3-642-82721-1.

[68] H. Hertz. “Über einen Einfluss des ultravioletten Lichtes auf die electrische Entladung”. *Annalen der Physik*, 267(8), 983–1000, 1887. doi:10.1002/andp.18872670827.

[69] A. Einstein. “Über einen die Erzeugung und Verwandlung des Lichtes betreffenden heuristischen Gesichtspunkt”. *Annalen der Physik*, 322(6), 132–148, 1905. doi:10.1002/andp.19053220607.

[70] Nobel Media AB. “The Nobel Prize in Physics 1921 `https://www.nobelprize.org/prizes/physics/1921/summary/`”. Web, accessed 26-Oct-2018.

[71] K. Siegbahn. “Electron Spectroscopy for Atoms, Molecules, and Condensed Matter”. *Science*, 217(4555), 111–121, 1982. doi:10.1126/science.217.4555.111.

[72] Nobel Media AB. “The Nobel Prize in Physics 1981 `https://www.nobelprize.org/prizes/physics/1981/summary/`”. Web, accessed 26-Oct-2018.

[73] S. Tanuma, C. J. Powell and D. R. Penn. “Calculations of electron inelastic mean free paths”. *Surface and Interface Analysis*, 37(1), 1–14, 2005. doi:10.1002/sia.1997.

[74] C. N. Berglund and W. E. Spicer. “Photoemission Studies of Copper and Silver: Experiment”. *Physical Review*, 136(4A), A1044–A1064, 1964. doi:10.1103/physrev.136.a1044.

[75] C. N. Berglund and W. E. Spicer. “Photoemission Studies of Copper and Silver: Theory”. *Physical Review*, 136(4A), A1030–A1044, 1964. doi:10.1103/physrev.136.a1030.

[76] S. Hüfner. *Photoelectron spectroscopy : principles and applications*. Advanced texts in physics. Berlin : Springer, 2003. doi:10.1007/978-3-662-09280-4.

[77] V. Schmidt. “Photoionization of atoms using synchrotron radiation”. *Reports on Progress in Physics*, 55(9), 1483–1659, 1992. doi:10.1088/0034-4885/55/9/003.

[78] M. Grioni. *Photoelectron Spectroscopy*, pages 189–237. Springer Netherlands, Dordrecht, 2006. ISBN 978-1-4020-3337-7. doi:10.1007/1-4020-3337-0_6.

[79] W. B. Jensen. “The Origin of the s, p, d, f Orbital Labels”. *Journal of Chemical Education*, 84(5), 757, 2007. doi:10.1021/ed084p757.

[80] H. N. Russell and F. A. Saunders. “New Regularities in the Spectra of the Alkaline Earths”. *The Astrophysical Journal*, 61, 38, 1925. doi:10.1086/142872.

[81] J. Yeh and I. Lindau. “Atomic subshell photoionization cross sections and asymmetry parameters: $1 \leq Z \leq 103$”. *Atomic Data and Nuclear Data Tables*, 32(1), 1–155, 1985. doi:10.1016/0092-640X(85)90016-6.

[82] B. R. Strohmeier. “An ESCA method for determining the oxide thickness on aluminum alloys”. *Surface and Interface Analysis*, 15(1), 51–56, 1990. ISSN 1096-9918. doi:10.1002/sia.740150109.

[83] M. R. Alexander, G. E. Thompson, X. Zhou, G. Beamson and N. Fairley. “Quantification of oxide film thickness at the surface of aluminium using

XPS". *Surface and Interface Analysis*, 34(1), 485–489, 2002. ISSN 1096-9918. doi:10.1002/sia.1344.

[84] S. Tougaard. "QUASES Software packages to characterize surface nanostructures by analysis of electron spectra `http://www.quases.com/`". Web, accessed 26-Oct-2018.

[85] S. Tanuma, C. J. Powell and D. R. Penn. "Calculations of electorn inelastic mean free paths. II. Data for 27 elements over the 50-2000 eV range". *Surface and Interface Analysis*, 17(13), 911–926, 1991. ISSN 1096-9918. doi:10.1002/sia.740171304.

[86] S. Tanuma, C. J. Powell and D. R. Penn. "Calculations of electron inelastic mean free paths. III. Data for 15 inorganic compounds over the 50-2000 eV range". *Surface and Interface Analysis*, 17(13), 927–939, 1991. ISSN 1096-9918. doi:10.1002/sia.740171305.

[87] K. Siegbahn, C. Nordling, G. Johansson, J. Hedman, P. Hedén, K. Hamrin, U. Gelius, T. Bergmark, L. Werme, R. Manne et al. *ESCA applied to free molecules.* Noviacta. Regia societas scientarum upsaliensis. North-Holland Publishing Company, 1969.

[88] H. Siegbahn and K. Siegbahn. "ESCA applied to liquids". *Journal of Electron Spectroscopy and Related Phenomena*, 2(3), 319–325, 1973. doi:10.1016/0368-2048(73)80023-4.

[89] H. Siegbahn. "Electron spectroscopy for chemical analysis of liquids and solutions". *The Journal of Physical Chemistry*, 89(6), 897–909, 1985. doi:10.1021/j100252a005.

[90] L. Nemec, H. J. Gaehrs, L. Chia and P. Delahay. "Photoelectron spectroscopy of liquids up to 21.2 eV". *The Journal of Chemical Physics*, 66(10), 4450–4458, 1977. doi:10.1063/1.433696.

[91] R. Ballard, S. Barker, J. Gunnell, W. Hagan, S. Pearce, R. West and A. Saunders. "HE(I) Photoelectron spectra of 1,2-ethanediol in the liquid and gas phases". *Journal of Electron Spectroscopy and Related Phenomena*, 14(5), 331–339, 1978. doi:10.1016/0368-2048(78)80007-3.

[92] R. W. Joyner, M. Roberts and K. Yates. "A "high-pressure" electron spectrometer for surface studies". *Surface Science*, 87(2), 501–509, 1979. doi:10.1016/0039-6028(79)90544-2.

[93] D. F. Ogletree, H. Bluhm, G. Lebedev, C. S. Fadley, Z. Hussain and M. Salmeron. “A differentially pumped electrostatic lens system for photoemission studies in the millibar range”. *Review of Scientific Instruments*, 73(11), 3872–3877, 2002. doi:10.1063/1.1512336.

[94] H. Bluhm, K. Andersson, T. Araki, K. Benzerara, G. Brown, J. Dynes, S. Ghosal, M. Gilles, H.-C. Hansen, J. Hemminger, A. Hitchcock, G. Ketteler, A. Kilcoyne, E. Kneedler, J. Lawrence, G. Leppard, J. Majzlam, B. Mun, S. Myneni, A. Nilsson, H. Ogasawara, D. Ogletree, K. Pecher, M. Salmeron, D. Shuh, B. Tonner, T. Tyliszczak, T. Warwick and T. Yoon. “Soft X-ray microscopy and spectroscopy at the molecular environmental science beamline at the Advanced Light Source”. *Journal of Electron Spectroscopy and Related Phenomena*, 150(2-3), 86–104, 2006. doi:10.1016/j.elspec.2005.07.005.

[95] N. Johansson. *Synchrotron-based In Situ Electron Spectroscopy Applied to Oxide Formation and Catalysis.* Ph.D. thesis, Lund University, 2017.

[96] S. Urpelainen, C. Såthe, W. Grizolli, M. Agåker, A. R. Head, M. Andersson, S.-W. Huang, B. N. Jensen, E. Wallén, H. Tarawneh, R. Sankari, R. Nyholm, M. Lindberg, P. Sjöblom, N. Johansson, B. N. Reinecke, M. A. Arman, L. R. Merte, J. Knudsen, J. Schnadt, J. N. Andersen and F. Hennies. “The SPECIES beamline at the MAX IV Laboratory: a facility for soft X-ray RIXS and APXPS”. *Journal of Synchrotron Radiation*, 24(1), 344–353, 2017. doi:10.1107/s1600577516019056.

[97] J. Knudsen, J. N. Andersen and J. Schnadt. “A versatile instrument for ambient pressure x-ray photoelectron spectroscopy: The Lund cell approach”. *Surface Science*, 646, 160–169, 2016. doi:10.1016/j.susc.2015.10.038.

[98] D. F. Ogletree, H. Bluhm, E. D. Hebenstreit and M. Salmeron. “Photoelectron spectroscopy under ambient pressure and temperature conditions”. *Nuclear Instruments and Methods in Physics Research Section A: Accelerators, Spectrometers, Detectors and Associated Equipment*, 601(1-2), 151–160, 2009. doi:10.1016/j.nima.2008.12.155.

[99] J. Zhou, S. Blomberg, J. Gustafson, E. Lundgren and J. Zetterberg. “Visualization of Gas Distribution in a Model AP-XPS Reactor by PLIF: CO Oxidation over a Pd(100) Catalyst”. *Catalysts*, 7(12), 29, 2017. doi:10.3390/catal7010029.

[100] N. M. Martin, M. V. den Bossche, A. Hellman, H. G. önbeck, C. Hakanoglu, J. Gustafson, S. Blomberg, N. Johansson, Z. Liu, S. Axnanda, J. F.

Weaver and E. Lundgren. "Intrinsic Ligand Effect Governing the Catalytic Activity of Pd Oxide Thin Films". *ACS Catalysis*, 4(10), 3330–3334, 2014. doi:10.1021/cs5010163.

[101] N. Johansson, L. R. Merte, E. Grånäs, S. Wendt, J. N. Andersen, J. Schnadt and J. Knudsen. "Oxidation of Ultrathin FeO(111) Grown on Pt(111): Spectroscopic Evidence for Hydroxylation". *Topics in Catalysis*, 59(5-7), 506–515, 2016. doi:10.1007/s11244-015-0521-7.

[102] N. Johansson, S. Sisodiya, P. Shayesteh, S. Chaudhary, J. N. Andersen, J. Knudsen, O. F. Wendt and J. Schnadt. "Sonogashira cross-coupling over Au(1 1 1): from UHV to ambient pressure". *Journal of Physics: Condensed Matter*, 29(44), 444005, 2017. doi:10.1088/1361-648x/aa89c4.

[103] A. R. Head, S. Chaudhary, G. Olivieri, F. Bournel, J. N. Andersen, F. Rochet, J.-J. Gallet and J. Schnadt. "Near Ambient Pressure X-ray Photoelectron Spectroscopy Study of the Atomic Layer Deposition of TiO2 on RuO2(110)". *The Journal of Physical Chemistry C*, 120(1), 243–251, 2015. doi:10.1021/acs.jpcc.5b08699.

[104] R. Timm, A. R. Head, S. Yngman, J. V. Knutsson, M. Hjort, S. R. McKibbin, A. Troian, O. Persson, S. Urpelainen, J. Knudsen, J. Schnadt and A. Mikkelsen. "Self-cleaning and surface chemical reactions during hafnium dioxide atomic layer deposition on indium arsenide". *Nature Communications*, 9(1), 2018. doi:10.1038/s41467-018-03855-z.

[105] H. Bluhm. "X-ray photoelectron spectroscopy (XPS) for in situ characterization of thin film growth". In "In Situ Characterization of Thin Film Growth", pages 75–98. Elsevier, 2011. doi:10.1533/9780857094957.2.75.

[106] Y. Joly and S. Grenier. *Theory of X-Ray Absorption Near Edge Structure*, pages 73–97. John Wiley & Sons, Ltd, 2016. ISBN 9781118844243. doi:10.1002/9781118844243.ch4.

[107] C. S. Schnohr and M. C. Ridgway (Editors). *X-Ray Absorption Spectroscopy of Semiconductors.* Springer Berlin Heidelberg, 2015. doi:10.1007/978-3-662-44362-0.

[108] J. Stöhr. *NEXAFS Spectroscopy.* Springer Berlin Heidelberg, 1992. doi:10.1007/978-3-662-02853-7.

[109] M. Born, E. Wolf, A. B. Bhatia, P. C. Clemmow, D. Gabor, A. R. Stokes, A. M. Taylor, P. A. Wayman and W. L. Wilcock. *Principles of Optics.* Cambridge University Press, 1999. doi:10.1017/cbo9781139644181.

[110] T. O. Menteş, G. Zamborlini, A. Sala and A. Locatelli. "Cathode lens spectromicroscopy: methodology and applications". *Beilstein Journal of Nanotechnology*, 5, 1873–1886, 2014. doi:10.3762/bjnano.5.198.

[111] E. Bauer. "Low energy electron microscopy". *Reports on Progress in Physics*, 57(9), 895–938, 1994. doi:10.1088/0034-4885/57/9/002.

[112] R. Tromp, J. Hannon, A. Ellis, W. Wan, A. Berghaus and O. Schaff. "A new aberration-corrected, energy-filtered LEEM/PEEM instrument. I. Principles and design". *Ultramicroscopy*, 110(7), 852–861, 2010. doi:10.1016/j.ultramic.2010.03.005.

[113] R. Tromp, J. Hannon, W. Wan, A. Berghaus and O. Schaff. "A new aberration-corrected, energy-filtered LEEM/PEEM instrument II. Operation and results". *Ultramicroscopy*, 127, 25–39, 2013. doi:10.1016/j.ultramic.2012.07.016.

[114] A. Locatelli, L. Aballe, T. O. Mentes, M. Kiskinova and E. Bauer. "Photoemission electron microscopy with chemical sensitivity: SPELEEM methods and applications". *Surface and Interface Analysis*, 38(12-13), 1554–1557, 2006. doi:10.1002/sia.2424.

[115] T. Schmidt, A. Sala, H. Marchetto, E. Umbach and H.-J. Freund. "First experimental proof for aberration correction in XPEEM: Resolution, transmission enhancement, and limitation by space charge effects". *Ultramicroscopy*, 126, 23–32, 2013. doi:10.1016/j.ultramic.2012.11.004.

[116] S. Schramm, A. Pang, M. Altman and R. Tromp. "A Contrast Transfer Function approach for image calculations in standard and aberration-corrected LEEM and PEEM". *Ultramicroscopy*, 115, 88–108, 2012. doi:10.1016/j.ultramic.2011.11.005.

[117] Elmitec GmbH. "`https://elmitec.de/`". Web, accessed 26-Oct-2018.

[118] A. Zakharov, A.Mikkelsen and J. Andersen. "Recent advances in imaging of properties and growth of low dimensional structures for photonics and electronics by XPEEM". *Journal of Electron Spectroscopy and Related Phenomena*, 185(10), 417–428, 2012. doi:10.1016/j.elspec.2012.03.002.

[119] R. Belkhou, S. Stanescu, S. Swaraj, A. Besson, M. Ledoux, M. Hajlaoui and D. Dalle. "HERMES: a soft X-ray beamline dedicated to X-ray microscopy". *Journal of Synchrotron Radiation*, 22(4), 968–979, 2015. doi:10.1107/s1600577515007778.

[120] S. Swaraj, R. Belkhou, S. Stanescu, M. Rioult, A. Besson and A. P. Hitchcock. "Performance of the HERMES beamline at the carbon K-edge". *Journal of Physics: Conference Series*, 849, 012046, 2017. doi:10.1088/1742-6596/849/1/012046.

[121] O. H. Griffith and W. Engel. "Historical perspective and current trends in emission microscopy, mirror electron microscopy and low-energy electron microscopy". *Ultramicroscopy*, 36(1-3), 1–28, 1991. doi:10.1016/0304-3991(91)90135-s.

[122] W. Świech, B. Rausenberger, W. Engel, A. Bradshaw and E. Zeitler. "Insitu studies of heterogeneous reactions using mirror electron microscopy". *Surface Science*, 294(3), 297–307, 1993. doi:10.1016/0039-6028(93)90116-2.

[123] S. Nepijko and N. Sedov. "Aspects of Mirror Electron Microscopy". In "Advances in Imaging and Electron Physics", pages 273–323. Elsevier, 1997. doi:10.1016/s1076-5670(08)70125-3.

[124] G. F. Rempfer and O. H. Griffith. "Emission microscopy and related techniques: Resolution in photoelectron microscopy, low energy electron microscopy and mirror electron microscopy". *Ultramicroscopy*, 47, 35–54, 1992. doi:10.1016/0304-3991(92)90184-L.

[125] S. M. Kennedy, D. E. Jesson and D. M. Paganin. "Laplacian and caustic imaging theories of MEM work-function contrast". *IBM Journal of Research and Development*, 55(4), 3:1–3:8, 2011. doi:10.1147/jrd.2011.2143310.

[126] C. Schneider. *Soft X-ray photoelectron emission-microscopy (X-PEEM).* Springer Netherlands, 2006. doi:10.1007/1-4020-3337-0_8.

[127] J. Stohr and S. Anders. "X-ray spectro-microscopy of complex materials and surfaces". *IBM Journal of Research and Development*, 44(4), 535–551, 2000. doi:10.1147/rd.444.0535.

[128] N. Rougemaille and A. K. Schmid. "Magnetic imaging with spin-polarized low-energy electron microscopy". *The European Physical Journal Applied Physics*, 50(2), 20101, 2010. doi:10.1051/epjap/2010048.

[129] D. C. Grinter, S. D. Senanayake and J. I. Flege. "In situ growth, structure, and real-time chemical reactivity of well-defined CeO x -Ru(0001) model surfaces". *Applied Catalysis B: Environmental*, 197, 286–298, 2016. doi:10.1016/j.apcatb.2016.02.043.

[130] G. Odahara, S. Otani, C. Oshima, M. Suzuki, T. Yasue and T. Koshikawa. "In-situ observation of graphene growth on Ni(111)". *Surface Science*, 605(11-12), 1095–1098, 2011. doi:10.1016/j.susc.2011.03.011.

[131] J. Feng and A. Scholl. *Photoemission Electron Microscopy (PEEM)*. New York: Springer, 2007. doi:10.1007/978-0-387-49762-4_9.

[132] A. Locatelli, T. O. Menteş, M. Á. Niño and E. Bauer. "Image blur and energy broadening effects in XPEEM". *Ultramicroscopy*, 111(8), 1447–1454, 2011. doi:10.1016/j.ultramic.2010.12.020.

[133] E. Bauer. "A brief history of PEEM". *Journal of Electron Spectroscopy and Related Phenomena*, 185(10), 314–322, 2012. doi:10.1016/j.elspec.2012.08.001.

[134] E. B. A Locatelli. "Recent advances in chemical and magnetic imaging of surfaces and interfaces by XPEEM". *Journal of Physics: Condensed Matter*, 20(9), 093002, 2008. doi:10.1088/0953-8984/20/9/093002.

[135] J. Liu. *High-Resolution Scanning Electron Microscopy*, pages 325–359. Springer US, Boston, MA, 2005. ISBN 978-1-4020-8006-7. doi:10.1007/1-4020-8006-9_11.

[136] J. I. Goldstein, D. E. Newbury, J. R. Michael, N. W. Ritchie, J. H. J. Scott and D. C. Joy. *Scanning Electron Microscopy and X-Ray Microanalysis*. Springer New York, 2018. doi:10.1007/978-1-4939-6676-9.

[137] E. Bettini, U. Kivisäkk, C. Leygraf and J. Pan. "Study of corrosion behavior of a 22% Cr duplex stainless steel: Influence of nano-sized chromium nitrides and exposure temperature". *Electrochimica Acta*, 113, 280–289, 2013. doi:10.1016/j.electacta.2013.09.056.

[138] C. Örnek and D. Engelberg. "SKPFM measured Volta potential correlated with strain localisation in microstructure to understand corrosion susceptibility of cold-rolled grade 2205 duplex stainless steel". *Corrosion Science*, 99, 164–171, 2015. doi:10.1016/j.corsci.2015.06.035.

[139] S. Takeda and H. Yoshida. "Atomic-resolution environmental TEM for quantitativein-situmicroscopy in materials science". *Microscopy*, 62(1), 193–203, 2013. doi:10.1093/jmicro/dfs096.

[140] C. Paulsen, R. Broks, M. Karlsen, J. Hjelen and I. Westermann. "Microstructure Evolution in Super Duplex Stainless Steels Containing σ-Phase Investigated at Low-Temperature Using In Situ SEM/EBSD Tensile Testing". *Metals*, 8(7), 478, 2018. doi:10.3390/met8070478.

[141] F. Zhang, J. Evertsson, F. Bertram, L. Rullik, F. Carlà, M. Långberg, E. Lundgren and J. Pan. "Integration of electrochemical and synchrotron-based X-ray techniques for in-situ investigation of aluminum anodization". *Electrochimica Acta*, 241, 299–308, 2017. doi:10.1016/j.electacta.2017.04.154.

[142] J. Elmer, T. Palmer and E. Specht. "In situ observations of sigma phase dissolution in 2205 duplex stainless steel using synchrotron X-ray diffraction". *Materials Science and Engineering: A*, 459(1-2), 151–155, 2007. doi:10.1016/j.msea.2007.01.071.

[143] C. Örnek, M. Långberg, J. Evertsson, G. Harlow, W. Linpé, L. Rullik, F. Carlà, R. Felici, E. Bettini, U. Kivisäkk, E. Lundgren and J. Pan. "In-situ synchrotron GIXRD study of passive film evolution on duplex stainless steel in corrosive environment". *Corrosion Science*, 141, 18–21, 2018. doi:10.1016/j.corsci.2018.06.040.

[144] D. E. Starr, Z. Liu, M. Hävecker, A. Knop-Gericke and H. Bluhm. "Investigation of solid/vapor interfaces using ambient pressure X-ray photoelectron spectroscopy". *Chemical Society Reviews*, 42(13), 5833, 2013. doi:10.1039/c3cs60057b.

[145] L. Trotochaud, A. R. Head, O. Karslıoğlu, L. Kyhl and H. Bluhm. "Ambient pressure photoelectron spectroscopy: Practical considerations and experimental frontiers". *Journal of Physics: Condensed Matter*, 29(5), 053002, 2016. doi:10.1088/1361-648x/29/5/053002.

[146] D. E. Starr, M. Favaro, F. F. Abdi, H. Bluhm, E. J. Crumlin and R. van de Krol. "Combined soft and hard X-ray ambient pressure photoelectron spectroscopy studies of semiconductor/electrolyte interfaces". *Journal of Electron Spectroscopy and Related Phenomena*, 221, 106–115, 2017. doi:10.1016/j.elspec.2017.05.003.

[147] A. Kolmakov, L. Gregoratti, M. Kiskinova and S. Günther. "Recent Approaches for Bridging the Pressure Gap in Photoelectron Microspectroscopy". *Topics in Catalysis*, 59(5-7), 448–468, 2016. doi:10.1007/s11244-015-0519-1.

[148] M. F. Lichterman, S. Hu, M. H. Richter, E. J. Crumlin, S. Axnanda, M. Favaro, W. Drisdell, Z. Hussain, T. Mayer, B. S. Brunschwig, N. S. Lewis, Z. Liu and H.-J. Lewerenz. "Direct observation of the energetics at a semiconductor/liquid junction by operando X-ray photoelectron spectroscopy". *Energy & Environmental Science*, 8(8), 2409–2416, 2015. doi:10.1039/c5ee01014d.

[149] A. Baraldi, G. Comelli, S. Lizzit, D. Cocco, G. Paolucci and R. Rosei. "Temperature programmed X-ray photoelectron spectroscopy: a new technique for the study of surface kinetics". *Surface Science*, 367(3), L67–L72, 1996. doi:10.1016/s0039-6028(96)01126-0.

[150] H. Li, C. Rameshan, A. V. Bukhtiyarov, I. P. Prosvirin, V. I. Bukhtiyarov and G. Rupprechter. "CO2 activation on ultrathin ZrO2 film by H2O co-adsorption: In situ NAP-XPS and IRAS studies". *Surface Science*, 679, 139–146, 2019. doi:10.1016/j.susc.2018.08.028.

[151] J. I. Flege and P. Sutter. "In situstructural imaging of CO oxidation catalysis on oxidized Rh(111)". *Physical Review B*, 78(15), 2008. doi:10.1103/physrevb.78.153402.

[152] H. Guo, E. Strelcov, A. Yulaev, J. Wang, N. Appathurai, S. Urquhart, J. Vinson, S. Sahu, M. Zwolak and A. Kolmakov. "Enabling Photoemission Electron Microscopy in Liquids via Graphene-Capped Microchannel Arrays". *Nano Letters*, 17(2), 1034–1041, 2017. doi:10.1021/acs.nanolett.6b04460.

[153] A. Schmid, W. Świech, C. Rastomjee, B. Rausenberger, W. Engel, E. Zeitler and A. Bradshaw. "The chemistry of reaction-diffusion fronts investigated by microscopic LEED I–V fingerprinting". *Surface Science*, 331-333, 225–230, 1995. doi:10.1016/0039-6028(95)00128-x.

[154] K. L. Man, Z. Q. Qiu and M. S. Altman. "Kinetic Limitations in Electronic Growth of Ag Films on Fe(100)". *Physical Review Letters*, 93(23), 2004. doi:10.1103/physrevlett.93.236104.

Summa cum lauge? Don't laugengebäck in anger!

Printed by Media-Tryck, Lund 2018 NORDIC SWAN ECOLABEL 3041 0903

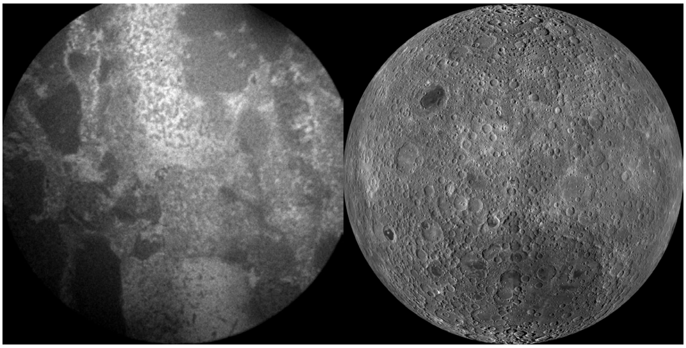

Figure X: Comparison between a PEEM image of a steel sample and an orthographic projection of the far side of the moon.

LUND
UNIVERSITY

Faculty of Science
Department of Physics
Division of Synchrotron Radiation Research

ISBN 978-91-7753-900-1 (print)
ISBN: 978-91-7753-901-8 (pdf)